
Neural Representations of Visual Motion Processing in the Human
Brain Using Laminar Imaging at 9.4 Tesla

Dissertation

zur Erlangung des Grades eines
Doktors der Naturwissenschaften

der Mathematisch-Naturwissenschaftlichen Fakultät
und
der Medizinischen Fakultät
der Eberhard-Karls-Universität Tübingen

vorgelegt

von

Fatemeh Molaei Vaneghi

aus Tehran, Iran

Juli - 2019

Tag der mündlichen Prüfung: 25-07-2019

Dekan der Math.-Nat. Fakultät: Prof. Dr. W. Rosenstiel

Dekan der Medizinischen Fakultät: Prof. Dr. I. B. Autenrieth

1. Berichterstatter: Prof. Dr. / PD Dr. / Dr. Andreas Bartels

2. Berichterstatter: Prof. Dr. / PD Dr. / Dr. Uwe Ilg

Prüfungskommission:

Prof. Dr. / PD Dr. / Dr. Andreas Bartels

Prof. Dr. / PD Dr. / Dr. Klaus Scheffler

Prof. Dr. / PD Dr. / Dr. Uwe Ilg

Prof. Dr. / PD Dr. / Dr. Marc Himmelbach

Erklärung / Declaration:

Ich erkläre, dass ich die zur Promotion eingereichte Arbeit mit dem Titel:

"Neural Representations of Visual Motion Processing in the Human Brain Using Laminar Imaging at 9.4 Tesla" selbständig verfasst, nur die angegebenen Quellen und Hilfsmittel benutzt und wörtlich oder inhaltlich übernommene Stellen als solche gekennzeichnet habe. Ich versichere an Eides statt, dass diese Angaben wahr sind und dass ich nichts verschwiegen habe. Mir ist bekannt, dass die falsche Abgabe einer Versicherung an Eides statt mit Freiheitsstrafe bis zu drei Jahren oder mit Geldstrafe bestraft wird.

I hereby declare that I have produced the work entitled "Neural Representations of Visual Motion Processing in the Human Brain Using Laminar Imaging at 9.4 Tesla", submitted for the award of a doctorate, on my own (without external help), have used only the sources and aids indicated and have marked passages included from other works, whether verbatim or in content, as such. I swear upon oath that these statements are true and that I have not concealed anything. I am aware that making a false declaration under oath is punishable by a term of imprisonment of up to three years or by a fine.

Tübingen, den 25072019

Datum / Date

.....

Unterschrift /Signature

To Farzaneh and Maysam

List of Abbreviations

AFI: Actual Flip Angle Imaging
ACS: Auto Calibration Signal
ALITS: Ascending Limb of the Inferior Temporal Sulcus
BOLD: Blood Oxygen Level Dependent
bSSFP: balanced Steady-State Free-Precession
CS: Calcarine Sulcus
CBV: Cerebral Blood Volume
CBF: Cerebral Blood Flow
CSF: Cerebral Spinal Fluid
B1+: Radio-Frequency (RF) Transmit Field
B1-: Radio-Frequency (RF) Receive Field
dHB: Deoxygenated Hemoglobin
EPI: Echo-Planar Imaging
FH: Food-Head
FLEET: Fast-Low Angle Excitation Echo-Planar Technique
fMRI: Functional Magnetic Resonance Imaging
FOV: Field-of-View
fCNR: Functional Contrast-to-Noise Ratio
GM: Gray Matter
GRE: Gradient Echo
3D-GRASE: inner-volume 3D Gradient-and-Spin-Echo
GRAPPA: Generalized Autocalibrating Partial Parallel Acquisition
ITS: Inferior Temporal Sulcus
IREPI: Inversion Recovery EPI
LO: Lateral Occipital Sulcus
B0: Local Magnetic Field
MPRAGE: Magnetization Prepared Rapid Gradient Echo
ODC: Ocular Dominance Column
POS: Parietal-Occipital Sulcus
PA: Posterior-Anterior
PED: Phase Encoding Direction
pMST: putative Medial Superior Temporal Cortex
PSF: Point Spread Function Correction
rBBR: Recursive Boundary Based Registration
ROI: Region of Interest
TE: echo Train
TOS: Transverse Occipital Sulcus
TR: Repetition Time
tSNR: Temporal Signal to Noise Ratio
UHF: Ultra High Field Imaging
IPS: Inferior Posterior Sulcus
WM: White Matter

Contents

List of Abbreviations.....	5
Abstract	8
CHAPTER 1. Introduction.....	10
1.1. Neural Basis of Real-World Motion Processing	10
1.2. Laminar Imaging at UHF	12
1.3. Feedforward and Feedback Signals	15
1.4. Sensory Integration	16
1.5. Scope and Main Goals	17
CHAPTER 2. Acquisition and Analysis Strategies for Conducting Laminar fMRI Studies at UHF	19
2.1. Introduction	19
2.1.1. Ultra-High Field Imaging	19
2.1.2. Development of Functional Sequences for UHF Imaging	21
2.1.3. Laminar fMRI	23
2.2. Methods	24
2.2.1. Subjects	24
2.2.2. Visual Stimulation	24
2.2.3. Anatomical Imaging	25
2.2.4. Functional Imaging	26
2.2.5. Depth-Dependent Analysis	27
2.3. Results	30
2.3.1. Anatomical Imaging	30
2.3.2. Functional Imaging	31
2.3.3. Sequence Comparison at 9.4T	33
2.3.4. Depth-Dependent Analysis of fMRI Data	34
2.4. Discussion.....	36
2.4.1. Sequence Development for Laminar Imaging	36
2.4.2. Depth-Dependent and Laminar fMRI	39
2.5. Conclusion.....	41
CHAPTER 3: Laminar Responses to Visual Motion and Pursuit Integration in Human Areas V3A and V6 Measured Using 9.4T fMRI	43
3.1. Introduction	43
3.2. Methods	45
3.2.1. Participants	45
3.2.2. Visual Stimulation and Experimental Design	45
3.2.3. Procedure	46
3.2.4. Fixation Task	46
3.2.5. Data Acquisition and Image Reconstruction	46
3.2.6. Preprocessing and Statistical Analysis of Functional Volumes	47
3.2.7. Definition of Regions of Interest.....	48
3.2.8. Depth Dependent Analysis	49
3.2.9. Statistical Analysis	51
3.3. Results.....	51
3.3.1. Laminar Responses to Retinal and Objective Motion in V3a and V6	52
3.3.2. Laminar Response in V3A and V6 after Removal of the Mean Signal and the Linear Trend	54
3.4. Discussion.....	55

CHAPTER 4. Real World Motion Processing in MT, pMST, and V1. A Laminar fMRI Study at 9.4T	61
4.1. Introduction	61
4.2. Methods	62
4.2.1. Participants	63
4.2.2. Visual Stimulation and Experimental Design	63
4.2.3. Procedure	64
4.2.4. Fixation Task	64
4.2.5. Data Acquisition and Image Reconstruction	65
4.2.6. Pre-processing and Statistical Analysis of Functional Volumes	65
4.2.7. Definition of Region of Interest (ROI)	66
4.2.8. Depth-Dependent Analysis	67
4.2.9. Correlation Analysis	67
4.3. Results	68
4.3.1. Depth-dependent Response to Retinal, Objective, and Pursuit Motion	69
4.3.2. Correlation	71
4.4. Discussion.....	73
References.....	78
Statement of Contributions	92
Acknowledgements	93

Abstract

During natural behavior, much of the motion signal falling into our eyes is due to our own movements. Therefore, in order to correctly perceive motion in our environment, it is important to parse visual motion signals into those caused by self-motion such as eye- or head-movements and those caused by external motion. Neural mechanisms underlying this task, which are also required to allow for a stable perception of the world during pursuit eye movements, are not fully understood. Both, perceptual stability as well as perception of real-world (i.e. objective) motion are the product of integration between motion signals on the retina and efference copies of eye movements.

The central aim of this thesis is to examine whether different levels of cortical depth or distinct columnar structures of visual motion regions are differentially involved in disentangling signals related to self-motion, objective, or object motion. Based on previous studies reporting segregated populations of voxels in high level visual areas such as V3A, V6, and MST responding predominantly to either retinal or extra- retinal ('real') motion, we speculated such voxels to reside within laminar or columnar functional units. We used ultra-high field (9.4T) fMRI along with an experimental paradigm that independently manipulated retinal and extra-retinal motion signals (smooth pursuit) while controlling for effects of eye-movements, to investigate whether processing of real world motion in human V5/MT, putative MST (pMST), and V1 is associated to differential laminar signal intensities. We also examined motion integration across cortical depths in human motion areas V3A and V6 that have strong objective motion responses. We found a unique, condition specific laminar profile in human area V6, showing reduced mid-layer responses for retinal motion only, suggestive of an inhibitory retinal contribution to motion integration in mid layers or alternatively an excitatory contribution in deep and superficial layers. We also found evidence indicating that in V5/MT and pMST, processing related to retinal, objective, and pursuit motion are either integrated or colocalized at the scale of our resolution. In contrast, in V1, independent functional processes seem to be driving the response to retinal and objective motion on the one hand, and to pursuit signals on the other. The lack of differential signals across depth in these regions suggests either that a columnar rather than laminar segregation governs these functions in these areas, or that the methods used were unable to detect differential neural laminar processing.

Furthermore, the thesis provides a thorough analysis of the relevant technical modalities used for data acquisition and data analysis at ultra-high field in the context of laminar fMRI. Relying on our technical implementations we were able to conduct two high-resolution fMRI experiments that helped us to further investigate the laminar organization of self-induced and externally induced motion cues in human high-level visual areas and to form speculations about the site and the mechanisms of their integration.

Keywords: efference copy, eye movements, ultra-high Field MRI, Visual Motion, multimodal integration

CHAPTER 1. Introduction

1.1. Neural Basis of Real-World Motion Processing

A number of neuronal functions are involved in visual motion processing, many of such functions, however, can be performed only by visual processing. A stable perception of the world through differentiation between self-induced and externally-induced motion calls for a multi-modal integration of visual motion signals with non-visual cues such as efference copies of the eye movement von Holst and Mittelstaedt (1950b); (Gibson 1954; Royden, Banks, and Crowell 1992; Ilg and Churan 2004). The absence of such sensory integration, where eye- or head-movements are interpreted as external motion can lead to severe impairing consequences (Haarmeier et al. 1997). To differentiate between retinal and extra-retinal signals (such as efference copies of the eye movement) and to disentangle the source of motion, visual system takes into account the movement of the eyes besides that of retinal images (Galletti and Fattori 2003). High-level visual motion processing including integration between visual and non-visual cues have been the focus of many recent human fMRI studies. Such studies paved the way for shedding light on previously poorly understood human cortical regions such as V3A, V6, and Cingulate sulcus visual area (CSv) (Wall et al. 2008; Pitzalis et al. 2010; Arnoldussen, Goossens, and van den Berg 2011; Fischer et al. 2012b). The existence of an internal efferent signal of eye- or head-movement and the integration of this signal with that of retinal motion, which allows for 'real' world motion perception was first suggested by Helmholtz and by Holst and Mittelstaedt. It has been shown that frontal eye fields (FEFs) are among the key cortical regions involved in pursuit execution as well as saccades. FEFs in primates are not only involved in driving pursuit and encoding its trajectories i.e. processing visual motion cues but also in processing extra-retinal cues related to ongoing eye-movements (Fukushima et al. 2002; Ilg and Thier 2008; Schoppik, Nagel, and Lisberger 2008). Varying fractions of 'real motion' neurons, i.e. neurons that are responsive to the motion of edges in the environment (even if it is cancelled on the retina by visual pursuit), rather than retinal motion (either self-induced or due to external motion) have been revealed in several cortical regions in monkeys (Galletti, Battaglini, and Fattori 1990; Erickson and Thier 1991; Ilg and Churan 2004; Zhang, Heuer, and Britten 2004; Dicke, Chakraborty, and Thier 2008). These areas, which are thought to receive efferent copies from eye-movements and to mediate perceptual stability include ventral intraparietal area (VIP), visual posterior sylvian area (VPS) V3A, V6, and MST. Populations of 'real motion' cells that are

responsive to pursuit in the absence of visual stimulation have been reported in MST (Erickson and Thier 1991). In addition to smooth pursuit processing, MST (or better MSTd) is also implied in processing self-motion cues. Contrary to V5/MT, MST and VIP are involved in integrating visual and vestibular self-motion signals and, therefore, have been labeled multisensory in the context of processing ego-motion (Chowdhury et al. 2009; Bremmer et al. 2001). A recent study reported a unique property of *human* V3A among other visual areas in the human brain, in that V3A had highly pronounced responses to planar objective ('real') motion while it lacked any response to planar retinal motion (Fischer et al. 2012a). The same study reported a similar behavior in V6; strong responsiveness to objective 'real' motion while being suppressed by planar retinal motion. Previous studies investigating the response to objective 'real' motion and to retinal motion in other visual motion processing areas have shown that MST responds to both retinal and objective (head-centered) motion components, whereas V5/MT is more responsive to retinal than to head-centered motion (Fischer et al. 2012b). Neurophysiological studies in monkeys have reported MST response to be correlated with target motion on the screen independent of pursuit and relative to the head, whereas neurons in V5/MT were mostly correlated with target motion on the retina (Chukoskie and Movshon 2009; Gegenfurtner et al. 2003; Inaba et al. 2007). The integration between visual motion cues and pursuit eye movements in humans has been investigated in only a few studies. A group of functionally segregated voxels that respond predominantly to either external ('real') motion or to retinal motion have been reported in human V3A, V6, and MST (Arnoldussen, Goossens, and van den Berg 2011). Signs of integration between retinal flow and eye-position have also been reported in human MST (Goossens et al. 2006). Functional characteristics of Cingulate sulcus visual area (CSv) has also shown to be relevant in the context of processing self-motion cues. Fischer and colleagues found that CSv was peculiar in several aspects: in contrast to V5/MT and MST, CSv was preferentially more responsive to planar motion compared to forward flow, it lacked any response to random motion, and it appeared to have very large receptive fields spanning both hemifields. Compared to V3A and V6, CSv integrated retinal motion with eye-movements to a lesser degree, but more than MST (Fischer et al. 2012b). Therefore, CSv is another candidate region processing large-field homogeneous flow induced by self-motion. A human homologue of macaque VIP has also been reported to be a candidate region for distinguishing between purely visual signals related to self-motion and to object-motion based on its functional response and its

connectivity with MST (Bartels, Zeki, and Logothetis 2008). These results confirm V3A to stand out among motion responsive areas in humans based on its strong responsiveness to objective 'real' motion and its lack of response to retinal motion cues (Fischer et al. 2012a). Direct comparisons of fMRI responses between human and macaque regions have additionally demonstrated that V3A is much more responsive to motion compared to its macaque counterpart (Orban et al. 2003).

Processing of retinal motion happens at the very first stages of visual motion processing. Only stages of motion processing, in which integration of extra-retinal signals such as vestibular cues or efference copies of the eye movements happens allow for inferring the source of motion. Nevertheless, aside from our knowledge on extensive studies on motion processing areas such as V5/MT and MST, little is known on how and where in the human brain retinal and extra-retinal motion cues such as pursuit eye movement are integrated in order to perceive the motion in the real world.

1.2. Laminar Imaging at UHF

The ability to acquire high-resolution data at a sub-millimeter scale afforded by significant increases in sensitivity and specificity at ultra-high field (UHF) magnetic fields (≥ 7 T) has made fMRI a key application of ultra-high field MRI systems. The techniques offered by ultra-high field MRI to enhance T2*-contrast imaging such as blood oxygenation level dependent (BOLD) contrast, and to increase signal-to-noise ratio (SNR) (Edelstein et al. 1986) led to a substantial increase in functional contrast-to-noise ratio (fCNR), which opens new doors into exploring the functional organization of human cortex at the level of cortical layers and columns. Through enhancement of fCNR at UHF fine functional structures can be captured in a reduced number of measurement runs or with less averaging. This allows for more time-efficient measurements, which is crucial in clinical settings, or single-subject studies, or even patient-specific diagnosis (Arbabshirani et al. 2017).

The main objective of increased sensitivity provided by UHF has, however, been the increase in spatiotemporal resolution of the acquisition. Faster sampling rate allows for more accurate sampling of the rapid hemodynamic response to transient neuronal activity (Smith and Sommer 2013), whereas finer spatial sampling helps to resolve small cortical and subcortical structures such as cortical layers and columns (Newton et al. 2012; De Martino et al. 2013; Satpute et al. 2013; Faull et al. 2015). Prevention of physiological noise sources and enabling

strategies for adequate sampling are amongst other benefits of high spatiotemporal resolution (Polimeni et al. 2018).

Reduction in voxel volume reduces random noise cancellation within the voxels, and therefore, leads to lower SNR. Similarly, higher temporal resolution reduces signal recovery via longitudinal relaxation, and therefore, leads to lower SNR. Thus, higher spatiotemporal resolution can result in lower SNR. Nevertheless, UHF-fMRI provides the additional SNR required for compensating the reduced SNR caused by high spatiotemporal resolution and still being able to obtain high resolution imaging.

At higher fields T2 relaxation time of brain tissue decreases more slowly compared to blood, this results in the origin of the BOLD fMRI to shift from intravascular signal to predominantly extravascular signal (Ugurbil et al. 2000). Thus, potential enhancement in signal specificity is another advantage of imaging at UHF. The availability of acquisition techniques such as balanced steady-state free-precession (bSSFP) (Scheffler et al. 2001; Miller et al. 2003) or Hahn spin echo with more sensitivity to extravascular signal changes around small venules and capillaries offers the possibility to restrict BOLD sensitivity only to the smallest vessels in parenchyma, which are thought to be more specific to neural activation. Therefore, such acquisitions allow for avoiding the impact of large draining vessels in corrupting and shifting spatial organization of functional activity (Polimeni et al. 2010a; Olman, Inati, and Heeger 2007).

Despite many advantages that UHF offers, there are still challenges that need to be addressed to be able to benefit from full potential of functional imaging at UHF. Field inhomogeneities in the local magnetic field (B_0) due to increased magnetic susceptibility effects as well as in radio-frequency (RF) transmit (B_1^+) and receive (B_1^-) fields caused by dielectric effects, increase at higher field strength. Such spatial inhomogeneities can lead to geometric distortions and intensity biases, which also scale with field strength and can potentially diminish the benefits offered by imaging at UHF. The enhanced impact of these artifacts at UHF becomes even more magnified in studies requiring high spatial accuracy at the level of cortical layers and columns.

Furthermore, reconstructing an accurate surface model from high resolution anatomical data acquired at UHF, which is a crucial step in any laminar fMRI study can be heavily affected by such artifacts. Due to having high tissue contrast and the ability to provide images with high spatial resolution in reasonable measuring time, magnetization-prepared T1-weighted pulse

sequences such as those derived from MPRAGE (Marques et al. 2010; van der Kouwe et al. 2008) have been commonly used for structural imaging. The quality of these anatomical sequences is heavily dependent upon a uniform RF transmit field during magnetization preparation. This assumption, however, is often violated at UHF, which results in tissue contrast being severely degraded especially in areas around the inferior temporal lobe that are affected by both B_0 and B_1+ inhomogeneities (Collins et al. 2005) as well as in orbitofrontal cortex and temporal poles, where gray matter and white matter can even appear isointense. This is a major issue when it comes to accurate reconstruction of cortical surfaces, which must be addressed at the time of acquisition. Excitation pulses can also be affected by nonuniformities in RF transmit field, which in case of MPRAGE can cause spatially varying intensity biases. Preprocessing steps prior to anatomical segmentation and surface reconstruction can be used to remedy the effect of such biases. Additionally, acquisition techniques based on acquiring a second, proton-density volume matched to the anatomical image e.g. MPRAGE can be applied to circumvent the impact of these vascular artifacts as well as intensity biases (Van de Moortele et al. 2009).

Exploring functional organizations within the six cellular layers of the cortex with 3mm thickness (Brodmann 1909; Economo 1929) asks for high-resolution imaging at the scale of cortical layers and columns, which is not usually feasible at conventional field strength (3T and below). Another advantage of UHF imaging, which is crucial in the context of depth-dependent fMRI studies is the reduced partial voluming of grey matter (GM) voxels with white matter (WM) and cerebrospinal fluid (CSF) (Koopmans et al. 2011; Yacoub et al. 2003; Logothetis 2002; Ress et al. 2007; Polimeni et al. 2010a). High resolution imaging increases the proportion of voxels containing cortical gray matter, it also significantly reduces contaminations related to physiological noise (Triantafyllou et al. 2005). With smaller voxel size, contribution of large draining vessels to spatial bias of the BOLD signal is reduced (Polimeni et al. 2010a), whereas functional signals originating from smaller vessels and capillaries are sufficiently enhanced to become detectable (De Martino et al. 2013). Image distortions (Wald and Polimeni 2017) and signal dropouts (Merboldt, Finsterbusch, and Frahm 2000) associated with ultrahigh field have been reduced with recent developments in parallel imaging techniques (Keil and Wald 2013). Advancements of high field imaging along with studies that provide direct evidence of the sensitivity of fMRI to capture neuronal processes at the level of functional layers (Muckli et al. 2015; Kok et al. 2016) and columns

(Yacoub, Harel, and Ugurbil 2008b; Shmuel et al. 2010; Chaimow et al. 2011; Nasr, Polimeni, and Tootell 2016) greatly enhanced the feasibility of studying layer-specific neuronal responses in human brain. This leads to a paradigm shift in neuroscientific questions that can be addressed in human fMRI studies. Recent studies have been successful in probing fine functional organizations such as cortical layers and columns in the human cortex by employing high-resolution imaging at a sub-millimeter scale affordable at UHF (Kok et al. 2016; Muckli et al. 2015; Fracasso et al. 2018; Kemper et al. 2015; Olman et al. 2012; Zimmermann et al. 2011). Making inferences about neuronal activation across cortical depth based on laminar fMRI calls for an understanding of how neurovascular coupling i.e. relationship between neural activity and vascular changes measured with fMRI varies as a function of cortical depth. A steady increase towards the cortical surface has been observed in early laminar fMRI studies investigating visually driven BOLD response in human visual cortex (Ress et al. 2007). Nevertheless, this enhanced response towards the shallow depths of the cortex was likely driven by large vessels draining venous blood towards the cortical surface (Turner and Jones 2003). When corrected for the contribution of venous draining, visually driven BOLD response (Kok et al. 2016) revealed a peak in layer 4 of V1 (Koopmans, Barth, and Norris 2010) conforming to previously reported invasive recordings from animals (Hubel and Wiesel 1972). The change in neurovascular coupling across cortical depth have been previously examined using laminar fMRI measurements of changes in cerebral blood volume (CBV) and blood flow (CBF) as well as BOLD in stimulated and unstimulated areas of macaque V1 (Goense, Merkle, and Logothetis 2012). It was reported that neurovascular coupling varies across cortical depth, and that it also differs between stimulated and unstimulated areas of the cortex. This notion should therefore be taken into account when inferences are drawn from laminar fMRI about neuronal activation across cortical depth (Uludag and Blinder 2018).

1.3. Feedforward and Feedback Signals

Feedforward processing signals and transforms sensory inputs, whereas feedback processing constructs a narrative based on what the brain predicts about the environmental and sensory inputs (Clark 2013; Park and Friston 2013). Processing related to feedforward and feedback inputs has different effects on receptive fields of neuronal populations. It is also known that feedforward and feedback inputs originate and terminate in different cortical layers (Markov

and Kennedy 2013), their processes activate different layers of a cortical unit (Self et al. 2013). The same holds true for lateral or horizontal connections too. In case of V1 for instance, feedforward connections from geniculate nucleus of the thalamus primarily into V1 terminate in layer 4 (Hubel and Wiesel 1972). Horizontal connections between columns of V1, on the other hand, are present in all layers with predominant terminations in upper layer 4 and shallow layers (Rockland and Pandya 1979). Finally, feedback connections into V1 from higher visual areas avoid layer 4 and primarily terminate in layer 1 and 5 (Anderson and Martin 2009; Felleman and Van Essen 1991; Markov and Kennedy 2013; Rockland and Virga 1989). It is also known that feedforward and feedback signals are distinguished by distinct oscillatory rhythms (Bastos et al. 2015; van Kerkoerle et al. 2014) and act on different glutamate receptors (Self et al. 2012). Feedforward processing operate in gamma and theta range, whereas feedback signals are carried by the alpha or beta frequencies. This suggest that bottom-up feedforward and top-down feedback signals serve different roles in communication, and that such separation of messages into different frequency bands could be used as a strategy to keep message passing independent when needed. The sender and receiver can hypothetically tune into feedforward and feedback signals independently. A separation in spatial organization of feedforward and feedback activity modulations, which are believed to have distinct functional roles (Self et al. 2013) could, therefore, be achieved through this relatively distinct structure of feedforward and feedback connectivity.

1.4. Sensory Integration

Neural activity in a given cortical region depends on the integration of sensory inputs carried by feedforward connections with internal representations carried by feedback connections, such combination of bottom-up and top-down processes is crucial for healthy cognition and consciousness (Bastos et al. 2015; Heeger 2017; Muckli 2010; Roelfsema and de Lange 2016). A conscious percept of a non-existent sound or sight for instance could occur (Horga et al. 2014) if the (mis)match between the two is not determined. Observing fluctuations in cortical ongoing activity modulating perception has revealed that internal modeling of forthcoming sensory inputs is likely to precede their arrival to the cortex (Hesselmann, Kell, and Kleinschmidt 2008). Depending on the behavioral demands, it might be advantageous for the brain to assign more weight to internal models or to perceptual inputs. Feedforward filtering operations are thought, by influential neurocomputational models of cortical function, to complement feedback processes carrying a prediction (or a generative model) of expected

input (Heeger 2017; Lee and Mumford 2003). A recent study investigating laminar profile of V1 activation under conditions of expected but absent bottom-up input have found that decoding of the visual scene in areas of visual cortex that received no bottom-up input was carried out via feedback processes that terminated in the supragranular layers (Muckli et al. 2015). In another study probing laminar activation in V1, a positive response to an illusory shape was found only in deep layers of V1, whereas a physical stimulus activated all layers of V1 (Kok et al. 2016). They speculated the perception of illusory shape to be driven by a prediction formed in higher-level brain regions, which is then fed back to the infragranular layers of V1. The findings of both studies are consistent with the known functional neuroanatomy of feedback projections entering deep and superficial layers and avoiding layer 4 (Anderson and Martin 2009; Rockland and Virga 1989). It can, therefore, be concluded that analysis of incoming sensory data is facilitated by responses in lower-level sensory areas being modulated by higher level cognitive processes. The integration of top-down modulatory processes with bottom-up sensory inputs is a fast-growing and increasingly important area of research in cognitive neuroscience. Despite these studies, the neuronal mechanisms underlying the integration between feedforward and feedback signals and their role in cognition remains not fully conceptualized. A multi-scale, multi-species approach is needed to develop an understanding about functional characteristics of such processing and to find out how and where their integration happens. We will not be able to develop a full understanding of constructive cortical processes until we find the missing piece of how the brain's internal and external worlds integrate.

Disentangling feedforward and feedback processes in fMRI signals captured at conventional field strength (3T and below) is very challenging if not impossible due to low resolution imaging. Most research distinguishing between the two has been performed on nonhuman primates using so-called laminar electrodes (Self et al. 2013; van Kerkoerle et al. 2014). Nevertheless, with recent developments in high-resolution functional imaging provided by ultra-high field fMRI, capturing layer-specific functional activations in human cortex has become possible.

1.5. Scope and Main Goals

In the present thesis we propose to use 9.4 Tesla human fMRI in order to examine laminar signals at very high spatial resolution in human visual regions V3A, V6 and MST during

exposure to high-level motion cues and during integration with pursuit eye-movements. Using ultra-high field (9.4T) imaging techniques we aim at resolving the question: Can we measure differential laminar distributions of signals related to retinal motion, objective motion, and to smooth pursuit eye-movements in V3A, V6 and MST? If so, the results may provide important hints with regards to the sources of the different signals in each of these regions, as upper, middle and lower layers are known to be differentially involved in processing of feedback, bottom-up input, and output signaling, respectively. At the same time, these results may also provide indications concerning the hierarchical relationship between V3A, V6 and MST. A similar question could also be asked as whether neural signals related to retinal motion, objective motion, and efference copies from eye movements are processed in independent sub-divisions (e.g., columns) within motion responsive regions. The results of Arnoldussen et al. (2011) leave the origin of the observed voxel-biases for retinal or head-centered motion open. They could have resulted from differential vascular pooling (Shmuel et al. 2010) , from laminar, or from columnar functional segregation.

Achieving the above aims requires ultra-high-resolution fMRI as well as highly specialized data analysis techniques specifically tailored to processing data acquired at high field MRI, as well as tailored to segregating signal across cortical depth over the curved structure of cortex. Prior studies using 7Tesla human fMRI have shown that the required resolution can be achieved: ocular dominance and orientation columns (Yacoub, Harel, and Ugurbil 2008a) as well as different lamina can be resolved in visual cortex (Polimeni et al. 2010a; Koopmans et al. 2011), and differential laminar response profiles for distinct stimulus conditions have also been demonstrated (Trampel et al. 2012). With 9.4T and the development of localized, high-resolution fMRI techniques we aim to further explore and boost the spatial limit, and to gain unique functional insights into high-level motion processing regions in the human brain.

CHAPTER 2. Acquisition and Analysis Strategies for Conducting Laminar fMRI Studies at UHF

2.1. Introduction

2.1.1. Ultra-High Field Imaging

Advances in parallel imaging techniques (Griswold et al. 2002; Pruessmann et al. 1999; Poser and Setsompop 2018), optimizations of multi-modal MRI sequences (Huber et al. 2018; Ivanov et al. 2017), and MRI technologies such as RF-coil technology (Vaughan et al. 2001) in addition to more accessibility to ultra-high field (UHF) scanners have opened up opportunities to push the spatial and temporal boundaries of human fMRI. fMRI at UHF benefits from substantial gain in spatiotemporal resolution to more accurately localize the neural activation driving the hemodynamic signal in the cortex (Uğurbil et al. 2003a), it also benefits from enhanced contrast to noise (CNR) and signal to noise (SNR) ratio offered by UHF. Advances in UHF fMRI, therefore, play a significant role in paving the way to probe fine functional structures in the human brain such as cortical layers and columns, which was not possible before. Nevertheless, acquisition techniques and analysis strategies for processing such high-resolution data are still being developed and optimized.

Application of conventional analysis workflows for UHF fMRI can introduce unwanted spatial or temporal blurring of the fMRI data or may lead to systematic errors in interpreting which anatomical regions are responding to a stimulus or task, and in some cases may even have deleterious effects on high-resolution fMRI data. Therefore, standard methods including preprocessing steps must be revisited when working with high-resolution fMRI data. Adaptation of the standard pre-processing steps for fMRI analysis to the steps tailored to specific considerations required for UHF fMRI have been previously discussed in detail (Polimeni et al. 2018). In the following section, we mainly focus on distortions and distortion correction techniques for UHF imaging as methods for distortion correction have shown to be one of the most challenging steps in depth-dependent fMRI studies.

EPI distortions are pronounced at UHF compared to conventional field strengths due to increased field offsets caused by susceptibility gradients, especially at air-tissue interfaces. Despite acquisition strategies to partially resolve these geometric distortions (Setsompop, Feinberg, and Polimeni 2016), several millimeters of distortion is still commonplace. This

emphasizes the need for more accurate distortion correction methods for UHF-fMRI studies, where several millimeter of distortion is not acceptable. Post-hoc distortion correction techniques including those (1): based on measuring the impact of the distortion on the EPI data such as the point-spread-function (PSF) correction or PLACE techniques (Xiang and Ye 2007), those (2): that calculate the distortion directly from the EPI data such as the blip-up/blip-down methods (Andersson, Skare, and Ashburner 2003; Holland, Kuperman, and Dale 2010), and those (3): based on direct measurements of the B0 field offset (Chen and Wyrwicz 1999; Hutton et al. 2002) remove the calculated distortion from EPI data through unwarping. This unwarping involves resampling of the shifted image onto the undistorted voxel grid and therefore requires interpolation, resulting in spatial correlations and spatially periodic resolution loss in the data. The resolution loss is not only a function of unwarping but also of spacing of voxel grid i.e. a displacement of 5 mm may cause local resolution loss for a 2 mm voxel grid but not for a 1 mm voxel grid. In order to circumvent the resolution loss due to interpolation and image resampling during distortion correction, surface-based distortion correction techniques have been proposed (Polimeni et al. 2018). Since in such methods surface mesh is deformed instead of the image, i.e. vertices of the surface mesh are displaced by the distortion field, no data sampling is required, and therefore, the effects of interpolation are minimized resulting in improved geometric accuracy of the fMRI data. There are, however, several caveats to this surface-based distortion correction, which is related to (1): head motion within or between experimental session causing the anatomical data to not be in register with the functional data or to (2): distortions causing spatially varying voxel sizes.

Compared to EPI-fMRI, T1 weighted anatomical images have higher GM-WM contrast, which is the main reason to utilize them for cortical layer definitions. For this reason, most studies of depth-dependent BOLD fMRI have so far relied on the conventional acquisition approach, which uses a differently-distorted structural and functional images. Examples include MP-RAGE & EPI (Fracasso et al. 2018; Muckli et al. 2015; Nasr, Polimeni, and Tootell 2016), MP-RAGE & 3D-GRASE (De Martino, Moerel, Ugurbil, et al. 2015; Olman et al. 2012; Zimmermann et al. 2011), MP2-RAGE & EPI (Kok et al. 2016), or MEMPRAGE & EPI (Polimeni et al. 2010b). However, such differences in pulse sequence, encoding scheme and readout between anatomical and functional data can pose limitations on achieving accurate registration between the two, which is crucial in high-resolution depth-dependent fMRI

studies. Although geometric distortions are still the main reason for the mismatch between EPI image and high-resolution anatomical image, it has been suggested that EPI quality is sufficient to be used as an anatomical reference. Inversion recovery preparation EPI with similar readouts to functional data for instance has been suggested to be a suitable technique for fast T1 mapping (Clare and Jezzard 2001; Gowland and Mansfield 1993; Ordidge et al. 1990b; Stehling et al. 1990). Clear advantages of IREPI approach in the context of depth-dependent fMRI, where minimal pre-processing of the functional data and accurate registration between functional and anatomical data is of utmost importance include: (1): foregoing the need to distortion-correct the fMRI data, and, therefore reducing the amount of interpolation and potential blurring associated with distortion correction. This in return limits the reduction of cortical depth-specific information. (2): distortion match between functional and anatomical data, which enhances the registration accuracy between the two. This approach has recently been used in depth-dependent analysis of high-resolution fMRI (Huber et al. 2017; Kashyap et al. 2016; Van Der Zwaag et al. 2016) including studies conducted at 9.4T (Ivanov et al. 2015). Despite evident benefits of IREPI approach, its performance in the context of depth-dependent fMRI has not yet been quantitatively evaluated against other acquisition strategies.

To avoid multiple interpolations and resampling steps conventionally carried out during pre-processing of fMRI data and to consequently reduce resolution loss, which is crucial in the context of laminar fMRI, it has been suggested to concatenate or mathematically compose all transformations required for preprocessing and to apply one transformation to the data and thus interpolate once. Several methods to perform multiple preprocessing steps simultaneously such as joint correction of slice-timing differences and head motion (Roche 2011) or simultaneous correction of geometric distortion and head motion (Andersson and Sotiropoulos 2016; Ernst et al. 1999) have been proposed recently.

2.1.2. Development of Functional Sequences for UHF Imaging

Zoomed-PSF

Distortions and signal dropouts, especially in areas with strong susceptibility differences like tissue and air interface, are amongst the most prominent artifacts in EPI imaging. The higher the strength of the MR field, the stronger these artifacts become. The same is with readout duration i.e. longer readout times result in higher artifacts. Pixel shift correction in image

space using a point spread function (PSF) map (In and Speck 2012). On the other hand, a reduction in echo train is often required at high field to obtain an optimal BOLD contrast. Combination of partial Fourier sampling with large parallel imaging factors is the most common approach for Cartesian trajectories. Another method to reduce the time to k-space center is zoomed imaging (Pfeuffer et al. 2002; Heidemann et al. 2012), in which reduction of the field of view (FOV) in phase encoding direction (PED) is combined with suppression of signals from outside of the volume of interest. To reduce the degree of distortions in functional images and to be able to obtain high resolution data with high SNR from scanning areas with limited field of view, we used a combination of zoomed and PSF correction.

bSSFP

Balanced steady-state free-precession (bSSFP) as a BOLD-sensitive acquisition was first proposed in stopband by Scheffler and Miller (Scheffler et al. 2001; Miller et al. 2003), later in 2005, a more robust version in passband was introduced (Bowen, S Menon, and Gati 2005; Bowen et al. 2006; Miller et al. 2007). Higher sensitivity of passband bSSFP to oxygenation changes in small vessels, similar to spin-echo (SE) sequences, and less sensitivity to large vessels have been demonstrated in previous studies (Scheffler and Hennig 2003; Bieri and Scheffler 2007; Miller et al. 2007; Miller and Jezzard 2008). Therefore, compared to gradient-echo (GE) sequences, bSSFP is capable of measuring the BOLD signal closer to the source of neuronal activation (Norris 2012). Furthermore, since bSSFP is in principle a distortion-free acquisition, it makes registration to structural images trivial. Nevertheless, reduced acquisition speed as well as reduced sensitivity to BOLD are currently the major drawbacks of bSSFP compared to GE-EPI.

FLEET

The fast-low angle excitation echo-planar technique (FLEET) is a hybrid of FLASH and segmented-EPI (Chapman et al. 1987; Polimeni et al. 2016). Compared to segmented EPI, the order of slice and segment loops is reversed in FLEET, such that all segments for a given slice are fully acquired before moving to the next slice. This order of acquisition reduces the effect of respiration and motion by minimizing the temporal separation between segments of a single slice. In other words, FLEET type segmented acquisition removes SNR discontinuity across slices caused by respiration, and therefore, provides motion robustness. It also

increases tSNR relative to EPI auto calibration signal (EPI-ACS) and reduces ghosting in presence of B0 inhomogeneity because FLEET ACS is echo-space matched, and therefore, distortion matched to the accelerated EPI data (Polimeni et al. 2016).

2.1.3. Laminar fMRI

Laminar or cortical depth-dependent fMRI (Koopmans, Barth, and Norris 2010; Polimeni et al. 2010a; Olman et al. 2012; Ress et al. 2007; De Martino et al. 2013b; Huber et al. 2014; Muckli et al. 2015; Fracasso et al. 2018; Zimmermann et al. 2011; Kok et al. 2016; Gati and Menon 2002) is a recent and fast-growing analysis paradigm in functional imaging of human brain. Enabled by small-voxel fMRI acquisitions, this new paradigm has significantly expanded the type of neuroscientific questions that can be investigated in vivo in humans. Laminar or depth-dependent fMRI not only allows for probing laminar and columnar patterns of neuronal activations within the cortex, but it can also be applied to study functional activations with systematic change across cortical depth. Nevertheless, due to insufficient tissue contrast in functional images and also relatively large voxel sizes, precise delineation of cortical depths is still challenging.

The systematic variation of cortical layers position as a function of cortical folding pattern is well-known. The supragranular (uppermost) layers are compressed in gyri and expanded in sulci, whereas the infragranular (lowermost) layers are compressed in sulci and expanded in gyri. An exaggeration of the Layer IV curvature is caused as the result of such expansion and compression, which in return causes its depth to vary as a function of the curvature of the cortical ribbon (Hilgetag and Barbas 2006; Bok 1929; Van Essen and Maunsell 1980). Therefore, in contrast to calculating the cortical depth for any given voxel, which is straightforward given a gray matter segmentation, estimating the position of cortical layers is relatively difficult. When investigating functional differences between putative cortical layers, their anatomical position within the cortex should, therefore, either be imaged directly or inferred based on the cortical folding pattern.

Solving the Laplace equation in the cortex is one of the early approaches to cortical depth definition that takes into account the geometry of cortical folding pattern. Nevertheless, it does not align well with the position of the cortical layers within the cortex (LePrince et al. 2015; Waehnert et al. 2012; Annese et al. 2004). Curvature regression, in which the strong (negative) correlation between the height of Layer IV relative to the white matter boundary

and the signed mean curvature of the cortical folding pattern is exploited is another approach for estimating layers position. A more recent approach to define cortical layer positions based on Bok principle (Bok 1929) (a.k.a. equivolume sampling) has been computationally implemented and compared to the Laplace equation and to sampling simply by cortical depth (a.k.a. equidistant sampling); the equivolume sampling was reported to provide a more accurate prediction of the layers position (Waehnert et al. 2014). Other studies using diffusion imaging data (Kleinnijenhuis et al. 2015) as well as high-resolution multi-modal anatomical data (Waehnert et al. 2016) have also reported the equivolume sampling to perform better compared to the other approaches. Although equivolume sampling has shown to provide more accurate predictions of cortical layers compared to other approaches such as equidistant sampling, it still has some inaccuracies. For instance, it has been demonstrated that this approach can generate predictions of Layer IV position in primary visual cortex that deviate systematically across subjects (Hinds et al., 2015; Tardif et al., 2013).

2.2. Methods

2.2.1. Subjects

For testing each sequence and investigating its validity in the context of laminar imaging five healthy adult volunteers were scanned for each of the sequences mentioned below after providing informed consent. All measurements discussed below were performed on a 9.4 T MRI scanner (Siemens Healthcare, Erlangen, Germany) using a custom-built 16 channel transmit array combined with a 31 channel receive helmet (Shajan et al. 2014).

2.2.2. Visual Stimulation

Ocular dominance columns (ODCs) with their periodic left-right stripes organisation are amongst the most distinct architectures within the cortex. They are primarily activated by visual input either from the right or from the left eye (Cheng, Waggoner, and Tanaka 2001). Therefore, in this study ODCs were chosen as cortical landmarks with distinctive anatomical structures for evaluating the performance of sequences and fine-tuning their parameters in terms of specificity and sensitivity to neural activation. A semicircular checkerboard pattern was used as the visual stimulus to activate ODCs. The details of the stimulus have already been explained in another study conducted at 9.4T (Loureiro et al. 2017). To be able to map the activation of ODCs we placed sagittal slices orthogonal to Calcarine Sulcus (CS)

covering superior and inferior lips of CS, in which case the mapped ODCs would appear as alternating stripes that terminate near the V1/V2 borders (Cheng, Waggoner, and Tanaka 2001).

2.2.3. Anatomical Imaging

MP2RAGE

All measurements were conducted on a 9.4 Tesla whole-body MRI scanner (Siemens, Erlangen, Germany) using a custom-built head coil with a 16-element dual row transmit array and a 31-element receive array (Shajan et al. 2014). Whole-brain T1-weighted anatomical images were acquired for each subject using a MP2RAGE sequence (Marques et al. 2010; Hagberg et al. 2017) (TR = 6000 ms, TE = 3 ms, voxel size 0.6 x 0.6 x 0.6 mm, matrix = 352 x 352 x 256), yielding two inversion contrasts (flip angle 1 = 5°, flip angle 2 = 9°, T11= 800 ms, T12 = 2000 ms). MP2RAGE data was reconstructed offline (Scheffler and Ehses 2016; Marques et al. 2010) and was further processed (Fujimoto et al. 2014) using custom software developed in MATLAB (The Mathworks, Natick, MA).

The offline reconstruction included a correction for residual transmit field variation using the measured transmit field map with AFI described as follows. Actual flip angle mapping (AFI) as one of the B1+ mapping methods (Yarnykh 2007; Yarnykh 2010; Pohmann and Scheffler 2013) was used to correct for geometric distortions and intensity biases, which are a major challenge for accurate tissue segmentation and surface reconstruction. Prior to MP2RAGE scanning, the reference voltage for the read-out pulse was set to attain the nominal value at the level of the anterior commissure. This information was gained by the AFI method with the following parameters: Nominal FA=60°; TR1/TR2=20/100ms; TE=7ms, voxel size=3x3x5mm³; TA=3min 45s. By applying AFI correction to MP2RAGE image, we were able reduce the effect of B1+ field variations on intensity biases (Figure 1), which played a significant role in increasing the accuracy of surface reconstruction derived from MP2RAGE.

Inversion-Recovery EPI (IREPI)

Having anatomical data that is geometrically identical to the functional data provides a way to localize brain activations across cortical layers with higher spatial accuracy than what can be achieved with a geometrically dissimilar anatomical template. To achieve this, we acquired anatomical images with high tissue contrast and similar distortion to the functional images using inversion-recovery time EPI, thereby eliminating the need to un-distort the fMRI data.

Our goal was to obtain a full brain image at 1 mm³ isotropic resolution in less than 3 minutes that can be automatically segmented by FreeSurfer.

To be used for surface reconstruction, T1w EPI acquisition must have not only suitable tissue contrast but also adequate spatial resolution to segment the cortical gray matter and to generate accurate surface reconstructions. Therefore, we used voxel size of 1 mm³ isotropic for structural EPI acquisition as recommended for adult human brains (Glasser et al. 2013; Lusebrink, Wollrab, and Speck 2013). We developed parameters of the anatomical EPI protocol to have the same slice prescription, phase-encoding axis, and phase-encoding direction as the functional EPI protocol. EPI echo spacing and field-of-view (FOV) was set to ensure matching distortion.

2.2.4. Functional Imaging

MZBOLD-PSF

Detailed descriptions of the MZBOLD-PSF sequence and the specific parameters used therein are provided in chapter 3, Material and Methods, "Laminar Responses to Visual Motion and Pursuit Integration in Human Areas V3A and V6 Measured Using 9.4T fMRI", sections "Data Acquisition and Image Reconstruction" and "Preprocessing and Statistical Analysis of Functional Volumes, Point-Spread Function Correction (PSF) of the EPI Images".

Zoomed-PSF

To obtain high-resolution functional images with less distortions and low parallel imaging factors we combined zoomed imaging with PSF techniques (zoomed-PSF) (Bause 2015); the former allows for high resolution imaging within a limited field-of-view (FOV), whereas the latter allows for correction of distortions. Without the need for high parallel imaging acceleration we were able to keep TE in the range for optimal BOLD contrast at 9.4T by using 50% shorter echo train. On the other hand, zoomed-PSF technique comes with higher absorption rates as the results of additional saturation pulses and the need for a separate reference scan. A 30 ms SKEWED pulse (Pfeuffer et al. 2002; Hwang, van Zijl, and Garwood 1999) was used in a GRE-EPI and a PSF mapping sequence for outer-volume signal suppression. Imaging parameters were: voxel size: 0.8 mm³, TR = 3120 ms, TE = 23 ms, FOV = 70 x 141 mm², GRAPPA = 2, and Partial Fourier of 6/8. To measure point spread function we used a separate scan before each fMRI experiment with the same imaging parameters.

bSSFP

We used a 3D passband bSSFP sequence adopted to 9.4T (Scheffler and Ehse 2016) to acquire functional data. Using a sufficiently short multiline readout we were able to minimize distortions without increased blurring in the phase-encoding direction (PED). Imaging parameters were: voxel size = 0.8 mm³, TR = 3.8 ms, matrix = 230×230×18, Field-of-View (FOV) = 12°, band-width = 990 Hz, and Partial Fourier = 0.625.

FLEET

Detailed descriptions of the Fast Low-Angle Excitation Echo-Planar Technique (FLEET) sequence and the specific parameters used therein are provided in chapter 4, Material and Methods, "Real World Motion Processing in MT, PMST, and V1. A Laminar fMRI Study at 9.4T", section "Data Acquisition and Image Reconstruction".

2.2.5. Depth-Dependent Analysis

Equidistant (i.e. cortical depth preserving) depth sampling and equivolume (i.e. cortical layer volume preserving) layer separation (Waehnert et al. 2014) models have been applied in fMRI studies (Polimeni et al. 2010a; Kok et al. 2016; Huber et al. 2015). Equidistant models keep a specified relative cortical depth level to the cortex boundaries i.e. for a specific relative depth level, the absolute distance at a local region is obtained by multiplying the depth level by the local cortical thickness. It is known, however, that cortical layers are not positioned at fixed distances relative to white matter and pial surface (Bok 1929) as suggested by equidistant models, but rather the ratios of the volumes of different layers remain constant throughout the cortex (Waehnert et al. 2014). Therefore, in equivolume models the width of each layer can mathematically be related to the curvature of the cortex at that location (Kleinnijenhuis et al. 2015; van Mourik et al. 2019), creating layers that are thin at low curvatures and thick at high curvatures. To determine whether either of these approaches would resolve depth-dependent responses with more precision, we used both equidistant and equivolume models.

Anatomical and functional sequences used to generate depth profiles are described in detail in chapter 3. To compute the relative contribution of each cortical layer to the functional signal of each voxel, we first used an interpolation method, in which time series statistics of

each voxel in the functional volume were transferred to the eleven surfaces reconstructed from the anatomical MP2RAGE image. The transformation produced from the functional-to-anatomical registration was used to project the functional signal of each voxel intersecting a surface onto the corresponding surface using nearest-neighbor interpolation. As the second approach, once the three equivolume gray matter layers (superficial, middle, and deep) were defined and the proportion of each voxel's volume in these layers was determined by layer weights, these weights were subsequently used in a spatial regression approach to determine layer-specific time courses of the blood-oxygen-level dependent (BOLD) signal (van Mourik et al. 2019). To unmix the activation signals from different layers, a general linear model (GLM) of spatially distributed responses was used.

For both equidistant and equivolume models, FreeSurfer (Dale, Fischl, and Sereno 1999) was used to generate surface reconstructions of the interface between white matter and gray matter (white surface) and between gray matter and CSF (pial surface) from 0.8 mm³ MP2RAGE data, and to create cortical thickness maps from these boundaries (Fischl and Dale 2000), using a modified reconstruction stream adapted for MP2RAGE (Fujimoto et al. 2014).

Equidistant Model

Following the method described in (Polimeni et al. 2010a), depth-dependent sampling of voxel-wise GLM results was performed by generating nine additional surfaces within gray matter at fixed relative distances from white matter and pial surface derived from cortical thickness. Thus, in total eleven surfaces corresponding to white matter surface, pial surface, and nine equally spaced intermediated surfaces were created for each subject and each hemisphere.

To align functional volumes to the surface reconstructions generated from MP2RAGE anatomical data a boundary-based registration method (Greve and Fischl 2009) was used to first identify the WM-GM boundary in the EPI data and then register this interface to the corresponding surface reconstruction in the anatomical image using a rigid transformation. Using the transformation generated from registering functional volumes to anatomical image time series, statistics of each voxel were transformed (or resampled) by nearest neighbor interpolation to the collection of surface reconstructions intersecting that voxel. When the size of the fMRI voxel is greater than the spacing between mesh vertices, which is the case in

this study, nearest neighbor interpolation works reasonably well in mapping the functional signal onto the surface reconstructions.

Equivolume Model

To define equivolume layers, we followed (Kok et al. 2016) method to create two intermediate surfaces between white matter and pial surface yielding three equivolume layers within the gray matter and five cortical compartments i.e. white matter, CSF, and three intermediate layers. A layer is the volume between two neighboring surfaces. Following this, four level set functions were calculated to determine the distance of each functional voxel to the four boundaries between five cortical compartments. Based on these level set functions, the distribution of each voxel's volume over the five cortical compartments was calculated (van Mourik et al. 2019) providing the basis for a laminar GLM.

To align functional volumes to these surface boundaries we used a rigid boundary-based registration (Greve and Fischl 2009) followed by a recursive boundary based registration (rBBR) (van Mourik et al. 2019) that was recursively applied to increasingly smaller portions of the cortical mesh. In each iteration, the cortical mesh was split in two along the cardinal axes such that the number of vertices was equal for both parts, then the optimal BBR was found and applied to the respective parts. We repeated the iteration four times using affine BBR with seven degrees of freedom: translation and rotation along x, y, and z axis, and scaling along phase encoding direction.

For each functional ROI, i.e. V3A, V6, and V7, a matrix was generated to identify its layer-volume distribution: distribution of white matter, CSF, and three intermediate layers over n voxels within that ROI. This matrix was then used to unmix the contributions of different layers to each voxel's signal according to its layer-volume distribution using a spatial General Linear Model (GLM) (van Mourik et al. 2019), as follows:

$$W = X \cdot V + E$$

Where W is a $[n \times 1]$ vector representing voxel values (contrast estimates from our fMRI GLM analysis) within each ROI, X is the $[n \times 5]$ matrix representing the distribution of 5 layers within each voxel volume (as explained above), E is a $[n \times 1]$ vector of error terms denoting deviations from least square estimates, and V is a $[5 \times 1]$ vector of laminar signals. By regressing W against V , five laminar signals were generated for each ROI.

2.3. Results

2.3.1. Anatomical Imaging

MP2RAGE

AFI correction has shown to yield highly reliable results within an acceptable measurement time at 9.4T (Pohmann and Scheffler 2013). By applying AFI correction to MP2RAGE image, we were able to reduce the effect of B1+ field variations on intensity biases (Figure 1), which played a significant role in increasing the accuracy of surface reconstruction derived from MP2RAGE.

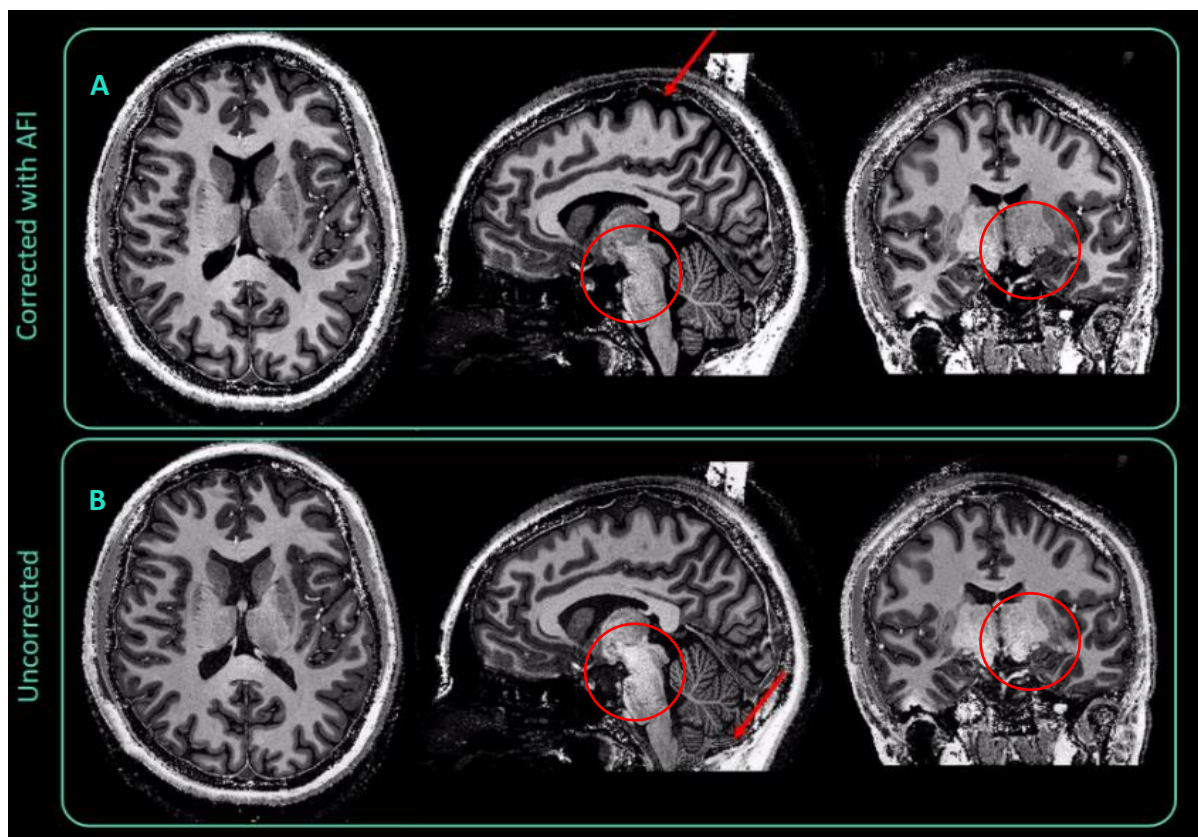


Figure 1. MP2RAGE image of one representative subject (A): corrected with AFI and (B): uncorrected. Circles point to areas where the effect of AFI correction in improving intensity homogeneity is most evident, arrows point to areas with more accurate tissue classification as the result of AFI correction.

Inversion Recovery EPI (IREPI)

It has been shown that depth-dependent functional information is best preserved if data analysis is performed in the original functional data space (Kashyap et al. 2016). By using

inversion recovery EPI, which is distortion matched to the structural image for surface reconstruction we aimed at eliminating the need to un-distort the fMRI data and performing the analysis in the native functional space. However, due to high degree of residual distortions, especially at air-tissue interfaces, we were unable to perform tissue segmentation and to initiate surface reconstruction. Nevertheless, our result demonstrates the first attempt towards generating IREPI image at 9.4T and achieving image quality sufficient for laminar analysis at UHF.

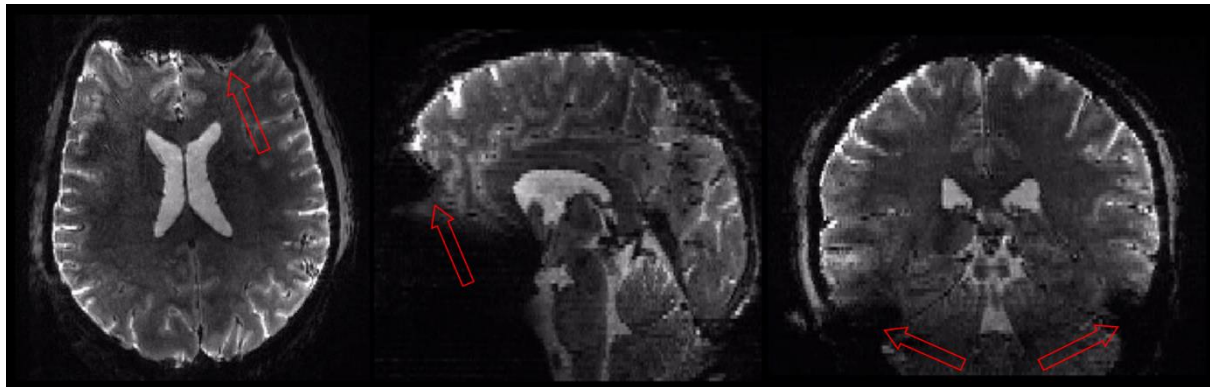


Figure 2. Axial, sagittal, and coronal view of Inversion recovery EPI (IREPI) in one representative subject demonstrating the current-state-of-the-art for IREPI imaging at 9.4T. Arrows point to residual distortions, which are more prevalent at air-tissue boundaries, and are the main obstacle in accurate segmentation of the IREPI data.

2.3.2. Functional Imaging

Zoomed-PSF

It has been shown that application of PSF correction with zoomed sequence results in stronger activations and a higher number of activated voxels (Bause 2015). The higher activation observed in zoomed images with PSF correction could be explained by reduced partial voluming of signal from activated voxels with signal from cortical areas with lower response to the stimulus than in distorted images. Bause et al., have also reported higher level of noise in PSF corrected zoomed images, possibly due to using high resolution data with less than optimal SNR for PSF map calculation. However, in our results we observed a shift in voxels position in the phase encoding direction (PED) after PSF was applied, which caused a mismatch between anatomical structure and functional signal.

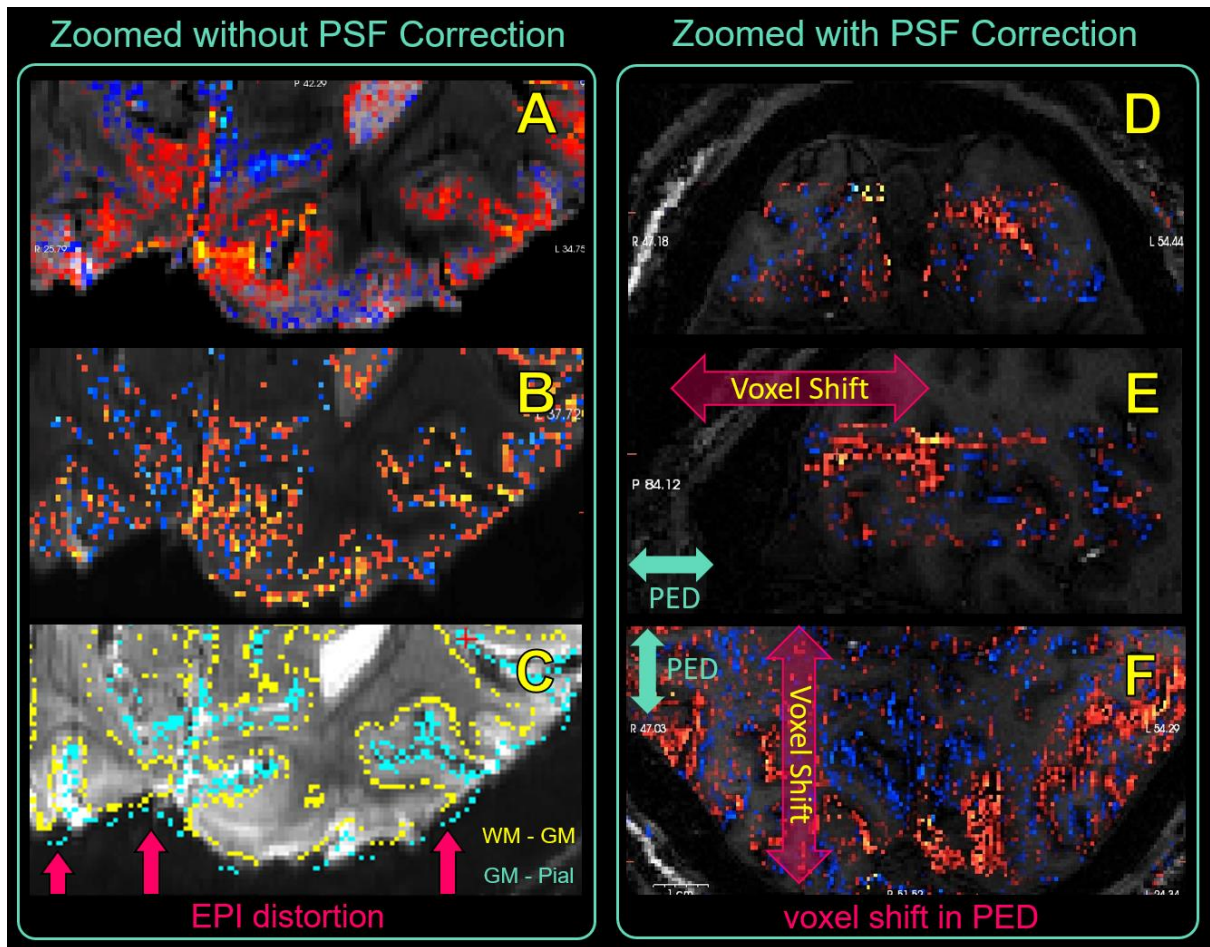


Figure 3. shows the BOLD activation maps of one example subject overlaid on top of the mean functional images (left column) and on the MP2RAGE image (right column) with and without point spread function (PSF) correction. (A-B): T1 activation maps in V1 without PSF distortion correction responding to checkerboard stimulus overlaid on top on the mean functional signal demonstrate lower noise level in activated areas. (C): white matter surface (WM-GM boundary) colored in yellow and pial surface (GM-pial boundary) colored in teal reconstructed from MP2RAGE image overlaid on top of the mean functional signal demonstrate a mismatch between anatomical and functional signal due to distortions not being corrected by PSF. (D-F): T1 activation maps with PSF correction in V3A/V6 responding to motion stimulus overlaid on top of the MP2RAGE image demonstrate a shift in voxel position in the phase encoding direction (PED) resulting in a distortion mismatch between functional and anatomical image.

2.3.3. Sequence Comparison at 9.4T

Comparison of different sequence, measurement parameters, and different post-hoc distortion correction methods demonstrated that: (1): bSSFP, although well confined to the stimulus area (high specificity) suffers from low SNR and, therefore, require more measurement time to reach a SNR level comparable to that in EPI data. (2): Using Foot-Head (FH) phase encoding generates activations with higher SNR compared to Posterior-Anterior (PA) due to shorter readout, faster TR, and less partial Fourier effect. (3): FLEET with post-hoc distortion correction (FSL topup) generated significantly more accurate results compared to MzBOLD sequence combined with PSF distortion correction. FLEET with PA phase encoding direction, and topup post-hoc distortion correction yielded results with the highest sensitivity and specificity, which is crucial in the context of laminar analysis of functional data.

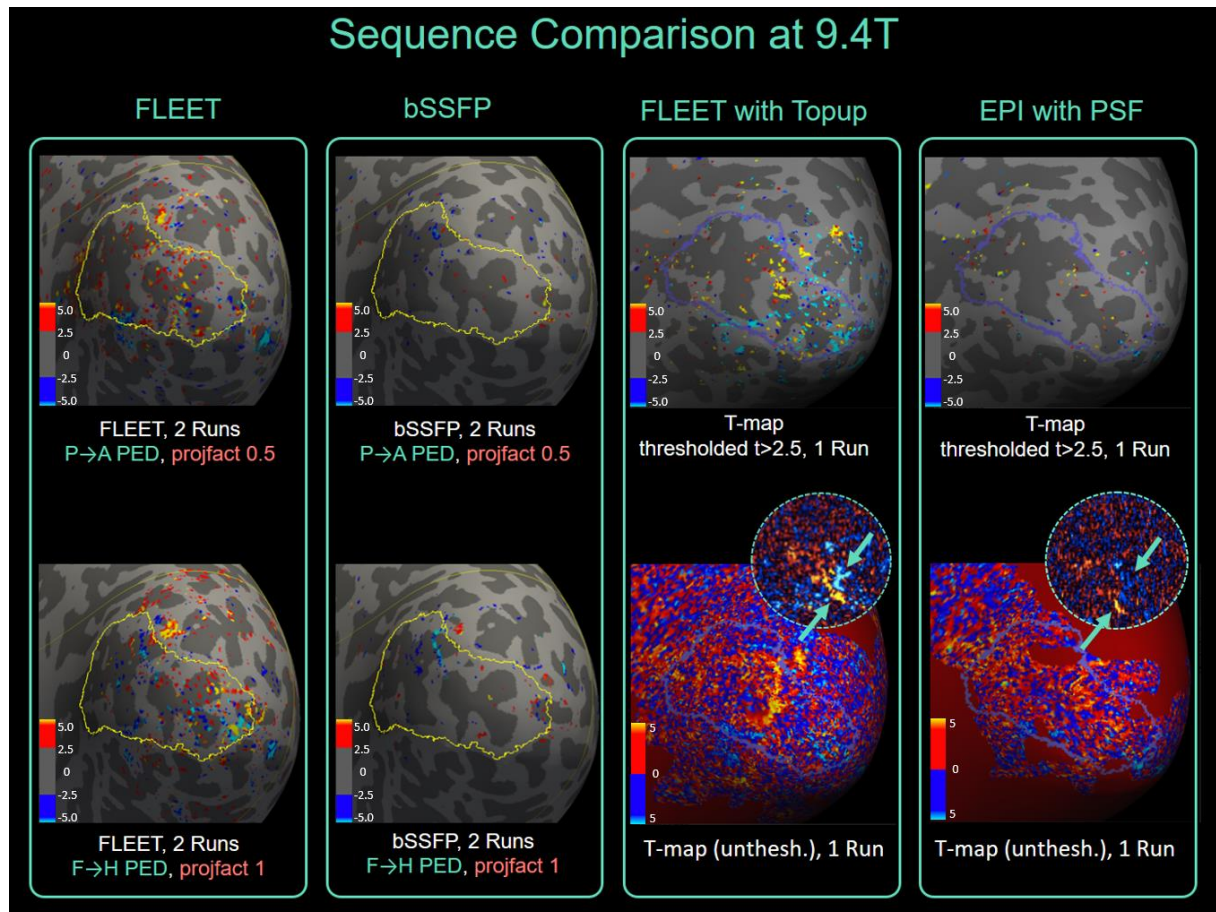


Figure 4. Effect of sequence, its parameters, and distortion correction method on the sensitivity and specificity of the functional data in an attempt to find the functional paradigm best suited for accurate laminar analysis of functional activity. Yellow and blue lines

demonstrate V1 boundaries, activations are produced in response to a checkerboard paradigm (described in "Methods" section).

2.3.4. Depth-Dependent Analysis of fMRI Data

Here we discuss depth-dependent profiles of the two main motion types we have been focusing on in this study i.e. retinal and objective motion in three regions of interests (ROIs) i.e. V3A, V6, and V7. Unlike V3A and V6, which are more responsive to objective motion compared to retinal motion, V7 was included as a ROI with no functional preference for either retinal or objective motion to be able to have a more precise comparison between the two mapping methods such that the observed shapes of laminar profiles across cortical depth are not driven by functional preference of these areas over either of the motion types. However, our objective is not to examine these profiles per se nor to investigate what are the neuronal processing driving them. These subjects will be discussed in detail in chapter 3. Our goal here is to compare the performance of the two methods we used to generate depth profiles: (1): interpolation to map voxels signal onto surfaces reconstructed from equidistant model, and (2): spatial GLM to map voxels signals onto surfaces reconstructed from equivolume model. When using either of these methods, the overall shapes of depth profiles were quite similar, i.e. an increasing trend towards shallow depths, regardless of the motion type or the region of interest (Figure 5) and its functional preference. The same overall agreement between the depth profiles generated by the two methods was observed when the profiles were detrended i.e. removal of the overall mean and linear trend across depth/layers to account for signal bias towards superficial layers in GE-EPI acquisitions caused by draining veins present on cortical surface (Figure 6). Nevertheless, in V6 a dip in the middle layers both in normal and detrended profiles was observed when using interpolation combined with equidistant surfaces, which was absent in depth profiles generated by spatial GLM combined with equivolume surfaces.

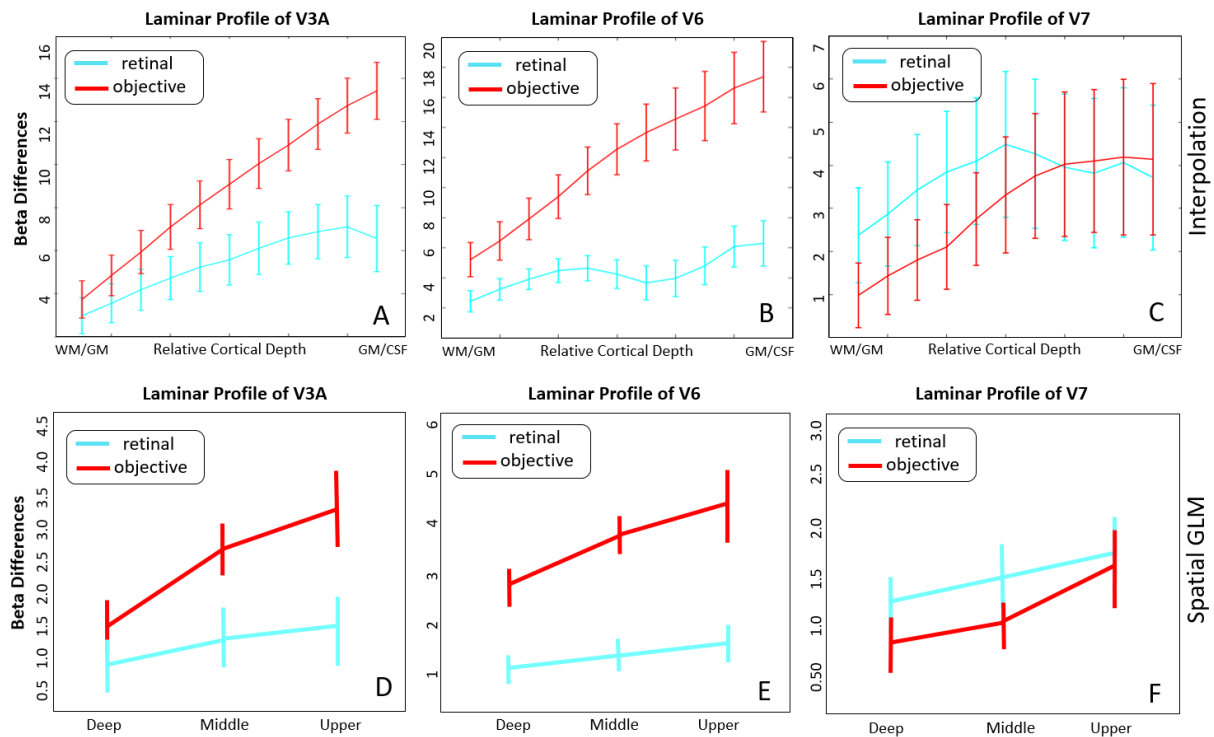


Figure 5. Laminar profiles of each ROI in response to retinal and objective motions (details described in chapter 3 "Methods" section). (A, B, C) Laminar response profiles of V3A, V6, and V7 to retinal and to objective motion using nearest neighbor interpolation to map functional signal onto surface reconstructions with equal distances (equidistant). (D, E, F) Laminar response profiles to retinal and to objective motion for the same regions using spatial GLM to map functional signal onto surface reconstructions with equal volumes (equivolume). Error bars represent SEM across subjects.

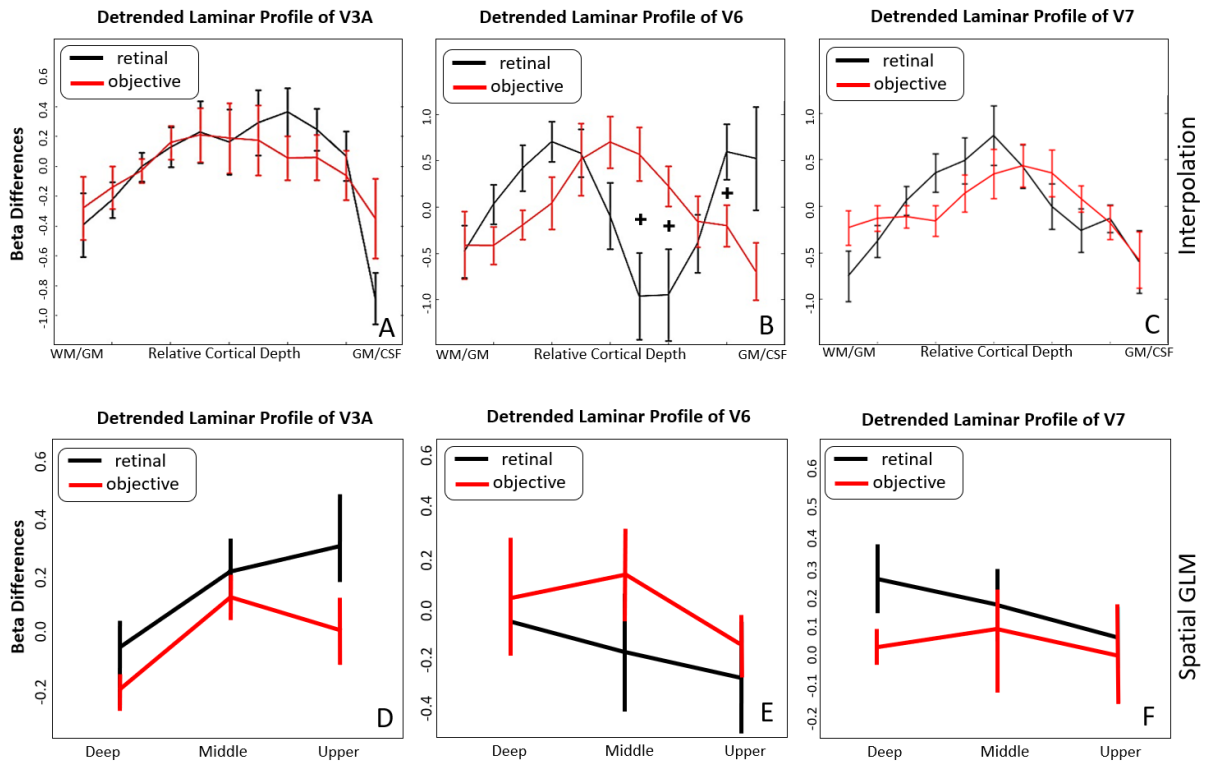


Figure 6. Detrended laminar response profiles (normalized by removal of the overall mean and linear trend across depth/layer) of each ROI in response to retinal and objective motion (details described in chapter 3 "Methods" section). (A, B, C) Detrended response profiles of V3A, V6, and V7 to retinal and to objective motion using nearest neighbor interpolation to map functional signal onto surface reconstructions with equal distances (equidistant). (D, E, F) Detrended laminar response profiles to retinal and to objective motion for the same regions using spatial GLM to map functional signal onto surface reconstructions with equal volumes (equivolume). Error bars represent SEM across subjects. Statistical tests were post-hoc t-tests conducted at each depth level between values of retinal and objective motion, correction refers to the number of depth levels for 2-way ANOVA analyses. \pm : $p < 0.05$ uncorrected (see chapter 3 "Methods" section for details).

2.4. Discussion

2.4.1. Sequence Development for Laminar Imaging

Inversion Recovery EPI (IREPI)

It has been shown that, compared to the conventional approach using MP2RAGE anatomy, higher spatial accuracy in cortical layer definition and better preservation of the depth-dependent functional information could be achieved if data analysis is performed in the

original space of functional data (Kashyap et al. 2016). Spatially accurate anatomical definition of cortical layers has been one of the significant challenges in depth-dependent fMRI studies. Inversion recovery preparation (Clare and Jezzard 2001; Gowland and Mansfield 1993; Ordidge et al. 1990a; Stehling et al. 1990) as a suitable method for fast T1 mapping has been used to acquire EPI images with identical readouts as the anatomical data. Multiple inversion-recovery time EPI (MI-EPI) at UHF-fMRI studies (Renvall et al. 2016) can yield high tissue contrast similar to MP2RAGE but with the advantage of being distortion-matched to the fMRI data. A clear advantage of MI-EPI approach, especially for depth-dependent fMRI studies in which accurate registration and minimal post-processing of the functional data is critical, is the achievement of more accurate registration with the distortion-matched anatomical reference and also foregoing the need of fMRI distortion correction. Another advantage of using this method is prevention of depth-dependent information loss by limiting the potential blurring associated with distortion correction. However, this approach comes at the cost of much lower fMRI temporal resolution compared to an EPI acquisition. To achieve this, we acquired anatomical images with similar distortion to the functional images using inversion-recovery time EPI, thereby eliminating the need to un-distort the fMRI data. However, due to residual distortions still being present in the data and the contrast not being sufficient (Figure 2) to identify tissue boundaries and, therefore, to perform a segmentation, the IR-EPI could not be used.

Zoomed with PSF Distortion Correction

Distortions and signal dropouts, especially in areas with strong susceptibility differences like tissue and air interface, are amongst the most prominent artifacts in EPI imaging. The higher the strength of the MR field, the stronger these artifacts become. The same is with readout duration i.e. longer readout times result in higher artifacts. Pixel shift correction in image space using a point spread function (PSF) map . On the other hand, a reduction in echo train is often required at high field to obtain an optimal BOLD contrast. Combination of partial Fourier sampling with large parallel imaging factors is the most common approach for Cartesian trajectories. Another method to reduce the time to k-space center is zoomed imaging (Pfeuffer et al. 2002; Heidemann et al. 2012), in which reduction of the field of view (FOV) in phase encoding direction (PED) is combined with suppression of signals from outside of the volume of interest. In this study we combined PSF technique with zoomed imaging to

be able to obtain high resolution data from a spatially limited area with high SNR but also to reduce the distortion in functional images. We used zoomed sequence with and without PSF to investigate the effect of PSF in correcting the distortions, and to examine whether or not its performance was accurate enough to be used for depth-dependent fMRI analysis. Without PSF correction, the distortions in the zoomed images resulted in a clear mismatch between functional and anatomical image (Figure 3.A-C). When using PSF, voxels in the distorted regions are shifted such that a spatial correspondence between voxels in functional and anatomical space is met. Nevertheless, when PSF was used to correct for distortions we observed a shift in voxels position in the phase encoding direction that did not lead to an accurate correspondence between functional and anatomical scans (Figure 3.D-F). The distortions in the zoomed images and the absence of correspondence between zoomed-PSF and the structural image becomes even more crucial when functional data is to be mapped across cortical depth. Therefore, we concluded that further development was needed to be able to use zoomed-PSF for depth-dependent fMRI studies.

Balanced Steady-State Free Precession (bSSFP)

Balanced Steady-State Free Precession (bSSFP) acquisitions can be made to be sensitive to BOLD signal changes (Scheffler et al. 2001; Bowen, S Menon, and Gati 2005; Miller et al. 2003), they can also have signal refocusing characteristics that make bSSFP a T_2 weighted acquisition (Scheffler and Hennig 2003; Miller et al. 2007; Kim et al. 2012). It has been shown that, similar to spin-echo, BOLD fMRI measured with bSSFP sequence is primarily sensitive to extravascular signals changes around small microvessels and capillaries (Miller et al. 2007; Bieri and Scheffler 2007). Therefore, compared to GE-EPI, bSSFP is capable of measuring neural activity closer to the source (Norris 2012), which makes distortion-free bSSFP images a good candidate for accurate mapping of functional activation across cortical depth. Nevertheless, in a recent study comparing depth-dependent BOLD signal measured with GE-EPI and bSSFP, no significant difference in terms of sensitivity across cortical depth was found between the two (Polimeni et al. 2018). They showed that both GE-EPI and bSSFP provide robust BOLD responses well-confined to the cortical gray matter, and that in both acquisitions, percent signal change, noise standard deviation, and statistical significance all increase monotonically towards the cortical surface (shallow layers). They speculated that, using a short TR in bSSFP sequence was the most probable contributing factor in observing

the common pattern of signal increase as voxels approach the pial surface. Future investigations are, therefore, required to investigate the effects of TR on the cortical depth profiles of BOLD signal measured with bSSFP. Nevertheless, in this study due to very low SNR in bSSFP acquisitions and, therefore, the need for longer scan times, which is a significant challenge when it comes to ultra-high field imaging, in addition to other studies not being able to find a significant difference between depth profiles generated by GE-EPI and bSSFP (Polimeni et al. 2018), we concluded that bSSFP requires further development to be used for laminar analysis at high field.

Fast low angle excitation echo-planar technique (FLEET)

Fast low angle excitation echo-planar technique (FLEET) is used to reduce the sensitivity of echo-planar imaging (EPI) Auto-Calibration Signal (ACS) to respiration and motion, which is an essential element in fMRI analysis specially in the context of depth-dependent fMRI. FLEET can also improve image quality and temporal Signal-to-Noise Ratio (tSNR) of accelerated EPI time-series data. Such benefits have already been shown in both conventional-resolution 3T and high-resolution 7T EPI time-series data (Polimeni et al. 2016). In this study we used FLEET to measure functional activation in Ocular Dominance Columns (ODCs) in response to a checkerboard paradigm. Our goal was to investigate its performance in terms of sensitivity and specificity to other sequences in general and also in terms of accuracy of depth-dependent fMRI. We observed that compared to bSSFP and MZBOLD EPI, signals measured with FLEET had a significantly higher SNR. In terms of spatial accuracy, bSSFP and FLEET performed quite similarly; the activations were well confined to the stimulated area in both acquisitions. In comparison to MZBOLD EPI with PSF correction, however, FLEET with topup distortion correction performed significantly better; a shift in voxel position in the phase encoding direction was observed when PSF was used in combination with MZBOLD EPI. In conclusion, FLEET outperformed all the other sequences tested in this study in terms of specificity and sensitivity and was less prone to subject motion and respiration artifacts.

2.4.2. Depth-Dependent and Laminar fMRI

In this study we examined two different approaches to depth-dependent fMRI: first a surface-based model that uses interpolation to map the functional signal of each voxel to underlying surfaces intersecting that specific voxel, and second a so called spatial GLM model, where

each voxel's signal is composed of the weighted sum of the signal in deep, middle, and superficial 3D layers making up the complete volume of that specific voxel. There are advantages and disadvantages to each approach, the most important of which are discussed below.

Since the surface reconstructions generated by the equidistant model have the same mesh topology and a natural vertex correspondence, a cortical depth profile can easily be generated at any location along the cortex. Additionally, the vertex correspondence between these 2-dimensional surfaces enables them to represent the layered, three-dimensional structure of the cortex. A disadvantage to this approach, however, is that depending on coarseness of mesh and voxel size, a given voxel may be assigned to multiple surface reconstruction (large voxel size) or in case of coarse mesh resolution it can be omitted, that is not mapped onto any surfaces. In case of using nearest-neighbor interpolation for mapping voxels signal onto the surfaces and depending on the mesh resolution, an additional disadvantage is that there may be some lateral displacement of the voxel data causing a local shearing effect. Nevertheless, by ensuring a sufficiently dense mesh, both disadvantages can be addressed.

Projecting fMRI voxels onto the vertices of the surface mesh is a form of interpolation, which can locally alter the spatial structure of the fMRI data. Nearest-neighbor interpolation, which is the most common form of interpolation assigns voxel data to all vertices that it intersects. This works well when the size of the fMRI voxel is greater than the spacing of the vertices in the mesh. In the absence of such condition, nearest neighbor interpolation can result in some fMRI voxels lying between vertices being "missed" or not projected anywhere onto the mesh. Trilinear, in which each vertex is assigned a weighted sum of nearby voxel intensities or other higher-order interpolations can avoid some of the disadvantages of nearest-neighbor interpolation.

Spatial GLM, on the other hand, is useful when a common laminar signal can be assumed over a number of voxels that are large compared to the number of layers (3D volume between two adjacent surfaces). This approach offers a potential solution to the partial volume problem. In contrast to interpolation, spatial GLM decomposes the layer signals based on the distribution of voxel volume over the layers it intersects, which has been shown to retrieve more accurate results at coarser resolutions and to reduce the inherent blurring of laminar profiles (van Mourik et al. 2019).

Given the limited biological resolution of fMRI, if similar functional properties were detected across depths at a particular location of cortex this similarity could reflect either true functional similarity at the neuronal level or the limited spatial specificity of the BOLD response, i.e., the signals measured within small voxels sampling across cortical depths could be intrinsically coupled through the local vasculature. Baseline venous CBV (V_0) and relaxation parameters such as T_2^* , which can vary across cortical depths as well as draining of deoxygenated hemoglobin (dHb) from deeper to shallow and superficial layers of the cortex via ascending veins are the two main sources of vascular biases in depth-dependent fMRI studies using GE-EPI. To remove the effect of vascular biases and to disentangle the neuronal from the vascular contributions, a dynamic biophysical model is needed. Recent depth-dependent fMRI studies have taken initial steps towards building such models (Heinzle et al. 2016; Markuerkiaga, Barth, and Norris 2016). Different methods have been proposed to account for such biases across cortical lamina such as using division instead of subtraction of the depth-dependent profiles or normalizing spatial profile of contrasting stimulus conditions with each other (Kashyap et al. 2016). Since the response to each motion type had a different magnitude compared to the other two and we were interested in comparing their overall shape across depth we used detrending i.e. removal of the overall mean and linear trend across depth to account for biases described above and to be able to perform a more accurate comparison of depth profiles. Details of this comparison are described in chapter 3 "Methods" section.

2.5. Conclusion

In this study, we demonstrated that gradient-echo imaging can resolve cortical depth-dependent modulation of the BOLD signal. We also showed that the choice of sequence and acquisition parameters in fMRI imaging as well as processing techniques can significantly impact cortical depth profiles of the BOLD signal. We explored different models based on which cortical surfaces were reconstructed, i.e. equidistant and equivolume models, and based on which functional signal were mapped onto the surface reconstructions, i.e. interpolation or spatial GLM (Figure 5 and 6). Employing each model offers distinct advantages and disadvantages. The key, however, is that they perform in ways that respect the underlying functional and anatomical structure.

In short, this study presents the current state-of-the-art in acquisition and practical considerations for the analysis of high-resolution depth-dependent BOLD fMRI data at ultra-high magnetic fields. Enabled by advances in UHF-fMRI acquisition, the relatively recent possibility to sample fMRI signals across cortical depths presents both opportunities and challenges, as outlined above.

CHAPTER 3: Laminar Responses to Visual Motion and Pursuit Integration in Human Areas V3A and V6 Measured Using 9.4T fMRI

3.1. Introduction

Visual motion perception, contrary to our intuition, is only partly based on visual input. Non-visual cues such as efference copies from eye movements determine to an equal degree our perception of motion, or the lack of it. It is therefore the multi-modal integration of visual motion signals with non-visual cues that allows for a stable perception of the world and differentiation between self-induced motion and external (or real) motion (Gibson 1954; Royden, Banks, and Crowell 1992; von Holst and Mittelstaedt 1950a). If we want to understand mechanisms related to visual motion perception, we therefore have to understand those of multimodal motion integration. There are patients with parieto-occipital lesions with impaired integration who suffer of vertigo and nausea as they interpret self-induced motion as external motion (Haarmeier et al. 1997). Invasive electrophysiology in macaques has revealed several cortical regions containing varying fractions of so-called ‘real motion’ neurons, i.e. neurons whose response reflects motion in the environment even when it is cancelled on the retina by visual pursuit (Erickson and Thier 1991; Galletti et al. 1984, 1988, 1990; Ilg, Schumann, and Thier 2004). Such neurons were predominantly found in motion processing regions V3A, V6, MST, VIP and VPS, but were also present as early as V1 (Daddaoua, Dicke, and Thier 2014; Galletti et al. 1984, 1988; Dicke, Chakraborty, and Thier 2008; Troncoso et al. 2015; Zhang, Heuer, and Britten 2004) with corresponding responses in human V1-V3 (Nau, Schindler, and Bartels 2018).

In the human brain, only relatively few studies addressed the integration of pursuit eye-movements with retinal motion (Arnoldussen, Goossens, and van den Berg 2011; Nau, Schindler, and Bartels 2018; Fischer et al. 2012a). These studies showed that V3A stands out in a unique way, as it had overwhelming responses to objective planar motion while either lacking responses to retinal motion, with comparably weaker objective motion responses also in V6, which was additionally suppressed by planar retinal motion (Fischer et al. 2012a).

V3A and V6 project to and receive projections from various cortical as well as subcortical regions in both dorsal and ventral streams (Anderson and Martin 2005; Galletti, Battaglini, and Fattori 1990, 2001). These connections, including the ones to parietal cortex and in particular the smooth pursuit region of the frontal eye fields (Stanton et al. 2005a), have been

suggested to provide pathways for the eye movement signals to be conveyed to areas like V3A and V6 (Fischer et al. 2012a). One possibility is that signals of efference copies, real motion, and retinal motion are processed in segregated voxels in V3A and V6, as suggested by human fMRI study that found partially functionally segregated voxels whose response preference was either dominated by retinal or by real motion regardless of pursuit eye-movements (Arnoldussen, Goossens, and van den Berg 2011).

In the present study, we investigated the possibility that retinal, objective, and pursuit motion signals are segregated according to laminar depth in the cortex. Laminar organization of neuronal circuitry in the cortex involves feedforward, lateral, and feedback pathways (Larkum 2013a; Markov et al. 2014; Sillito, Cudeiro, and Jones 2006). In every cortical region, top-down feedback signals enter cortical regions from deep and superficial layers, whereas bottom-up feedforward signals target middle layers (Felleman and Van Essen 1991; Harris and Mrsic-Flogel 2013; Rockland and Pandya 1979; Wong-Riley 1978). If such mechanisms are at work for V3A and V6 with respect to retinal and pursuit or real motion signals, respectively, we would expect putative feedback-mediated responses in these regions during processing of real motion to result in a laminar activity profile that is distinct from the activity elicited by putative bottom-up input by retinal motion.

To test this hypothesis, we used high-resolution ultra-high field (9.4T) fMRI to quantify neural signals across cortical depth related to retinal motion, real motion, and pursuit in areas V3A, V6, and, as a control, in IPS-0 / V7. We used an established paradigm that allows for the reliable separation of neural signal related to retinal and real motion using a two-factorial pursuit paradigm on planar on-screen motion (Fischer et al. 2012a).

Recent studies using fMRI at ultra-high-field have provided direct evidence of the sensitivity of fMRI to capture neuronal processes at different cortical depths (Huber, Uludag, and Moller 2017; Kashyap et al. 2018; Kok et al. 2016; Trampel et al. 2017) and of different columns (Nasr, Polimeni, and Tootell 2016; Shmuel et al. 2010; Yacoub, Harel, and Ugurbil 2008b). High resolution imaging not only increases the proportion of voxels containing cortical gray matter but also significantly reduces contaminations related to physiological noise (Triantafyllou et al. 2005). Contribution of large draining vessels that introduce spatial bias to the BOLD signal by pooling deoxygenated blood away from the activated neuronal populations (Olman, Inati, and Heeger 2007) is reduced at high field, while functional signals originating from smaller vessels and capillaries are sufficiently enhanced to become

detectable (De Martino et al. 2012). With smaller voxel size biases introduced to the intracortical signal by surface vessels can be reduced (Baez-Yanez et al. 2017; Polimeni et al. 2010a). Recent developments in ultra-high field imaging hardware (Keil and Wald 2013) have helped to push parallel imaging acceleration factors, enabling shortening of the echo-train length and thereby reduction of image distortions (de Zwart et al. 2002; Polimeni et al. 2016) and signal dropouts (Merboldt, Finsterbusch, and Frahm 2000).

While our approach would hence allow for depth-resolved neuroimaging of higher-level motion regions, it is still a debated question in the field whether the vascular organization and its regulation allow for differential neural involvement across lamina to be reflected using current neuroimaging methods (Polimeni et al. 2018).

3.2. Methods

3.2.1. Participants

Eleven neurologically healthy adults (3 females, 8 males, mean age 32 years \pm 9 SD) with normal or corrected-to-normal vision volunteered to participate in the study. In accordance with the local research ethics committee requirements volunteers underwent a physical and psychological check-up by a local physician and provided written informed consent. All investigations were conducted in agreement with the Declaration of Helsinki and were approved by the ethics committee of the university clinics Tübingen. Prior to scanning, subjects were instructed on the experimental procedures and performed a test trial to get accustomed to stimuli and to the task.

3.2.2. Visual Stimulation and Experimental Design

Visual stimuli and paradigm were very similar to those used previously to identify retinal and real motion responses in V3A and V6 (Fischer et al. 2012a). In brief, stimuli consisted of randomly arranged black and white dots (size ranging from 0.1 to 1.1 deg) on a grey (90 cd/m²) background, presented at 100% contrast (i.e. maximal luminance for white dots and minimal luminance for black dots). The 320 visible dots yielded an average density of 0.75 dots/deg². The experiment included 4 conditions arranged in a 2x2 factorial design including 2 factors with 2 levels each. The two factors were pursuit (on/off) and 2D planar motion (on/off). 2-D planar motion was achieved by displacement of the entire dot field along the vertical and horizontal axes along a 2D sinusoidal trajectory with either 3 or 4 cycles per trial

(randomly assigned to x and y axes, respectively) and with random initial phases. Pursuit was implemented by moving the otherwise centrally presented fixation disc (that contained the fixation task, see Fixation Task below) along the same trajectory. When both pursuit and planar motion were 'on', the two were coupled, such that the fixation task moved together with the dots, resulting in zero planar retinal motion. The starting direction was randomized for each trial. The mean dot speeds for 2-D planar motion was 3.80 deg/s in all trials.

3.2.3. Procedure

Stimulus presentation followed a block design schedule where each of the four stimulus conditions was presented eight times with a duration of 12 s each. Hence, each of the four functional runs consisted of 32 full stimulus blocks. Different conditions were presented in pseudorandom sequences in which each condition was preceded equally often by all conditions. The stimulus was rear-projected using a linearized projector with a resolution of 1024 x 768 pixels at 60 Hz onto a screen located in the scanner bore. Subjects viewed the stimulus at 82 cm distance through a mirror mounted on the receive coil array, leading to a display size of 30*20 visual degrees. The stimulus was written in MATLAB 2010a (<http://www.mathworks.de/>) using the Psychophysics Toolbox 3 extensions (<http://psychtoolbox.org/>) and was presented using a Windows computer.

3.2.4. Fixation Task

Throughout the experiment subjects performed a character repetition-detection task on a fixation disc, ensuring fixation as well as balanced attention across conditions. A total of 26 characters were presented in random succession (1.6 degrees height, white) on a gray fixation annulus (2 width, 72 cd/m²), with random presentation times of 1-2.16 s. Subjects indicated character repetitions by button press.

3.2.5. Data Acquisition and Image Reconstruction

All measurements were conducted on a 9.4 Tesla whole-body MRI scanner (Siemens, Erlangen, Germany) using a custom-built head coil with a 16-element dual row transmit array and a 31-element receive array (Shajan et al. 2014).

For the acquisition of blood oxygen level dependent (BOLD) weighted images, we used PSF (Point Spread Function) corrected (In and Speck 2012) 2D gradient-echo EPI with 0.8 x 0.8 x

0.8 mm isotropic resolution and the following parameters (see section below for PSF correction details): TR / TE / flip angle = 2000 ms / 21 ms / 70 deg, field of view = 160 x 160 mm, matrix = 200 x 200, bandwidth = 1388 Hz / pixel, GRAPPA (Griswold et al. 2002) acceleration factor of 4, and partial Fourier of 6 / 8. The slices covered the dorsal part of the visual cortex and part of parietal cortex using 20 oblique-coronal slices positioned parallel to the calcarine sulcus. The number of slices was limited to 20 due to limits in the specific absorption rate (SAR). The wall-time for each run was 6 min and 36 seconds (396 s), including the initial 8 s block of dummy scans in the beginning of each scan to allow T1 steady state to be achieved, and 1 TR of reference scan. Functional images were reconstructed with the standard online Siemens EPI and GRAPPA reconstruction. Four functional runs each consisting of 203 volumes, including the four dummy scans and one reference scan, were obtained for each subject. For each run, automatic reconstruction of data acquisitions was done twice, once with PSF correction and once without PSF correction. PSF corrected images were used for the subsequent analysis.

Whole-brain T1-weighted anatomical images were acquired for each subject using a MP2RAGE sequence (Marques et al. 2010) (TR = 6 ms, TE = 2.3 ms, voxel size 0.8 x 0.8 x 0.8 mm, matrix = 256 x 256 x 192, PAT mode: GRAPPA 3, and 6/8 partial Fourier with POCS reconstruction), yielding two inversion contrasts (flip angle 1 = 4°, flip angle 2 = 6°, T1 = 900 ms, T2 = 3500 ms). MP2RAGE data was reconstructed offline using custom software developed in MATLAB.

3.2.6. Preprocessing and Statistical Analysis of Functional Volumes

Point-Spread Function Correction (PSF) of the EPI Images

Point-spread function (PSF) mapping is one of the promising methods for correcting geometrical and intensity-related distortions in Echo-planar imaging (EPI). Using acquisitions with additional phase-encoding gradients, PSF maps encode spatial information relevant to overall intensity distribution and geometrical distortion from a single voxel. These maps are then convolved with the distorted image in order to obtain PSF-corrected EPIs (Zeng and Constable 2002). We used PSF mapping to correct for (1): possible distortions in the EPI images that are related to field inhomogeneity, (2): eddy current effects, and (3): blurring due to image distortion. Pixel shifts in image space were corrected based on a PSF map (In and Speck 2012; Zaitsev, Hennig, and Speck 2004; Zeng and Constable 2002). The point spread

function was measured in a separate scan prior to each BOLD sequence using the same parameters as the EPI sequence. PSF shift maps in the non-distorted spin-wrap encoding direction (obtained online) were used to compute the average and the standard deviation of the shift values in the regions-of-interest (ROIs). Compared to distorted images, PSF-corrected activation maps were registered easier and with more precision to the anatomical images.

Preprocessing and GLM analysis

PSF corrected functional data were preprocessed and analyzed using the FreeSurfer functional analysis stream, FSFAST (<https://surfer.nmr.mgh.harvard.edu/fswiki/FsFast>). Preprocessing included motion correction of the functional volumes to the first volume of the first run, slice-timing correction, and co-registering functional images to the MP2RAGE. No spatial smoothing (volume- or surface-based) was applied to the data at any stage of the analysis.

A general linear model (GLM) including regressors for each condition as well as head-motion parameters was then fitted to the time course of each voxel. A second order polynomial function was used as a nuisance regressor to model low frequency drifts. The GLM analysis of the 2x2 factorial design allowed us to separate cortical responses related to the main factors of (a) eye-movements (active pursuit), (b) objective (2D planar) motion, and their interaction: (c) retinal motion. The main factor (b: 2D planar motion) and the interaction (c: retinal motion) were balanced for all effects of pursuit, hence cancelling effects related to motion of the screen edges induced by eye movements or to less accurate fixation during pursuit.

3.2.7. Definition of Regions of Interest

FreeSurfer surface-based analysis (Dale, Fischl, and Sereno 1999; Fischl, Sereno, and Dale 1999; Polimeni et al. 2018) was used to define the ROIs on the surface. For ROI definition only, fMRI data was smoothed (3 mm) on the surface – note that for ROI definition, neither cortical depth information nor ultra-high resolution were relevant. No smoothing, neither in the volume nor on the surface, was performed in any stage of the subsequent laminar analyses. We used a previously established motion localizer to localize V3A and V6 (Fischer et al. 2012a) as follows. Using the contrast ‘objective versus retinal motion’, V3A and V6 were

defined as voxels that had higher responses to objective (real) compared to retinal motion and that were located in the anatomical locations of the two regions known from prior studies as outlined below. In these prior studies, this contrast has led to selective activation of voxels overlapping with retinotopically defined V3A (Fischer et al. 2012a). V3A was located below the parietal-occipital sulcus (POS) and extended into the transverse occipital sulcus (TOS) coinciding with the anatomical landmarks previously reported for the V3A area (Pitzalis et al. 2006; Silver, Ress, and Heeger 2005; Tootell et al. 1997). The same functional contrast was previously shown to activate voxels overlapping retinotopically defined V6 (Fischer et al. 2012a), which is located in the dorsal part of the POS (Pitzalis et al. 2006, 2015). However, for V6 we cannot exclude the possibility that the neighboring retinotopic area V6A responded also to our localizer contrast. Recent studies reported that V6A also responded to visual flow fields (Pitzalis et al. 2013, 2015). We hence refer to this functionally defined region as V6+ to indicate that it includes V6 and possibly V6A.

In every subject the first functional run was used to localize V3A and V6+, and the remaining three runs were used for analysis.

In addition to investigating responses in V3A and V6+, which were the main focus of this study, we also identified area V7 (also referred to as IPS-0). V7 shares a common feature with V3A and V6, in that it, too, responds to coherent motion (Cardin and Smith 2011; Helfrich, Becker, and Haarmeier 2013) and eye movements (Schluppeck, Glimcher, and Heeger 2005). However, compared to V3A and V6, V7 has no or only small preference to objective motion compared to retinal motion (Nau, Schindler, and Bartels 2018; Fischer et al. 2012a). As it is also directly neighboring V3A and V6, and as it is located within the narrow field of view of our focused imaging sequence, we selected V7 as a control ROI to examine to which extent the pattern of results we find in V3A and V6 can be attributed to their overall preference to objective motion. To localize V7 we used maximum probabilistic maps (most probable region for any given point on the cortical surface) of the functional probabilistic atlas provided by the Kastner group (Wang et al. 2015), thresholded at 50 percent.

3.2.8. Depth Dependent Analysis

FreeSurfer (Dale, Fischl, and Sereno 1999) was used to generate surface reconstructions of the interface between white matter and gray matter (white surface) and between gray matter and CSF (pial surface) from 0.8 mm MP2RAGE data, and to create cortical thickness

maps from these boundaries (Fischl and Dale 2000), using a modified reconstruction stream adapted for MP2RAGE (Fujimoto et al. 2014). Following Polimeni et al. (2010), nine additional surfaces within gray matter at fixed relative distances from white matter and pial surface were then derived from cortical thickness maps (Polimeni et al. 2010a). Thus, in total eleven surfaces corresponding to white matter surface, pial surface, and nine equally spaced intermediate surfaces were created for each subject and each hemisphere (Figure 7).

Functional volumes were aligned to the surface reconstructions generated from the MP2RAGE anatomical data using a boundary-based registration method (Greve and Fischl 2009) that first identified the WM-GM boundary in the EPI data and then registered this interface to the corresponding surface reconstruction in the anatomical image using a rigid transformation. To map functional signal to the surface reconstructions we resampled GLM statistics of each voxel in the functional volume to the eleven surfaces reconstructed from the anatomical MP2RAGE image by nearest neighbor interpolation. When the size of the fMRI voxel is greater than the spacing between mesh vertices, which is the case in this study, nearest neighbor interpolation has been shown to work well in mapping the functional signal onto the surface reconstructions (Polimeni et al. 2018).

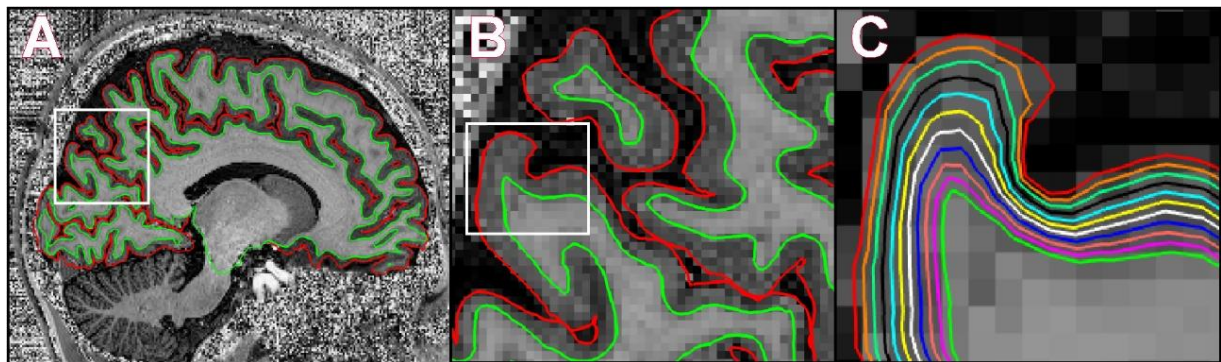


Figure 7. Laminar surface segmentation. (A) A T1w MP2RAGE image was used to segment the brain and to generate intermediate surfaces throughout the whole cortex. (B) The approximate location of V3A and V6 is magnified to illustrate the sections shown in (C). (C) Illustration of laminar depth-segmentation using nine surfaces between white-gray matter boundary and pial surface.

3.2.9. Statistical Analysis

Laminar signal was analyzed in three ways for each ROI. First, a two-way ANOVA compared signal intensities as a function of cortical depth (factor depth) and of experimental contrast (factor contrast: retinal motion, objective motion) using the GLM-derived contrast values.

Second, given the fact that contrast estimates for different signal types (retinal, objective) showed an increase from lower towards upper layers, we examined whether the slopes of this increase differed between signal types. The slopes were calculated by fitting a first degree polynomial function to eleven data points corresponding to the eleven laminar signals.

Third, we performed the above-described two-way ANOVA after detrending signal intensities across depth: given the known signal bias towards larger vessels in GE-EPI, signal increases towards superficial layers, and differences in signal slopes could be due to differential blood vessel distribution across the cortical depth and differences in proximity to the large surface vessels, rather than due to neural effects (or in addition to the latter). In an attempt to overcome this surface bias, we repeated the two-way ANOVA following linear detrending of laminar responses of retinal and objective motion. Using a linear regression, we removed constant and linear trends from the laminar profiles of each motion type and examined only the residual effects, now corrected for the overall linear signal increase across layers and for differences in mean signal amplitude. The analysis of the residuals would therefore reveal the uniqueness of condition-specific laminar profiles beyond surface-bias and mean differences.

3.3. Results

We used ultra-high field (9.4T) fMRI to examine laminar activation profiles of high level visual areas V3A, V6, and V7 in response to real world motion during pursuit eye movement in eleven human participants.

In the separate localizer runs, we were able to reproduce the previously reported response to objective and to retinal motion in V3A and V6 (Fischer et al. 2012a). Every subject revealed clearly localized clusters with objective motion preference in positions corresponding to typical locations of V3A and V6, as shown in Figure 8 for a representative subject.

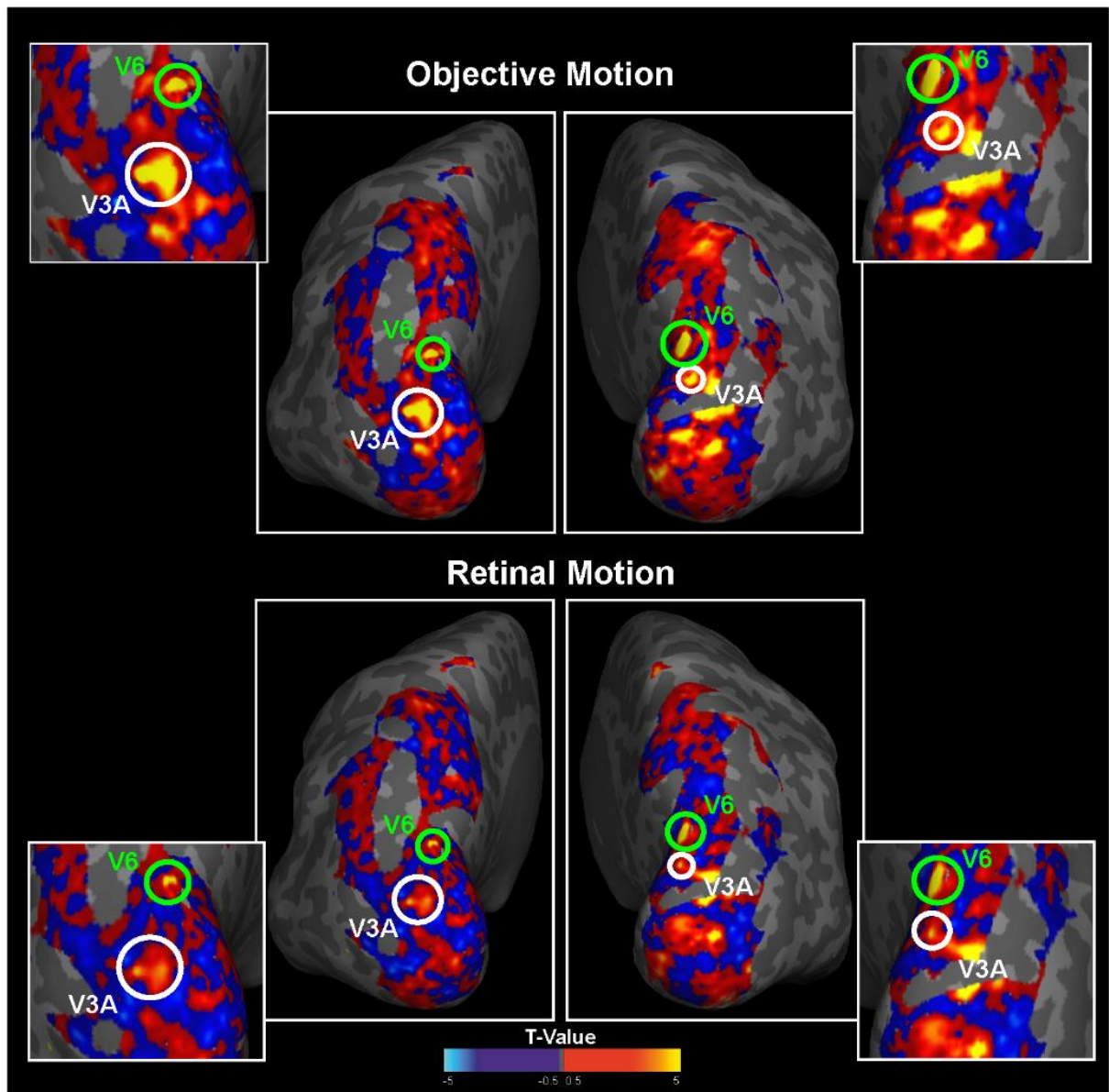


Figure 8. Responses of putative V3A and V6 to retinal and objective motion illustrated for one representative subject. For better visualization and more accurate estimate of ROI boundaries, smoothed (3mm) activations are shown.

3.3.1. Laminar Responses to Retinal and Objective Motion in V3a and V6

In both V3A and V6, net BOLD signal was higher during objective motion compared to retinal motion (V3A: $t(21)=-8.4724$, $p=3.24 \times 10^{-8}$, V6: $t(21)=-6.5727$, $p=1.64 \times 10^{-6}$). Similar to all results shown below, this result is based on the last three imaging runs and hence confirms the results from the first run that was used to select the ROIs based on this contrast.

The laminar profiles for retinal and objective motion differed in both ROIs, V3A and V6, as is evident in Figure 9 (A, B). The two-way ANOVA showed that there was a significant interaction between layer and experimental contrast in both regions (V3A: $F(10,210)=22.59$, $p<0.001$; V6: $F(10,210)=20.18$, $p<0.001$). For V3A, post-hoc paired sample t-test revealed a significantly stronger response to objective compared to retinal motion in the superficial layers, but not in the lower layers (upper layers: depth09: $t(21)=-3.1083$, $p=0.0053$, depth10: $t(21)=-3.2450$, $p=0.0039$, depth11: $t(21)=-3.8138$, $p=0.0010$; lower layers: depth01: $t(21)=-0.5874$, $p=0.5632$, depth02: $t(21)=-0.9541$, $p=0.3509$, depth03: $t(21)=-1.2492$, $p=0.2253$, depth04: $t(21)=-1.6243$, $p=0.1192$) (Figure 9A). In V6 the response to objective motion was significantly stronger than that to retinal motion across all layers, yet with larger differences in the middle and superficial layers (Figure 9B).

These results were also reflected in the slopes analysis, that showed significantly higher slopes in the objective motion compared to the retinal motion in both regions (V3A: $t(21)=-6.3167$, $p=2.0*10^{-6}$, V6: $t(21)=-5.6583$, $p=7.0*10^{-6}$).

We included V7 as a control ROI in order to test whether the higher bias for objective motion could also be observed in a region that has no overall higher signal for objective motion. V7 showed indeed no higher mean signal for objective compared to retinal motion (Figure 9C). Hence, if V7 showed an interaction between experimental contrast and depth this would speak for a genuine neural bias for objective motion in the upper layers.

Even though weak, the laminar results for V7 support the neural bias account. The ANOVA showed an interaction between layer and experimental contrast (Figure 9C) ($F(10,210)=2.62$, $p=0.0051$), which was driven by the steeper laminar response slope in V7 for objective compared to retinal motion ($t(21)=-1.8253$, $p=0.0822$). Note this can not be accounted for by higher responses to objective motion, as, to the contrary, retinal signal trended higher than objective motion in lower layers ($p<0.2$ at each layer).

The upper-layer response bias during objective compared to retinal motion processing in V3A and V7 hence lend support to the notion of a contribution enhanced neural activity that was more pronounced in upper layers during objective motion processing.

3.3.2. Laminar Response in V3A and V6 after Removal of the Mean Signal and the Linear Trend

Since all responses contained activity biases towards upper layers we wanted to perform an additional analysis that examined the underlying laminar response profiles after removal of each individual surface bias from each ROI and each condition.

Figure 9 (D, E, F) shows the laminar profiles of each ROI and motion type after removal of the linear trend and the overall mean signal. Two-way ANOVAs of the laminar signals revealed (1): a significant interaction between layer and motion type in V6 and a trend in V3A (V3A: $F(10,210)=1.59$, $p=0.0518$; V6: $F(10,210)=2.07$, $p=0.0045$), and (2): a significant interaction between layer and ROI for retinal but not for objective motion (retinal: $F(10,210): 4.02$, $p=0.0$; objective: $F(10,210): 0.86$, $p=0.5696$). Post-hoc paired-sample t-tests at each depth-level of each ROI revealed significant differences between laminar profiles of retinal and objective motion only in V6 at depths 7, 8, and 10 (depth 7: $t(21)=-2.6205$, $p=0.016$; depth 8: $t(21)=-2.39$, $p=0.0263$; depth 10: $t(21)=2.1663$, $p=0.0419$), showing that upper mid-layer response differences drove the interaction.

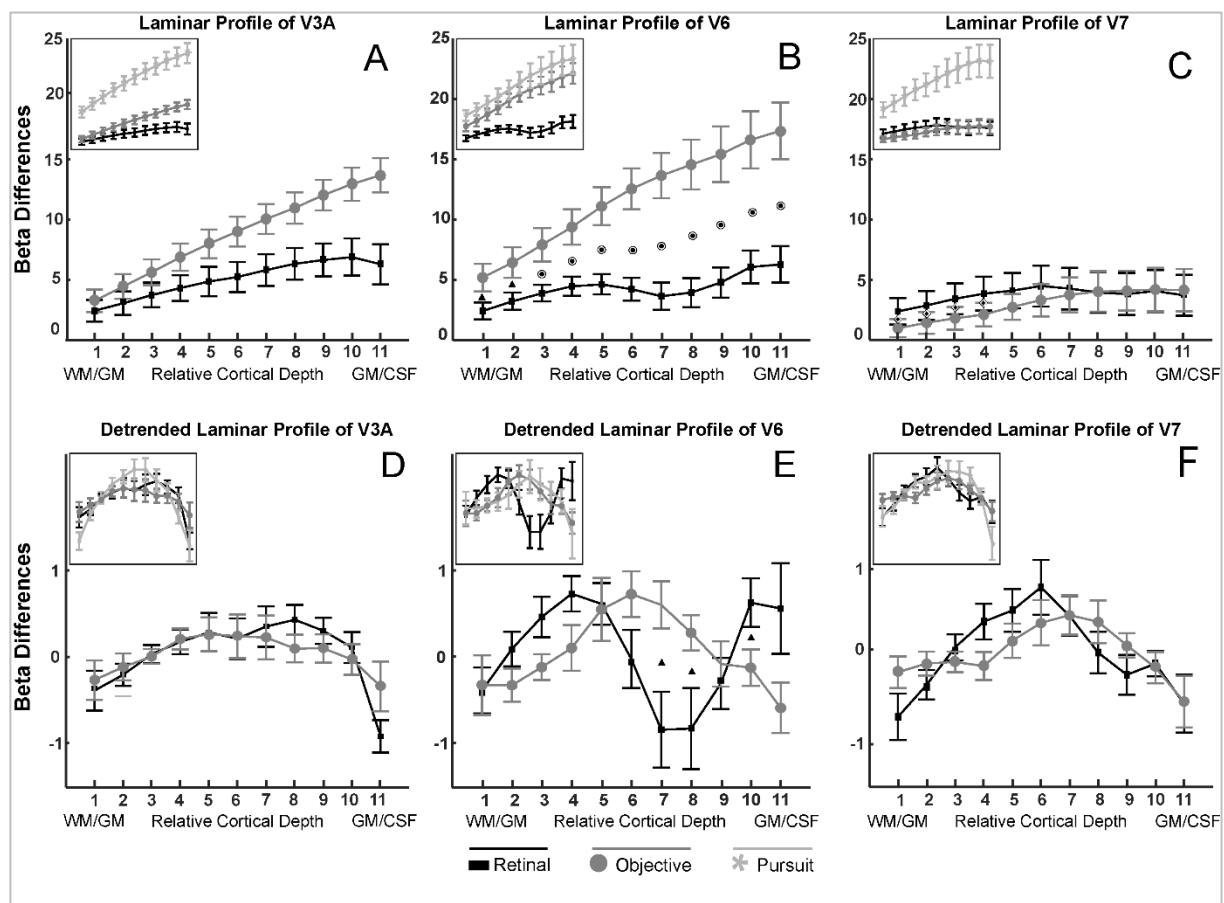


Figure 9. Laminar profile of putative V3A, V6, and V7 in response to retinal, objective, and pursuit motion. (A, B, C): laminar signals in response to the three motion types, (D, E, F): laminar signals from which the linear trend and the overall mean signal were removed. Error bars represent SEM across subjects. Statistical tests were post-hoc t-tests conducted at each depth level between values of retinal and objective motion, correction refers to the number of depth levels. See full text for 2-way ANOVA analyses. \odot : $p < 0.05$ corrected, \blacktriangle : $p < 0.05$ uncorrected, and \blacklozenge : $p < 0.28$.

3.4. Discussion

In this study, we used ultra-high field (9.4T) fMRI to measure laminar BOLD signal in high-level visual areas V3A, V6 and V7 in response to retinal motion, objective motion, and pursuit eye-movement. We hypothesized that feedback signals related to efference copies from eye movements would influence superficial or deep layers during processing of objective motion but not retinal motion. In order to test this, we used a factorial design including planar screen motion and smooth pursuit eye movements that has previously been shown to allow functional segregation of retinal and objective motion responses (Fischer et al. 2012a). Our results firstly demonstrate that laminar signal can be recorded in high-level motion regions such as V3A, V6, and V7. Second, we confirmed that V3A and V6 had an overall preference for objective compared to retinal motion. Third, we found that in all regions, there was an interaction between layer and experimental condition, and that the signal increase towards superficial layers was higher for objective motion compared to retinal motion. In V3A, this was the case even though signal strength in lower layers was matched between retinal and objective motion, and in V7 retinal motion trended higher in lower layers.

There are two possible accounts for these findings. First, the measured response profiles are compatible with segregated neural responses across depth, e.g. a higher fraction of voxels with a preference towards objective motion in superficial layers. This population of voxels could be driven by feedback signals related to pursuit and/or by local processing integrating pursuit signal with retinal signal entering at middle layers. In context of this study we speculate that these feedback projections transmit efference copies of the eye movement from other cortical areas, most likely originating from pursuit regions of frontal eye fields (Stanton et al. 2005a) and MST (Boussaoud, Ungerleider, and Desimone 1990), to superficial layers in V3A and V6.

Second, as the laminar responses did not show a double-dissociation between experimental conditions across depth but instead an increase of objective motion response towards upper layers only, an alternative account cannot be excluded. Pial vessels and diving venules are known to induce a spatial bias of increased BOLD signal toward superficial layers (Ahveninen et al. 2016; Polimeni et al. 2018). If this bias increases as a function of net signal, the higher signal observed in superficial layers of V3A and V6 in response to objective motion could be driven by objective motion signal arising from all layers yet accumulating towards upper layers. Two observations speaking against the second account are the lack of such differences in lower layers in V3A, and the higher objective motion slope for objective motion in control area V7 despite retinal signal trending higher in lower layers.

Finally, we observed unique, condition-specific laminar profiles after removal of linear trends across cortical depth, which may open a window to new mechanistic insights into motion processing in high-level cortical regions. We discuss these results in the following section.

Normalized Laminar Profiles

All detrended laminar profiles showed a higher response in middle layers surrounded by lower responses in deep and superficial layers. The only exception was the laminar profile in V6 to retinal motion that showed a prominent dip in the middle layers. The present results open up several interesting mechanistic interpretations that will need to be investigated in future studies.

First, we know that objective motion responses are the product of an integration between pursuit signals with retinal motion, and that in 3T fMRI, V6 was suppressed by retinal motion alone (Fischer et al. 2012a). The signal integration could hence be implemented in the form of an inhibition-excitation mechanism, that allows the two signals to be subtracted from each other. If the retinal input signal to V6 is of an inhibitory nature in this mechanism, it could account for the decrease in the middle layers for retinal motion. The observed laminar dip in the middle layers specific to retinal motion could therefore be related to the inhibitory contribution of retinal motion, as well as to the suppression of retinal motion signal observed previously.

Second, V6, in contrast to V3A, can compensate for pursuit signals even when 3D expansion flow is superimposed on the planar motion stimulus (Fischer et al. 2012a). This suggests that in addition to the direct comparison between the retinal motion signal with pursuit velocity

signals, V6 must also contain a mechanism allowing it to parse the planar component embedded in the complex motion, followed by its comparison with the efference speed signal. The V6-specific dip may be related to this V6-specific parsing mechanism.

Third, taking into account the direct connection between V3A and V6 (Galletti et al. 2001), V6 can be assumed to receive much of its high-level motion input (i.e. objective motion) from V3A and from higher-level motion responsive regions such as MST (Galletti and Fattori 2003, 2018; Fischer et al. 2012b). This view is also compatible with the large receptive fields in V6 and its preference for complex ego-motion compatible motion (Cardin and Smith 2011, 2010; Pitzalis et al. 2006, 2010, 2012, 2015), and its potential role in complex vision-for-action tasks (Galletti et al. 2003, 2018; Pitzalis et al. 2013, 2015). Hence, in contrast to V3A, V6 may also receive retinal motion through feedback, e.g. from other higher-level regions such as MST—hence the relative weighting of the retinal motion profile in deep and superficial layers known for receiving feedback signals (Felleman and Van Essen 1991; Wong-Riley 1978).

The decrease in the laminar profile of retinal motion in middle layers in addition to being significantly different from the laminar profile of objective motion at layer 7, 8, and 10, therefore, provides first insights with regards to mechanistic differences between retinal and objective motion processing within V6 in the context of motion perception. While future studies are needed to differentiate between the different interpretations, to our knowledge, this has been the first study demonstrating condition-specific laminar profile differences in high-level visual areas, providing a new entry to a better mechanistic understanding of motion processing mechanisms in V3A and V6.

Cortical Depth Sampling

In the present study we computed the relative contribution of each cortical layer, reconstructed based on normalized distances between the white matter and pial surface boundary (Dale, Fischl, and Sereno 1999; Fischl, Sereno, and Dale 1999, 2000, 2001, 2002; Polimeni et al. 2010a; Segonne et al. 2004), to the functional signal of each voxel. One limitation of the present depth sampling method is that because the relative thickness of the cortical laminae changes across the cortex and correlates with the local folding pattern (Fatterpekar et al. 2003; Van Essen and Maunsell 1980), the laminar reconstructions based on the above method do not precisely correspond to the histological laminar anatomy per se. Although such surface reconstructions are not expected to have a perfect alignment with

cortical lamina, many high-field laminar studies (De Martino, Moerel, Xu, et al. 2015; Koopmans, Barth, and Norris 2010, 2011; Olman et al. 2012; Polimeni et al. 2010a; Zimmermann et al. 2011) have demonstrated the robustness of this model in accurate assignment of fMRI signal to cortical layers specifically with high resolution functional data. Another consideration, as discussed previously (Polimeni et al. 2010a), is the dependency of the spatial specificity of the BOLD signal on the local vascular density, which also depends on the position within the folding pattern as well as the depth within the cortical gray matter. Therefore, more studies are needed to further examine causes of variability in the spatial specificity of the BOLD signal.

Feedforward and Feedback Signals

In the sensory system, bottom-up feedforward signals convey sensory inputs from the external world into the brain, whereas top-down feedback signals are thought to project higher-level information such as expectations or non-visual information to visual regions. Feedforward and feedback signals are largely segregated and terminate in distinct layers of cortex (Petro and Muckli 2017). Feedforward signals arrive in mid-layers, whereas feedback signals target deep and superficial layers (Felleman and Van Essen 1991; Wong-Riley 1978). V3A and V6 were localized based on their higher preference to objective compared to retinal motion (objective - retinal contrast). This preselection introduces an unavoidable correlation between the upper-layer bias in laminar profile of objective motion and its overall higher signal, i.e. signals with higher amplitude tend to increase toward the superficial layers with sharper slope. To examine whether we could find an upper-layer bias also in regions without a net signal preference to objective motion we included V7 as a control ROI.

Similar to V3A and MST, V7/IPS-0 receives efference copies of eye movements, with a corresponding response bias (Konen and Kastner 2008; Schluppeck, Glimcher, and Heeger 2005). This may explain the significantly higher response of V7 to pursuit. The steeper activity increases toward superficial layers during objective compared to retinal motion processing despite the higher activity trend of retinal motion in deep layers is consistent with the arrival of pursuit related feedback signals in the superficial layers.

Laminar Organization

Invasive laminar recordings in macaque during figure-ground segregation reported feedback effects in superficial layer I and the upper part of layer II, whereas in the absence of input to middle layer IV, these effects are restricted to the deep layers. One possible mechanism to explain how interaction with bottom-up sensory inputs can change laminar profile of feedback signals is through inhibitory connections from the deep layers to the granular layer IV (Katzel et al. 2011; Kim et al. 2014; Thomson and Bannister 2003), which leads to a reduction throughout the entire cortical column as a result of the excitatory pathway from layer IV to layers II–III and from layers II–III to layers V–VI (Douglas and Martin 2004). It should, however, be noted that local excitatory-inhibitory circuitries may have distinct characteristics across different cortical regions and also across different species. Therefore, the mechanism of integration described here may not be fully translatable to V3A and V6 areas in human.

It has previously been shown that remapping of the eye movement motor commands in V3A precedes occurrence of the eye movement (Nakamura and Colby 2002) suggesting that this area has access to the information about the eye movement before efference copy of the eye movement reaches them. This could suggest that the observed laminar profile of V3A may be driven, at least in part, by local computations in this region. According to the principles of predictive coding (Brown and Brune 2012; Mumford 1992; Rao and Ballard 1999) as one proposed implementation of hierarchical perceptual inference, each cortical region contains segregated neuronal populations coding for perceptual hypotheses (predictions) and mismatch between these hypotheses and the current bottom-up sensory inputs (prediction error). These segregated sub-populations have been suggested to be located in different cortical layers, with deep layers being predominantly populated by prediction units, and the units for prediction errors being more likely to reside in middle and superficial layers (Bastos et al. 2012). This mechanism can be one potential explanation of the suppressed response to retinal motion in V3A and V6 when it is induced by pursuit eye movement.

The fact that such neuronal computations are likely simultaneously at work with other mechanisms involving intra-laminar connectivity within each cortical area can significantly complicate the interpretation of laminar activations. This becomes even more complex when the BOLD effects are detected in superficial layers, which are proximate to pial veins, very thin, and sparsely populated with neurons. Contextual BOLD effects in superficial layers can

also arise from layers II and III, known to be targeted by horizontal connections (Angelucci and Bullier 2003; Rockland and Pandya 1979; Self et al. 2013).

Limitations of Laminar fMRI

In laminar fMRI studies, spatial resolution of functional voxels, especially in areas where cortical gray matter is quite thin, plays an important role in accurate mapping of functional activity. Obtaining a high functional resolution becomes even more challenging taking into account the blurring effect of head motion correction, magnetic field inhomogeneities, and inaccuracies in the registration between functional and anatomical data.

Venous blood draining from deep layers toward superficial layers pools deoxygenated blood towards the surface and displaces the measured signal change from the site of neuronal activity (Duvernoy, Delon, and Vannson 1981). Therefore, the closer to the cortical surface the more laminar activation is expected to contain a mixture of signals from lower layers. These laminar interdependencies reduce spatial specificity of the signal and make it difficult to precisely ascertain the origin of laminar activation, especially in the superficial layers. Exclusion of the voxels located above the cortical ribbon (Polimeni et al. 2010a) and comparing laminar profiles of different effects rather than a particular effect per se (Kok et al. 2016) have been suggested to reduce such effects.

Intrinsic complexity in the relationship between synaptic activity and hemodynamic response is another challenge in interpretation of fMRI activation and more so in laminar fMRI, in particular as neurovascular coupling can differ for negative and positive BOLD responses as well as across layers (Goense, Merkle, and Logothetis 2012). However, studies in macaques have shown that neuronal excitation (Goense and Logothetis 2008) and inhibition (Shmuel et al. 2006) typically closely correspond to the BOLD signal, even though exceptions do exist (Bartels, Logothetis, and Moutoussis 2008; Logothetis 2008).

Similar to previous laminar studies in humans, our study demonstrates the ability of high field fMRI to capture neuronal activation at the level of fine scaled cortical structures i.e. cortical layers. Investigation of the information content of laminar signals (Kamitani and Tong 2005; Williams et al. 2008) rather than their amplitude can be pursued in future studies to investigate other aspects of laminar signals.

CHAPTER 4. Real World Motion Processing in MT, pMST, and V1. A Laminar fMRI Study at 9.4T

4.1. Introduction

Much of the motion signal falling into our eyes is driven by our own movement. In order to correctly perceive and differentiate a stable world from external motion in our environment, the visual system is thought to integrate visual motion signals on our retina with non-visual cues such as efference copies of eye-movements (von Holst and Mittelstaedt 1950b; Gibson 1954; Ilg and Churan 2004; Royden, Banks, and Crowell 1992). This integration yields responses found in so-called 'real-motion' neurons: they respond to world-centered motion even if it is cancelled on the retina through pursuit eye movements, and they do not respond to retinal motion when induced by eye movements sweeping over a stationary edge (Erickson and Thier 1991; Galletti, Battaglini, and Fattori 1990; Galletti and Fattori 2003). Several brain regions, including V1 and V2 (Galletti, Battaglini, and Aicardi 1988; Daddaoua, Dicke, and Thier 2014), as well as key motion regions V5/MT and MST (Erickson and Thier 1991; Thier and Ilg 2005), V3A (Galletti, Battaglini, and Fattori 1990), V6 (Galletti and Fattori 2003), and ventral intraparietal area (VIP) contain varying fractions of real motion neurons.

Human fMRI studies on real motion responses (Goossens et al. 2006; Arnoldussen, Goossens, and van den Berg 2011; Fischer et al. 2012a, 2012b; Nau, Schindler, and Bartels 2018) revealed overwhelming responses to real motion compared to retinal motion in areas V3A and V6 (Fischer et al. 2012a; Nau, Schindler, and Bartels 2018), but also robust responses in early visual regions V1-V3 (Nau, Schindler, and Bartels 2018). Mid-level motion regions V5/MT, MST, and further occipito-parietal regions including CSv had intermediate (Goossens et al. 2006; Arnoldussen, Goossens, and van den Berg 2011) and about equally strong response fractions to retinal and objective motion (Fischer et al. 2012a; Nau, Schindler, and Bartels 2018). One study suggested that distinct sets of voxels responded to head-centered and retinal motion in V5+/MT+ (Arnoldussen, Goossens, and van den Berg 2011). These past results suggest that both, early visual areas as well as the human motion complex V5+/MT+ contain neural responses to visual motion in at least two separate reference frames, i.e. retinal and head- or world-centered. However, it is not known how and whether these representations are functionally segregated, and whether such a segregation involves columnar structures or organization across cortical depth.

In the present study we therefore used ultra-high-field human fMRI at 9.4T to examine whether functional signal corresponding to retinal motion, objective motion, and pursuit can be differentiated across cortical depths or across voxels independent of depth. We used a slab of slices that allowed us to cover in a same acquisition early visual cortex as well as the human motion complex V5+/MT+, with a functional resolution of 0.8 mm isotropic.

In both, early visual cortex and V5+/MT+ complex retinal signals arrive through bottom-up connections from lateral geniculate nucleus (LGN), superior colliculus (SC) (or V1 for V5+/MT+) in mid-layer IV (Bremmer et al. 2001; Lyon, Nassi, and Callaway 2010). The origin of information from eye-movements or already integrated objective motion likely involves top-down projections from regions such as V3A, V6, parietal cortex, and, for V5+/MT+, the smooth pursuit region of the frontal eye fields (Stanton et al. 2005b). Even though such top-down connections that target primarily upper or lower cortical layers (Larkum 2013b), this does not preclude a columnar-style functional segregation, akin to the segregation of colour, motion, depth, or orientations and directions within V1, V2, or the V5+/MT+ complex, and as suggested previously (Arnoldussen, Goossens, and van den Berg 2011).

We hence used a functional protocol that has in the past allowed for a reliable segregation of neural responses to retinal and objective motion using a two-by-two factorial design involving visual pursuit and planar motion (Fischer et al. 2012a). We recently used the same paradigm but different anatomical coverage to examine parietal regions V3A and V6 using 9.4 T imaging, and found differential laminar signals to retinal and objective motion particularly in V6 (see Chapter 3). The present study aimed to examine V1 and V5+/MT+ using the same approach in order to examine their functional organization with respect to real motion processing while using highly comparable methodology.

4.2. Methods

The present study asked a very related functional question to one of our previous studies (see Chapter 3), yet on distinct anatomical visual regions (V1 and V5+/MT+) instead of V3A and V6. For this reason, visual stimuli, experimental paradigm, task, and some but not all analysis steps were identical to those used in our recent study. For the sake of clarity, the corresponding sections below are reproduced based on the prior descriptions (see Chapter 3).

4.2.1. Participants

Six neurologically healthy adults (4 females, age 27 ± 5 , mean \pm SD) with normal or corrected-to-normal vision volunteered to participate in the study. In accordance with local research ethics committee requirements, volunteers underwent a physical and psychological check-up by a local physician and provided written informed consent. The study was conducted in agreement with the Declaration of Helsinki (World Medical Association, 2013). Prior to scanning, subjects were instructed on the experimental procedures and performed a test trial to get accustomed to stimuli and to the task.

4.2.2. Visual Stimulation and Experimental Design

Visual stimuli and the experimental paradigm were identical to those used in our recent study of parietal areas V3A and V6, and described here again for the sake of clarity (see Chapter 3). Visual stimuli consisted of randomly arranged black and white dots (size ranging from 0.1 to 1.1 deg) on a grey (90 cd/m^2) background, presented at 100% contrast (i.e. maximal luminance for white dots and minimal luminance for black dots). The 320 visible dots yielded an average density of 0.75 dots/deg^2 . The experiment included 4 conditions arranged in a 2x2 factorial design including 2 factors with 2 levels each. The two factors were “pursuit” (on/off) and “objective motion” (on/off). Objective motion was achieved by displacement of the entire dot field along the vertical and horizontal axes along a 2D (i.e. planar) sinusoidal trajectory with either 3 or 4 cycles per trial (randomly assigned to x and y axes, respectively) and with random initial phases. This led to figure-of-eight-style planar trajectories of the dot field. We refer to this as objective motion (equivalent to ‘real’ motion) to distinguish it from retinal motion that can be induced by eye movements over the static dot field. Pursuit was implemented by moving the otherwise centrally presented fixation disc (that contained the fixation task, see Fixation Task below) along the same trajectory. The maximal eccentricity of the fixation disc reached 2.5 visual degrees, such that the eccentricity of the visually fully controlled stimulus (i.e. fixation to screen border) was at least 12.5×7.5 visual degrees or more at all times (given the screen size of 30×20 visual degrees). When both pursuit and objective motion were ‘on’, the two were coupled, such that the fixation task moved together with the dots, resulting in zero retinal motion. The starting direction was randomized for each trial. The mean speed for objective motion (and pursuit) was 3.80 deg/s .

Two key contrasts available from this 2x2 design, namely the contrast “objective motion” (i.e. both conditions with objective motion “on” versus both conditions with objective motion “off”), and “retinal motion” (i.e. the two conditions where pursuit and objective motion were in different states (on/off and off/on) versus the two conditions where both factors were in the same state (on/on and off/off)) were fully controlled for the amount of retinal motion and pursuit signals. As each of these contrasts had one pursuit condition counting positive and one counting negative, any peripheral motion artifacts resulting from pursuit cancelled each other out within each contrast. Hence, foveal and parafoveal representations (out to 12.5 x 7.5 visual degrees eccentricity) would be stimulated in a fully controlled way, and peripheral effects would be balanced and cancel out. Only the contrast “pursuit” (both pursuit “on” conditions versus both pursuit “off” conditions) was difficult to interpret as it combined motor effects of pursuit with visual effects (peripheral motion), which is why we focus here on the first two, controlled, contrasts, as we did in our original study (Fischer et al. 2012a).

4.2.3. Procedure

Stimulus presentation followed a block design schedule where each of the four stimulus conditions was presented eight times with a duration of 12 s each. Hence, each of the four functional runs consisted of 32 full stimulus blocks. Different conditions were presented in pseudorandom sequences in which each condition was preceded equally often by all conditions. The stimulus was rear-projected using a linearized projector with a resolution of 1024 x 768 pixels at 60 Hz onto a screen located in the scanner bore. Subjects viewed the stimulus at 82 cm distance through a mirror mounted on the receive coil array, leading to a display size of 30 x 20 visual degrees. The stimulus was written in MATLAB 2010a (<http://www.mathworks.de/>) using the Psychophysics Toolbox 3 extensions (<http://psychtoolbox.org/>) and was presented using a Windows computer.

4.2.4. Fixation Task

Throughout the experiment subjects performed a character repetition-detection task on the fixation disc, ensuring fixation as well as balanced attention across conditions (Huk, Ress, and Heeger 2001). A total of 26 characters were presented in random succession (1.6 degrees

height, white) on a gray fixation annulus (2 degrees width, 72 cd/m²), with random presentation times of 1-2.16 s. Subjects indicated character repetitions by button press.

4.2.5. Data Acquisition and Image Reconstruction

All measurements were conducted on a 9.4 Tesla whole-body MRI scanner (Siemens, Erlangen, Germany) using a custom-built head coil with a 16-element dual row transmit array and a 31-element receive array (Shajan et al. 2014).

Whole-brain T1-weighted anatomical images were acquired for each subject using a MP2RAGE sequence (Marques et al. 2010; Hagberg et al. 2017) (TR = 6000 ms, TE = 3 ms, voxel size 0.6 x 0.6 x 0.6 mm, matrix = 352 x 352 x 256), yielding two inversion contrasts (flip angle 1 = 5°, flip angle 2 = 9°, TI1 = 800 ms, TI2 = 2000 ms, acceleration R=2x2, CAIPI-shift 1). MP2RAGE data was reconstructed offline (Scheffler and Ehes 2016) using custom software developed in MATLAB (The Mathworks, Natick, MA).

For the acquisition of blood oxygen level dependent (BOLD) weighted images, we used a GE-EPI sequence with FLEET (fast low-angle excitation echo-planar technique) autocalibration, that has been shown to exhibit the highest temporal stability and the lowest residual aliasing across acceleration factors, field strengths, and spatial resolution (Polimeni et al. 2016). The parameters were as follows: voxel size: 0.8 x 0.8 x 0.8 mm, TR / TE / flip angle = 2000 ms / 23 ms / 70 deg, field of view = 150 mm, bandwidth = 1156 Hz / pixel, GRAPPA (Griswold et al. 2002) acceleration factor of 5, and partial Fourier of 7 / 8. The wall-time for each run was 6 min and 36 seconds (396 s), excluding the initial 8 s block of dummy scans in the beginning of each scan to allow T1 steady state to be achieved, and 1 TR of reference scan. Forty oblique-axial slices were positioned parallel to the calcarine sulcus. Functional images were reconstructed with the standard online Siemens EPI and GRAPPA reconstruction. Five functional runs each consisting of 203 volumes, including the four dummy scans and one reference scan, were obtained for each subject.

4.2.6. Pre-processing and Statistical Analysis of Functional Volumes

Pre-processing

Functional data was preprocessed and analyzed using FreeSurfer functional analysis stream (FSFAST, <https://surfer.nmr.mgh.harvard.edu/fswiki/FsFast>). Preprocessing included motion correction of the functional volumes to the first volume of the first run and co-registering

functional images to the MP2RAGE. No spatial smoothing (volume- or surface-based) was applied to the data at any stage of the analysis. Topup (Andersson, Skare, and Ashburner 2003) as implemented in FSL (M. Smith et al. 2004) was used for distortion correction of the EPI images using additional 10 volumes collected with reversed phase-encode blips at the end of the experiment.

GLM Analysis

A general linear model (GLM) including regressors for each condition as well as head-motion parameters was fitted to the time course of each voxel. A second order polynomial function was used as a nuisance regressor to model low frequency drifts. The GLM analysis of the 2x2 factorial design allowed us to separate cortical responses related to the main factors of (a) pursuit (both pursuit conditions versus both fixation conditions), (b) objective motion (both conditions with background-dot motion versus both conditions with static background), and their interaction (c) retinal motion (the two conditions where pursuit and objective motion were in different states (on/off and off/on) versus the two conditions where both factors were in the same state (on/on and off/off)). The two contrasts objective motion and retinal motion were each balanced for effects of pursuit, as in each of the two contrasts one pursuit condition is on the positive and one on the negative side of the contrast. Hence, these two conditions are entirely driven by effects related to processing of objective motion or that of retinal motion, excluding any pursuit-related effects such as peripheral motion or less accurate fixation during pursuit.

4.2.7. Definition of Region of Interest (ROI)

FreeSurfer surface-based analysis (Fischl, Sereno, and Dale 1999; Dale, Fischl, and Sereno 1999) was used to define the ROIs on the surface (Figure 10). For ROI definition only, fMRI data was smoothed (3 mm) on the surface to allow for more accurate identification of functionally defined ROIs. No smoothing, neither in the volume nor on the surface, was performed in any stage of the subsequent laminar analyses. For each subject, the joint-ROI of V5+/MT+ (that includes MST) was functionally localized as voxels responsive to the three conditions containing objective motion and/or pursuit versus the all-static condition (no pursuit and no motion). We then used probabilistic FreeSurfer maps of MT and MST to guide the division of the joint-ROI into putative V5/MT and putative MST. pV5/MT was located on

the ventrolateral occipital cortex, slightly posterior to the junction of the ascending limb of the inferior temporal sulcus (ALITS) and the lateral occipital sulcus (LO) coinciding with the anatomical landmarks previously reported for V5/MT area, whereas pMST was typically located on the ventral and dorsal banks of the posterior limb of the inferior temporal sulcus (ITS) (Zeki et al. 1991; Tootell and Taylor 1995; Dumoulin et al. 2000). In order to maintain independence between localizer runs and runs used for further analyses, the first functional run was used for ROI localization, and the remaining four runs were used for analysis. V1 was localized using FreeSurfer probabilistic maps.

4.2.8. Depth-Dependent Analysis

To test for differential signal intensities across cortical depths, we used FreeSurfer (Dale, Fischl, and Sereno 1999) to generate surface reconstructions of the interface between white matter and gray matter (white surface) and between gray matter and CSF (pial surface) from MP2RAGE data at native 0.6 mm isotropic resolution (Zaretskaya et al. 2018). Depth-dependent sampling of voxel-wise GLM results was performed by generating nine additional surfaces within the gray matter at fixed relative distances from white matter and pial surface (Polimeni et al. 2010a). To align functional volumes to the surface reconstructions generated from MP2RAGE anatomical data, a boundary-based registration method (Greve and Fischl 2009) was used to first identify the WM-GM boundary in the EPI data and then register this interface to the corresponding surface reconstruction in the anatomical image using a rigid transformation. This transformation was used to transfer the time series statistics of each voxel to the collection of surface reconstructions intersecting that voxel. Mapping of functional signal values in each voxel to the corresponding surface was done using nearest neighbor interpolation.

For each ROI, contrast estimates belonging to the same depth were averaged and their differential response to different conditions across layers was examined in a 2-way ANOVA with factors “depth” (1 to 11) and condition (retinal, objective and pursuit).

4.2.9. Correlation Analysis

The above analysis tested for differential depth profiles of functional responses to the different motion types. However, other types of functional segregation within an area are also possible. For example, neurons selective to the same motion type can be clustered into

cortical columns. Alternatively, there may be a spatial gradient along the 2D cortical sheet from predominantly one motion type to another. In order to be able to detect these other possibilities, we conducted a correlation analysis that does not assume a specific spatial layout of functionally segregated signals. It simply tested whether functional preference to one motion type was correlated to that of another. First, we defined preference of each voxel within a ROI to each specific motion type in terms of GLM contrast values for retinal, objective, and pursuit signals. Second, we measured the similarity between responses to different motion types by computing Pearson's correlation coefficients between all pairs of contrasts across voxels. A high correlation between two motion types (negative or positive) is indicative of a common driving force, whereas a low correlation implies different underlying processes.

4.3. Results

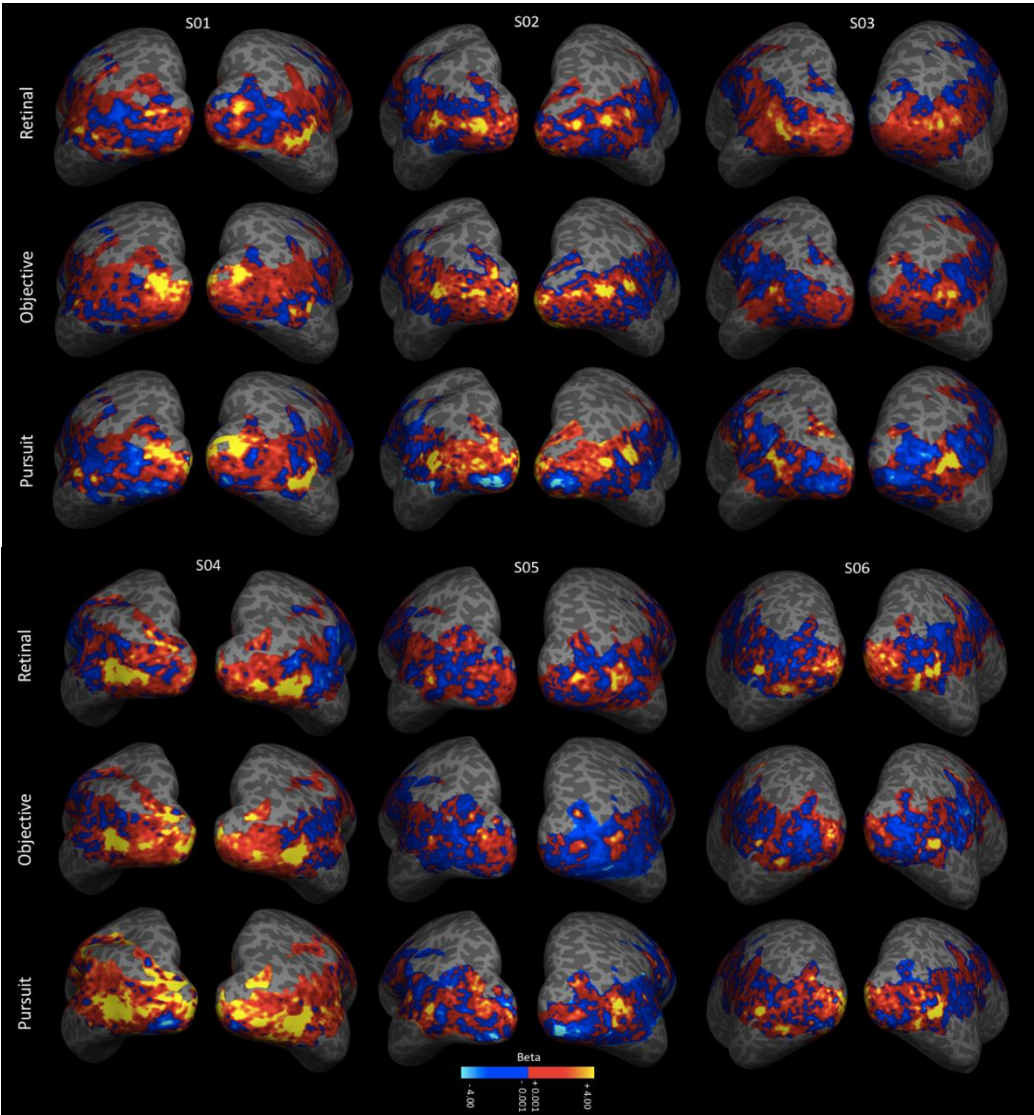


Figure 10. Retinal, objective, and pursuit contrast values projected onto the individual cortical surfaces reconstructed from MP2RAGE anatomical image. In all subjects, V5+/MT+ response to each motion type is detectable as distinct localized activations.

4.3.1. Depth-dependent Response to Retinal, Objective, and Pursuit Motion

We first examined the net signal of V1, pV5/MT, and pMST in response to retinal and objective ('real') motion using ultra-high field (9.4T) fMRI. In V1 and MT, net BOLD signal during retinal motion was higher compared to objective motion (V1: $T(11)=2.8215$, $P=0.0166$; MT: $T(11)=2.6857$, $P=0.0212$; pMST: $T(11)=1.3158$, $P=0.2150$;) (Figure 11). A small preference to retinal motion in MT but not in MST is consistent with previously reported responses to retinal and objective motion in MT, and MST (Fischer et al., 2012).

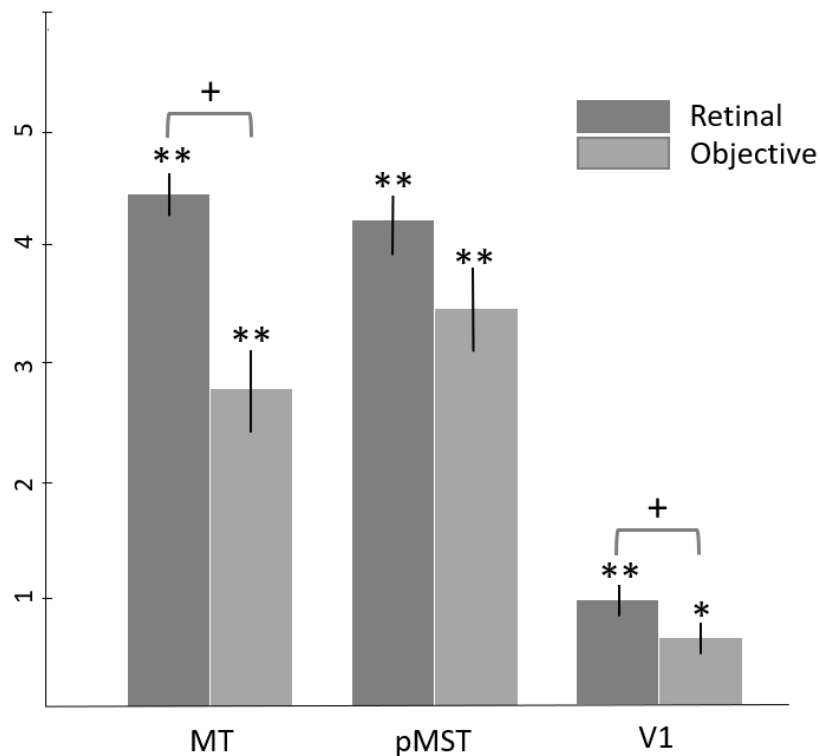


Figure 11. MT, pMST, and V1 overall response to retinal, object, and pursuit motion. Despite having a significant response to objective ('real') motion, in all three regions retinal motion was preferred to objective motion. V1 and pMST had the highest response to pursuit motion (** $p < 0.001$, * $p < 0.01$, + $p < 0.05$).

We then examined the laminar profiles in response to the three motion types. In all three regions, there was a significant interaction between cortical depth and experimental contrast (2-way ANOVA, V1: $F(10,110)=16.45$, $p < 0.001$; MT: $F(10,110)=2.41$, $p < 0.001$; pMST:

$F(10,110)=7.76$, $p<0.001$). Post-hoc paired sample t-test revealed a significantly stronger response to retinal compared to objective motion in MT across all depths except in depth seven ($p<0.05$) (Figure 12.A). However, in V1 and pMST no significant preference to either retinal or objective motion was found at any depth (Figure 12.B, C) confirming that the significant interaction between depth and contrast in these regions only holds true when pursuit is compared with either of the other two contrasts.

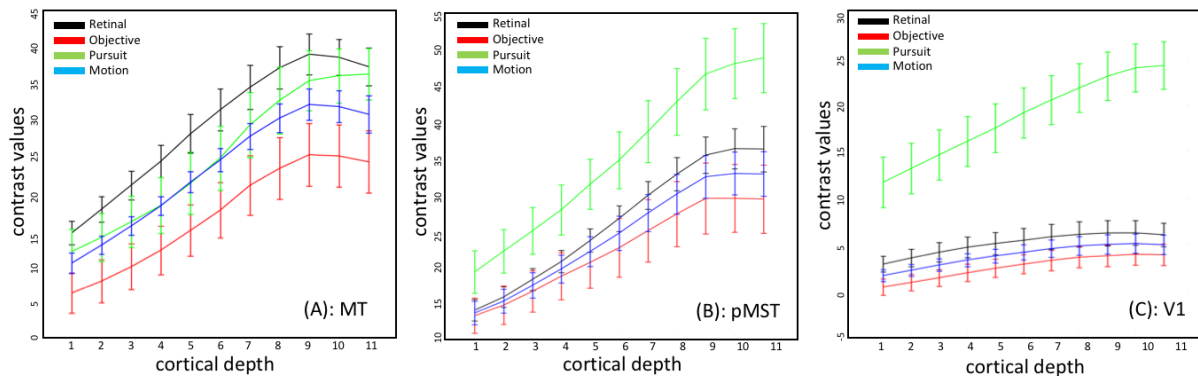


Figure 12. Laminar profiles of MT, pMST, and V1 in response to each motion type. The overall preference of each region to each specific motion type is clearly reflected in their depth-dependent response. Note that “motion” is the average between objective and retinal motion.

In case of V1, with significantly high response to both motion types (retinal: $T(11)=5.4575$, $P<0.001$, objective: $T(11)=4.3765$, $P=0.0011$), there is almost no increase toward the surface, nor did we observe a higher slope in laminar profile of retinal motion compared to objective although it is significantly preferred over objective ($T(11)=2.8215$, $P=0.0166$). Future studies are needed to determine the extent, to which the enhancement of BOLD signal in V1 and MT towards the cortical surface is caused by higher metabolic demands in upper and superficial depths or by large draining veins on the cortical surface. Also, it will be of interest to determine which factors contribute to slopes that depend on absolute signal amplitude and those that scale with signal amplitude – our data appear to show examples for both. In both regions, however, we observed retinal and objective signals to increase with almost equal slopes toward the cortical surface.

4.3.2. Correlation

To investigate if processing of objective motion involved distinct populations of voxels driven by independent functional processes, we examined the relation between retinal, objective, and pursuit motion signals using Pearson correlation coefficients between pairs of contrasts, separately for each ROI within individual hemispheres (Nasr, Polimeni, and Tootell 2016). A strong (positive or negative) correlation between two motion signals would indicate a common driving force or the same population of voxels responding to both motion types, whereas uncorrelated signals would imply independent processes or segregated voxels responding to each motion type.

We found that in MT and pMST, retinal, objective, and pursuit motion signals were highly correlated (Figure 13.1). Similarly, in V1 we observed a high correlation between retinal and objective motion signals ($T(11)=5.0209$, $P=0.0040$) but almost no correlation between retinal and pursuit, nor between objective and pursuit signals was found (retinal-pursuit: $T(11)=2.8622$, $P=0.0353$; objective-pursuit: $T(11)=3.4992$, $P=0.0173$) (Figure 13.1).

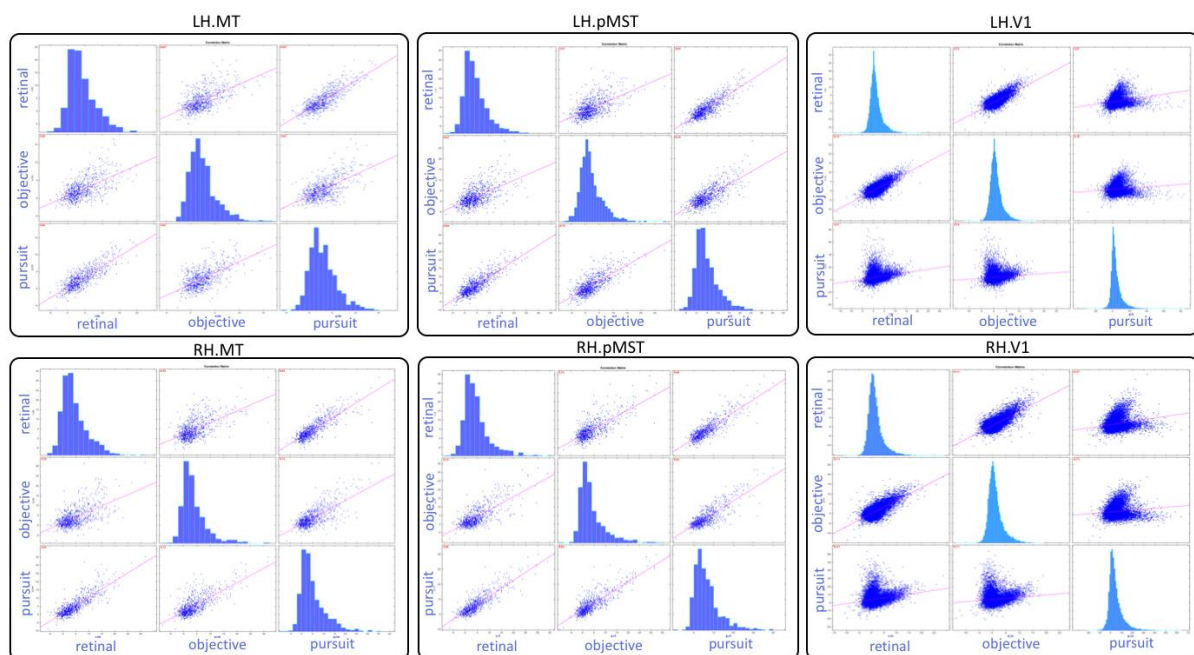


Figure 13.1. correlation plots for all pairs of motion signals; retinal, objective, and pursuit in MT, pMST, and V1 for one representative subject. In MT and pMST, a significantly positive correlation was observed between all motion types. In V1, retinal and objective were also positively correlated, whereas, no significant correlation was observed between retinal and pursuit, neither between objective and pursuit. However, the plots for V1 were indicative of

the presence of two separate population of voxels responding differently to positive and negative retinal and objective motion.

From the scatter plots in V1 the presence of two populations of voxels is discernible: one with negative response to retinal (and/or objective) motion that seems to be negatively correlated with pursuit signal, and the other with positive response to retinal (and/or objective) that seems to have a positive correlation with pursuit signal. To investigate this further, we split the data into separate sets, one set with positive retinal motion responses and the other with negative retinal motion responses. We then calculated correlations between negative and positive retinal motion signals separately with pursuit signal and repeated the same for objective motion. Our results revealed a significant negative correlation (negative retinal-pursuit: $T(11)=-9.2373$, $P<0.001$) between retinal motion and pursuit in voxels with negative response to retinal motion, and a positive correlation (positive retinal-pursuit: $T(11)=8.5889$, $P<0.001$) in voxels with a positive response to retinal motion (Figure 13.2). The same was observed between objective motion and pursuit motion signals: voxels with a positive response to objective motion were positively correlated with pursuit (positive objective-pursuit: $T(11)=11.5376$, $P<0.0001$), whereas voxels that responded negatively to objective motion demonstrated a negative correlation (negative objective-pursuit: $T(11)=-8.1258$, $P<0.001$) with pursuit (Figure 13.2).

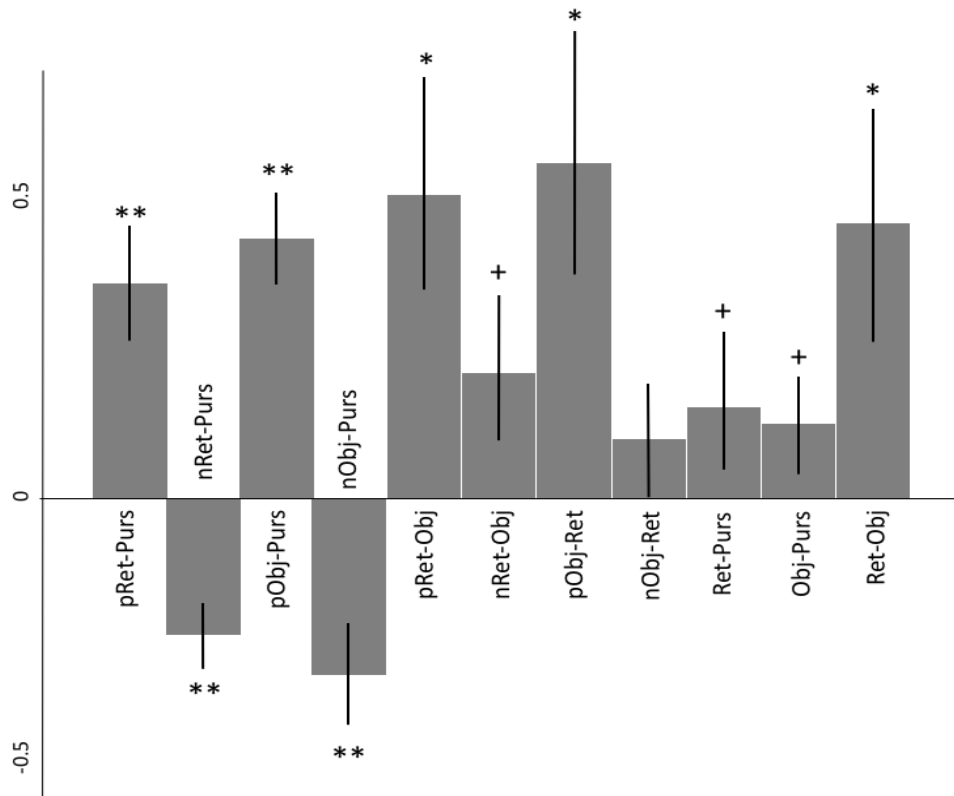


Figure 13.2. Bar plots of correlation values averaged across all subjects. Error bars represent SEM (** $p < 0.001$, * $p < 0.005$, + $p < 0.05$). : “n” denotes negative, “p” denotes positive valued responses to the respective contrast.

4.4. Discussion

Using ultra-high field fMRI at 9.4T, we examined processing of real-world motion in human areas MT, pMST, and primary visual cortex in either the presence or absence of the pursuit eye movements. We first investigated to what extent these regions integrate retinal motion with extra-retinal pursuit signals to discard self-induced retinal motion and respond to objective (‘real’) motion. For MT and pMST we were able to replicate previously shown (Fischer et al. 2012a) results, in that both regions responded about equally to retinal and objective motion, with MT having a marginally significant larger response to retinal motion. In V1, we observed a higher response to retinal motion compared to objective motion. To investigate if the integration between visual retinal motion signal with non-visual pursuit signal in MT, pMST, and V1 involves any laminar organization we used high resolution (0.8mm isotropic) fMRI to study how these signals change across cortical depth. We found that in MT and pMST depth-dependent responses to retinal and objective motion increased toward cortical surface, whereas in V1 they remained almost constant across depth. The response to

pursuit motion increased toward superficial depths in all three regions. Overall, the depth profiles of retinal, objective, and pursuit signals (Figure 12) in none of the regions provided cues for a functional segregation as a function of depth.

In order to examine whether a non-laminar spatial segregation of function is present, we calculated the correlations of voxel responses between pairs of contrasts in each ROI to examine the relationship between retinal, objective, and pursuit motion signals across the whole population of voxels in a given ROI. In MT and pMST we found a positive correlation between all pairs of contrasts. V1 differed however: retinal and objective were also positively correlated, but almost no correlation was observed between retinal motion and pursuit, neither between objective and pursuit motion. This implies that in MT and pMST common functional processes are likely to be involved in mediating the response to retinal, objective, and pursuit motion, whereas in V1 independent functional processes seem to be driving the response to retinal and pursuit motion. The same holds true for objective and pursuit motion in V1. Based on our laminar results, it is unlikely that these segregated functions reside in different cortical layers in V1. On the other hand, the invariability of retinal and objective signals across cortical depth may be indicative of columnar functional units driving the response to these motion types. Additionally, we found that in voxels with negative response to retinal motion, retinal and pursuit were negatively correlated. The same was true for objective motion and pursuit: in voxels with negative response to objective motion, objective and pursuit were negatively correlated.

Visual Motion Processing

While V5/MT and MST are both heavily involved in motion processing, they can be differentiated based on their distinct functions in visual motion and pursuit processing. V5/MT is allocated to the processing of visual motion signals such as motion velocity and acceleration, it is also implied in the processing of object motion. On the other hand, MST (or better MSTd), together with its key role in smooth pursuit processing is additionally involved in processing extra-retinal signals and self-motion cues. Ventrolateral MST (MSTl) has been shown to contain the representation of object motion (Ilg and Churan 2004; Ilg and Thier 2008) possibly facilitated by visual tracking neurons in this area, which are sensitive to slow hand- and eye-movements as well as retinal image slip (Erickson and Thier 1991; Ilg and Thier 2008).

Having cells with larger receptive fields, MST responds stronger to coherent motion and optic flow patterns compared to V5/MT. Its sub-region MSTd, contrary to V5/MT, demonstrates a higher preference to radial flow than to translational motion (Morrone et al. 2000). These differences in functional properties of V5/MT and MST while both are highly responsive to visual motion signals is likely to drive their distinct laminar profiles in response to retinal, objective, and pursuit motion cues. Retinotopic coding in early visual cortex has revealed the involvement of V1 and ventral areas V2/V3 in speed judgements based on retinal motion, whereas dorsal V2/V3 receives extra-retinal speed signals during pursuit (Lebranchu et al. 2010). Similarly, it has been shown that areas V1-V3 respond to retinal motion, but they are also responsive to pursuit eye movement signals in the absence of retinal motion (Fischer et al. 2012a). These results favor the notion that already early visual regions rely on extra-retinal signals for a subsequent segregation of self-induced or externally induced motion signals. They may also be suggestive of a predictive coding account indicating that feedback connections from higher to lower-order visual areas carry predictions of lower level neural activations, whereas feedforward signals carry the residual errors between the predictions and the actual lower-level activities (Rao and Ballard 1999).

Feedforward and Feedback Signals

In contrast to early visual areas involved in processing primary visual inputs, areas such as V3A, MST and more parietal regions like VIP seem to be candidate regions for the integration of visual self-motion cues, efference copies and predictive signals from other regions. MST and VIP, contrary to V5/MT, have been shown to integrate visual and vestibular self-motion signals and hence have been labeled multisensory in the context of ego-motion processing (Bremmer et al. 2002; Chowdhury et al. 2009).

Bottom-up feedforward signals convey sensory inputs from the external world into the brain, whereas top-down feedback signals project the internal representation of sensory inputs (Kok et al. 2016). Within each cortical region, feedforward and feedback signals are largely segregated, with top-down feedback signals arriving at superficial layers and bottom-up sensory inputs targeting middle layers (Felleman and Van Essen 1991; Rockland and Pandya 1979). The integration of feedforward and feedback signals across cortical layers is one of the critical requirements for healthy perception and cognition. This integration results in a feedback-mediated activity with a specific laminar profile distinct from that elicited by

bottom-up sensory inputs (Kok et al. 2016). If there were segregated populations of neurons across cortical layers responding differently to objective and to retinal motion we would expect the feedback-mediated activity in response to objective motion, resulting from the integration between feedforward retinal signal and feedback pursuit signal, to have a specific laminar profile that is distinct from the activation elicited by bottom-up sensory input from retina. Although we did not observe any significant difference between laminar profiles of objective and retinal signal, it still does not provide enough evidence to reason out the speculation that the response to objective motion may in fact be the result of integration between retinal and pursuit motion signals. Any of the following parameters can potentially cast shadow over possible depth-dependent changes in laminar profiles of each motion type. (1): spatial bias of the BOLD signal toward superficial layers due to the presence of pial vessels and diving venules (Polimeni et al. 2018; Ahveninen et al. 2016), which can be amplified considering the significant response of all three ROIS i.e. MT, pMST, and V1 to both retinal and objective motion, (2): potential artifactual coupling of the hemodynamic signal across cortical depth due to the presence of radial vessels imparting spatial spread of the BOLD signal perpendicular to the cortical surface, and (3): neuronal activation in the deep layers triggering the change in the BOLD signal across all layers due to the downstream effect, in which small intracortical venules drain deoxygenated blood from deeper layers up through superficial layers up to the pial vasculature.

Close resemblance between grid-like regularity of local vascular anatomy and the layout of cortical layers and columns is another issue that complicates interpretation of laminar signal. Principle arterioles and venules, oriented perpendicularly to the cortical surface, are spaced roughly every 0.75–1.0 mm (Duvernoy, Delon, and Vannson 1981), similar to the spatial periodicity of many columnar structures in human V1 (Polimeni et al. 2018). This evident spatial regularity has paved the way for emergence of theories regarding the functional relationship between columnar organizations and these “vascular units” (Harel et al. 2010; Gardner 2010), which may or may not hold across brain regions (Adams et al. 2014; Blinder et al. 2013). Geometrical regularity of cortical vasculature i.e. tangential extension of pial vessels over the cortical surface and radial expansion of intra-cortical venules across the cortical depth exerts an influence on the BOLD signal that is a function of the angle between the orientation of the static magnetic field (B_0) and the local cortical surface normal (Gagnon et al. 2015). This leads to a systematic variation in depth-dependent coupling of the BOLD

signal, and also signal contamination from large pial vessels across the cortex, which brings further challenges into laminar fMRI studies.

References

- Adams, Daniel L, Valentina Piserchia, John R Economides, and Jonathan C Horton. 2014. 'Vascular supply of the cerebral cortex is specialized for cell layers but not columns', *Cerebral cortex*, 25: 3673-81.
- Ahveninen, J., W. T. Chang, S. Huang, B. Keil, N. Kopco, S. Rossi, G. Bonmassar, T. Witzel, and J. R. Polimeni. 2016. 'Intracortical depth analyses of frequency-sensitive regions of human auditory cortex using 7TfMRI', *Neuroimage*, 143: 116-27.
- Anderson, J. C., and K. A. Martin. 2005. 'Connection from cortical area V2 to V3 A in macaque monkey', *J Comp Neurol*, 488: 320-30.
- Anderson, J. C., and K. A. Martin. 2009. 'The synaptic connections between cortical areas V1 and V2 in macaque monkey', *J Neurosci*, 29: 11283-93.
- Andersson, J. L. R., and S. N. Sotiropoulos. 2016. 'An integrated approach to correction for off-resonance effects and subject movement in diffusion MR imaging', *Neuroimage*, 125: 1063-78.
- Andersson, Jesper L. R., Stefan Skare, and John Ashburner. 2003. 'How to correct susceptibility distortions in spin-echo echo-planar images: application to diffusion tensor imaging', *Neuroimage*, 20: 870-88.
- Angelucci, A., and J. Bullier. 2003. 'Reaching beyond the classical receptive field of V1 neurons: horizontal or feedback axons?', *J Physiol Paris*, 97: 141-54.
- Annese, J., A. Pitiot, I. D. Dinov, and A. W. Toga. 2004. 'A myelo-architectonic method for the structural classification of cortical areas', *Neuroimage*, 21: 15-26.
- Arbabshirani, M. R., S. Plis, J. Sui, and V. D. Calhoun. 2017. 'Single subject prediction of brain disorders in neuroimaging: Promises and pitfalls', *Neuroimage*, 145: 137-65.
- Arnoldussen, D. M., J. Goossens, and A. V. van den Berg. 2011. 'Adjacent visual representations of self-motion in different reference frames', *Proc Natl Acad Sci U S A*, 108: 11668-73.
- Baez-Yanez, M. G., P. Ehses, C. Mirkes, P. S. Tsai, D. Kleinfeld, and K. Scheffler. 2017. 'The impact of vessel size, orientation and intravascular contribution on the neurovascular fingerprint of BOLD bSSFP fMRI', *Neuroimage*, 163: 13-23.
- Bartels, A., N. K. Logothetis, and K. Moutoussis. 2008. 'fMRI and its interpretations: an illustration on directional selectivity in area V5/MT', *Trends Neurosci*, 31: 444-53.
- Bartels, A., S. Zeki, and N. K. Logothetis. 2008. 'Natural vision reveals regional specialization to local motion and to contrast-invariant, global flow in the human brain', *Cereb Cortex*, 18: 705-17.
- Bastos, A. M., W. M. Usrey, R. A. Adams, G. R. Mangun, P. Fries, and K. J. Friston. 2012. 'Canonical microcircuits for predictive coding', *Neuron*, 76: 695-711.
- Bastos, A. M., J. Vezoli, C. A. Bosman, J. M. Schoffelen, R. Oostenveld, J. R. Dowdall, P. De Weerd, H. Kennedy, and P. Fries. 2015. 'Visual areas exert feedforward and feedback influences through distinct frequency channels', *Neuron*, 85: 390-401.
- Bause, J., In, M.-H., Ehses, P., Shajan, G., Speck, O., Pohmann, R. 2015. 'Distortion-Corrected High Resolution Zoomed fMRI at 9.4 T', *Poster presented at 23rd Annual Meeting and Exhibition of the International Society for Magnetic Resonance in Medicine (ISMRM 2015)*.
- Bieri, O., and K. Scheffler. 2007. 'Effect of diffusion in inhomogeneous magnetic fields on balanced steady-state free precession', *NMR Biomed*, 20: 1-10.

- Blinder, P., P. S. Tsai, J. P. Kaufhold, P. M. Knutsen, H. Suhl, and D. Kleinfeld. 2013. 'The cortical angiome: an interconnected vascular network with noncolumnar patterns of blood flow', *Nat Neurosci*, 16: 889-97.
- Bok, Siegfried Thomas. 1929. 'Der Einfluss der in den Furchen und Windungen auftretenden Krümmungen der Großhirnrinde auf die Rindenarchitektur', *Zeitschrift für die gesamte Neurologie und Psychiatrie*, 121: 682-750.
- Boussaoud, D., L. G. Ungerleider, and R. Desimone. 1990. 'Pathways for motion analysis: cortical connections of the medial superior temporal and fundus of the superior temporal visual areas in the macaque', *J Comp Neurol*, 296: 462-95.
- Bowen, C, J Mason, R Menon, and J Gati. 2006. 'High field balanced-SSFP fMRI: examining a diffusion contrast mechanism using varied flip angles', *Proc ISMRM, Seattle*: 665.
- Bowen, Chris, R. S Menon, and Sabiha Gati. 2005. *High field balanced-SSFP fMRI: A BOLD technique with excellent tissue sensitivity and superior large vessel suppression*.
- Bremmer, F., F. Klam, J. R. Duhamel, S. Ben Hamed, and W. Graf. 2002. 'Visual-vestibular interactive responses in the macaque ventral intraparietal area (VIP)', *Eur J Neurosci*, 16: 1569-86.
- Bremmer, F., A. Schlack, N. J. Shah, O. Zafiris, M. Kubischik, K. Hoffmann, K. Zilles, and G. R. Fink. 2001. 'Polymodal motion processing in posterior parietal and premotor cortex: a human fMRI study strongly implies equivalencies between humans and monkeys', *Neuron*, 29: 287-96.
- Brodmann, K. 1909. *Vergleichende Lokalisationslehre der Großhirnrinde*.
- Brown, E. C., and M. Brune. 2012. 'Evolution of social predictive brains?', *Front Psychol*, 3: 414.
- Cardin, V., and A. T. Smith. 2010. 'Sensitivity of human visual and vestibular cortical regions to egomotion-compatible visual stimulation', *Cereb Cortex*, 20: 1964-73.
- Cardin, V., and A. T. Smith. 2011. 'Sensitivity of human visual cortical area V6 to stereoscopic depth gradients associated with self-motion', *J Neurophysiol*, 106: 1240-9.
- Chaimow, D., E. Yacoub, K. Ugurbil, and A. Shmuel. 2011. 'Modeling and analysis of mechanisms underlying fMRI-based decoding of information conveyed in cortical columns', *Neuroimage*, 56: 627-42.
- Chapman, B., R. Turner, R. J. Ordidge, M. Doyle, M. Cawley, R. Coxon, P. Glover, and P. Mansfield. 1987. 'Real-time movie imaging from a single cardiac cycle by NMR', *Magn Reson Med*, 5: 246-54.
- Chen, Nan-kuei, and Alice M. Wyrwicz. 1999. 'Correction for EPI distortions using multi-echo gradient-echo imaging', *Magnetic Resonance in Medicine*, 41: 1206-13.
- Cheng, K., R. A. Waggoner, and K. Tanaka. 2001. 'Human ocular dominance columns as revealed by high-field functional magnetic resonance imaging', *Neuron*, 32: 359-74.
- Chowdhury, S. A., K. Takahashi, G. C. DeAngelis, and D. E. Angelaki. 2009. 'Does the middle temporal area carry vestibular signals related to self-motion?', *J Neurosci*, 29: 12020-30.
- Chukoskie, L., and J. A. Movshon. 2009. 'Modulation of visual signals in macaque MT and MST neurons during pursuit eye movement', *J Neurophysiol*, 102: 3225-33.
- Clare, S., and P. Jezzard. 2001. 'Rapid T(1) mapping using multislice echo planar imaging', *Magn Reson Med*, 45: 630-4.
- Clark, A. 2013. 'Whatever next? Predictive brains, situated agents, and the future of cognitive science', *Behav Brain Sci*, 36: 181-204.

- Collins, C. M., W. Liu, W. Schreiber, Q. X. Yang, and M. B. Smith. 2005. 'Central brightening due to constructive interference with, without, and despite dielectric resonance', *J Magn Reson Imaging*, 21: 192-6.
- Daddaoua, N., P. W. Dicke, and P. Thier. 2014. 'Eye position information is used to compensate the consequences of ocular torsion on V1 receptive fields', *Nat Commun*, 5: 3047.
- Dale, A. M., B. Fischl, and M. I. Sereno. 1999. 'Cortical surface-based analysis. I. Segmentation and surface reconstruction', *Neuroimage*, 9: 179-94.
- De Martino, F., M. Moerel, K. Ugurbil, R. Goebel, E. Yacoub, and E. Formisano. 2015. 'Frequency preference and attention effects across cortical depths in the human primary auditory cortex', *Proc Natl Acad Sci U S A*, 112: 16036-41.
- De Martino, F., M. Moerel, P. F. van de Moortele, K. Ugurbil, R. Goebel, E. Yacoub, and E. Formisano. 2013. 'Spatial organization of frequency preference and selectivity in the human inferior colliculus', *Nat Commun*, 4: 1386.
- De Martino, F., M. Moerel, J. Xu, P. F. van de Moortele, K. Ugurbil, R. Goebel, E. Yacoub, and E. Formisano. 2015. 'High-Resolution Mapping of Myeloarchitecture In Vivo: Localization of Auditory Areas in the Human Brain', *Cereb Cortex*, 25: 3394-405.
- De Martino, F., S. Schmitter, M. Moerel, J. Tian, K. Ugurbil, E. Formisano, E. Yacoub, and P. F. de Moortele. 2012. 'Spin echo functional MRI in bilateral auditory cortices at 7 T: an application of B(1) shimming', *Neuroimage*, 63: 1313-20.
- de Zwart, J. A., P. van Gelderen, P. Kellman, and J. H. Duyn. 2002. 'Application of sensitivity-encoded echo-planar imaging for blood oxygen level-dependent functional brain imaging', *Magn Reson Med*, 48: 1011-20.
- Dicke, P. W., S. Chakraborty, and P. Thier. 2008. 'Neuronal correlates of perceptual stability during eye movements', *Eur J Neurosci*, 27: 991-1002.
- Douglas, R. J., and K. A. Martin. 2004. 'Neuronal circuits of the neocortex', *Annu Rev Neurosci*, 27: 419-51.
- Dumoulin, S. O., R. G. Bittar, N. J. Kabani, C. L. Baker, Jr., G. Le Goualher, G. Bruce Pike, and A. C. Evans. 2000. 'A new anatomical landmark for reliable identification of human area V5/MT: a quantitative analysis of sulcal patterning', *Cereb Cortex*, 10: 454-63.
- Duvernoy, H. M., S. Delon, and J. L. Vannson. 1981. 'Cortical blood vessels of the human brain', *Brain Res Bull*, 7: 519-79.
- Economo, Von. 1929. *The Cytoarchitectonics of the Human Cerebral Cortex* (Oxford Univ. Press: Oxford).
- Edelstein, W. A., G. H. Glover, C. J. Hardy, and R. W. Redington. 1986. 'The intrinsic signal-to-noise ratio in NMR imaging', *Magn Reson Med*, 3: 604-18.
- Erickson, R. G., and P. Thier. 1991. 'A neuronal correlate of spatial stability during periods of self-induced visual motion', *Exp Brain Res*, 86: 608-16.
- Ernst, T., O. Speck, L. Itti, and L. Chang. 1999. 'Simultaneous correction for interscan patient motion and geometric distortions in echoplanar imaging', *Magn Reson Med*, 42: 201-5.
- Fatterpekar, G. M., B. N. Delman, W. W. Boonn, S. H. Gultekin, Z. A. Fayad, P. R. Hoff, and T. P. Naidich. 2003. 'MR microscopy of normal human brain', *Magn Reson Imaging Clin N Am*, 11: 641-53.
- Faull, O. K., M. Jenkinson, S. Clare, and K. T. Pattinson. 2015. 'Functional subdivision of the human periaqueductal grey in respiratory control using 7 tesla fMRI', *Neuroimage*, 113: 356-64.

- Felleman, D. J., and D. C. Van Essen. 1991. 'Distributed hierarchical processing in the primate cerebral cortex', *Cereb Cortex*, 1: 1-47.
- Fischer, E., H. H. Bulthoff, N. K. Logothetis, and A. Bartels. 2012a. 'Human areas V3A and V6 compensate for self-induced planar visual motion', *Neuron*, 73: 1228-40.
- Fischer, E., H. H. Bulthoff, N. K. Logothetis, and A. Bartels. 2012b. 'Visual motion responses in the posterior cingulate sulcus: a comparison to V5/MT and MST', *Cereb Cortex*, 22: 865-76.
- Fischl, B., and A. M. Dale. 2000. 'Measuring the thickness of the human cerebral cortex from magnetic resonance images', *Proc Natl Acad Sci U S A*, 97: 11050-5.
- Fischl, B., A. Liu, and A. M. Dale. 2001. 'Automated manifold surgery: constructing geometrically accurate and topologically correct models of the human cerebral cortex', *IEEE Trans Med Imaging*, 20: 70-80.
- Fischl, B., D. H. Salat, E. Busa, M. Albert, M. Dieterich, C. Haselgrove, A. van der Kouwe, R. Killiany, D. Kennedy, S. Klaveness, A. Montillo, N. Makris, B. Rosen, and A. M. Dale. 2002. 'Whole brain segmentation: automated labeling of neuroanatomical structures in the human brain', *Neuron*, 33: 341-55.
- Fischl, B., M. I. Sereno, and A. M. Dale. 1999. 'Cortical surface-based analysis. II: Inflation, flattening, and a surface-based coordinate system', *Neuroimage*, 9: 195-207.
- Fracasso, A., P. R. Luijten, S. O. Dumoulin, and N. Petridou. 2018. 'Laminar imaging of positive and negative BOLD in human visual cortex at 7T', *Neuroimage*, 164: 100-11.
- Fujimoto, K., J. R. Polimeni, A. J. van der Kouwe, M. Reuter, T. Kober, T. Benner, B. Fischl, and L. L. Wald. 2014. 'Quantitative comparison of cortical surface reconstructions from MP2RAGE and multi-echo MPRAGE data at 3 and 7 T', *Neuroimage*, 90: 60-73.
- Fukushima, K., T. Yamanobe, Y. Shinmei, and J. Fukushima. 2002. 'Predictive responses of periarculate pursuit neurons to visual target motion', *Exp Brain Res*, 145: 104-20.
- Gagnon, L., S. Sakadzic, F. Lesage, J. J. Musacchia, J. Lefebvre, Q. Fang, M. A. Yucel, K. C. Evans, E. T. Mandeville, J. Cohen-Adad, J. R. Polimeni, M. A. Yaseen, E. H. Lo, D. N. Greve, R. B. Buxton, A. M. Dale, A. Devor, and D. A. Boas. 2015. 'Quantifying the microvascular origin of BOLD-fMRI from first principles with two-photon microscopy and an oxygen-sensitive nanoprobe', *J Neurosci*, 35: 3663-75.
- Galletti, C., P. P. Battaglini, and G. Aicardi. 1988. 'Real-motion' cells in visual area V2 of behaving macaque monkeys', *Exp Brain Res*, 69: 279-88.
- Galletti, C., P. P. Battaglini, and P. Fattori. 1990. 'Real-motion' cells in area V3A of macaque visual cortex', *Exp Brain Res*, 82: 67-76.
- Galletti, C., and P. Fattori. 2003. 'Neuronal mechanisms for detection of motion in the field of view', *Neuropsychologia*, 41: 1717-27.
- Galletti, C., and P. Fattori. 2018. 'The dorsal visual stream revisited: Stable circuits or dynamic pathways?', *Cortex*, 98: 203-17.
- Galletti, C., M. Gamberini, D. F. Kutz, P. Fattori, G. Luppino, and M. Matelli. 2001. 'The cortical connections of area V6: an occipito-parietal network processing visual information', *Eur J Neurosci*, 13: 1572-88.
- Galletti, C., D. F. Kutz, M. Gamberini, R. Breveglieri, and P. Fattori. 2003. 'Role of the medial parieto-occipital cortex in the control of reaching and grasping movements', *Exp Brain Res*, 153: 158-70.
- Galletti, C., S. Squatrito, P. P. Battaglini, and M. Grazia Maioli. 1984. 'Real-motion' cells in the primary visual cortex of macaque monkeys', *Brain Res*, 301: 95-110.
- Gardner, J. L. 2010. 'Is cortical vasculature functionally organized?', *Neuroimage*, 49: 1953-6.
- Gati, JS, and RS Menon. 2002. "High resolution fMRI using 3D-EPI." In *Proc. ISMRM*, 124.

- Gegenfurtner, K. R., D. Xing, B. H. Scott, and M. J. Hawken. 2003. 'A comparison of pursuit eye movement and perceptual performance in speed discrimination', *J Vis*, 3: 865-76.
- Gibson, J. J. 1954. 'The visual perception of objective motion and subjective movement', *Psychol Rev*, 61: 304-14.
- Glasser, M. F., S. N. Sotiropoulos, J. A. Wilson, T. S. Coalson, B. Fischl, J. L. Andersson, J. Xu, S. Jbabdi, M. Webster, J. R. Polimeni, D. C. Van Essen, M. Jenkinson, and W. U-Minn HCP Consortium. 2013. 'The minimal preprocessing pipelines for the Human Connectome Project', *Neuroimage*, 80: 105-24.
- Goense, J. B., and N. K. Logothetis. 2008. 'Neurophysiology of the BOLD fMRI signal in awake monkeys', *Curr Biol*, 18: 631-40.
- Goense, J., H. Merkle, and N. K. Logothetis. 2012. 'High-resolution fMRI reveals laminar differences in neurovascular coupling between positive and negative BOLD responses', *Neuron*, 76: 629-39.
- Goossens, J., S. P. Dukelow, R. S. Menon, T. Vilis, and A. V. van den Berg. 2006. 'Representation of head-centric flow in the human motion complex', *J Neurosci*, 26: 5616-27.
- Gowland, P., and P. Mansfield. 1993. 'Accurate measurement of T1 in vivo in less than 3 seconds using echo-planar imaging', *Magnetic Resonance in Medicine*, 30: 351-54.
- Greve, D. N., and B. Fischl. 2009. 'Accurate and robust brain image alignment using boundary-based registration', *Neuroimage*, 48: 63-72.
- Griswold, M. A., P. M. Jakob, R. M. Heidemann, M. Nittka, V. Jellus, J. Wang, B. Kiefer, and A. Haase. 2002. 'Generalized autocalibrating partially parallel acquisitions (GRAPPA)', *Magn Reson Med*, 47: 1202-10.
- Haarmeier, T., P. Thier, M. Repnow, and D. Petersen. 1997. 'False perception of motion in a patient who cannot compensate for eye movements', *Nature*, 389: 849-52.
- Hagberg, G. E., J. Bause, T. Ethofer, P. Ehses, T. Dresler, C. Herbert, R. Pohmann, G. Shajan, A. Fallgatter, M. A. Pavlova, and K. Scheffler. 2017. 'Whole brain MP2RAGE-based mapping of the longitudinal relaxation time at 9.4T', *Neuroimage*, 144: 203-16.
- Harel, N., P. J. Bolan, R. Turner, K. Ugurbil, and E. Yacoub. 2010. 'Recent Advances in High-Resolution MR Application and Its Implications for Neurovascular Coupling Research', *Front Neuroenergetics*, 2: 130.
- Harris, K. D., and T. D. Mrsic-Flogel. 2013. 'Cortical connectivity and sensory coding', *Nature*, 503: 51-8.
- Heeger, D. J. 2017. 'Theory of cortical function', *Proc Natl Acad Sci U S A*, 114: 1773-82.
- Heidemann, Robin M, Alfred Anwander, Thorsten Feiweier, Thomas R Knösche, and Robert Turner. 2012. 'k-space and q-space: combining ultra-high spatial and angular resolution in diffusion imaging using ZOOPPA at 7 T', *Neuroimage*, 60: 967-78.
- Heinzle, J., P. J. Koopmans, H. E. M. den Ouden, S. Raman, and K. E. Stephan. 2016. 'A hemodynamic model for layered BOLD signals', *Neuroimage*, 125: 556-70.
- Helfrich, R. F., H. G. Becker, and T. Haarmeier. 2013. 'Processing of coherent visual motion in topographically organized visual areas in human cerebral cortex', *Brain Topogr*, 26: 247-63.
- Hesselmann, G., C. A. Kell, and A. Kleinschmidt. 2008. 'Ongoing activity fluctuations in hMT+ bias the perception of coherent visual motion', *J Neurosci*, 28: 14481-5.
- Hilgetag, C. C., and H. Barbas. 2006. 'Role of mechanical factors in the morphology of the primate cerebral cortex', *PLoS Comput Biol*, 2: e22.

- Holland, D., J. M. Kuperman, and A. M. Dale. 2010. 'Efficient correction of inhomogeneous static magnetic field-induced distortion in Echo Planar Imaging', *Neuroimage*, 50: 175-83.
- Horga, G., K. C. Schatz, A. Abi-Dargham, and B. S. Peterson. 2014. 'Deficits in predictive coding underlie hallucinations in schizophrenia', *J Neurosci*, 34: 8072-82.
- Hubel, D. H., and T. N. Wiesel. 1972. 'Laminar and columnar distribution of geniculate-cortical fibers in the macaque monkey', *J Comp Neurol*, 146: 421-50.
- Huber, L., J. Goense, A. J. Kennerley, D. Ivanov, S. N. Krieger, J. Lepsien, R. Trampel, R. Turner, and H. E. Moller. 2014. 'Investigation of the neurovascular coupling in positive and negative BOLD responses in human brain at 7 T', *Neuroimage*, 97: 349-62.
- Huber, L., J. Goense, A. J. Kennerley, R. Trampel, M. Guidi, E. Reimer, D. Ivanov, N. Neef, C. J. Gauthier, R. Turner, and H. E. Moller. 2015. 'Cortical lamina-dependent blood volume changes in human brain at 7 T', *Neuroimage*, 107: 23-33.
- Huber, L., D. Ivanov, D. A. Handwerker, S. Marrett, M. Guidi, K. Uludag, P. A. Bandettini, and B. A. Poser. 2018. 'Techniques for blood volume fMRI with VASO: From low-resolution mapping towards sub-millimeter layer-dependent applications', *Neuroimage*, 164: 131-43.
- Huber, L., K. Uludag, and H. E. Moller. 2017. 'Non-BOLD contrast for laminar fMRI in humans: CBF, CBV, and CMRO₂', *Neuroimage*.
- Huber, Laurentius, Sean Marrett, Daniel Handwerker, Adam Thomas, Benjamin Gutierrez, Chris Steel, Dimo Ivanov, Benedikt Poser, and Peter Bandettini. 2017. 'Fast dynamic measurement of functional T1 and grey matter thickness changes during brain activation at 7T', *F1000Research*, 6.
- Huk, A. C., D. Ress, and D. J. Heeger. 2001. 'Neuronal basis of the motion aftereffect reconsidered', *Neuron*, 32: 161-72.
- Hutton, C., A. Bork, O. Josephs, R. Deichmann, J. Ashburner, and R. Turner. 2002. 'Image distortion correction in fMRI: A quantitative evaluation', *Neuroimage*, 16: 217-40.
- Hwang, Tsang-Lin, Peter CM van Zijl, and Michael Garwood. 1999. "Asymmetric adiabatic pulses for NH selection." In.: Elsevier.
- Ilg, U. J., and J. Churan. 2004. 'Motion perception without explicit activity in areas MT and MST', *J Neurophysiol*, 92: 1512-23.
- Ilg, U. J., S. Schumann, and P. Thier. 2004. 'Posterior parietal cortex neurons encode target motion in world-centered coordinates', *Neuron*, 43: 145-51.
- Ilg, U. J., and P. Thier. 2008. 'The neural basis of smooth pursuit eye movements in the rhesus monkey brain', *Brain Cogn*, 68: 229-40.
- In, M. H., and O. Speck. 2012. 'Highly accelerated PSF-mapping for EPI distortion correction with improved fidelity', *Magma*, 25: 183-92.
- Inaba, N., S. Shinomoto, S. Yamane, A. Takemura, and K. Kawano. 2007. 'MST neurons code for visual motion in space independent of pursuit eye movements', *J Neurophysiol*, 97: 3473-83.
- Ivanov, D, B Poser, M Havlicek, and K Uludağ. 2015. "Fast quantitative T1-mapping at ultra-high field using inversion-recovery echo planar imaging." In *21st Annual Meeting of the Organization for Human Brain Mapping*.
- Ivanov, Dimo, Benedikt A Poser, Laurentius Huber, Josef Pfeuffer, and Kâmil Uludağ. 2017. 'Optimization of simultaneous multislice EPI for concurrent functional perfusion and BOLD signal measurements at 7T', *Magnetic Resonance in Medicine*, 78: 121-29.

- Kamitani, Y., and F. Tong. 2005. 'Decoding the visual and subjective contents of the human brain', *Nat Neurosci*, 8: 679-85.
- Kashyap, S., D. Ivanov, M. Havlicek, B. A. Poser, and K. Uludag. 2018. 'Impact of acquisition and analysis strategies on cortical depth-dependent fMRI', *Neuroimage*, 168: 332-44.
- Kashyap, Sriranga, Dimo Ivanov, Martin Havlicek, Benedikt Poser, and Kamil Uludag. 2016. *High-resolution T1-mapping using inversion-recovery EPI and its application to cortical depth-dependent fMRI at 7 Tesla*.
- Katzel, D., B. V. Zeman, C. Buetfering, M. Wolfel, and G. Miesenbock. 2011. 'The columnar and laminar organization of inhibitory connections to neocortical excitatory cells', *Nat Neurosci*, 14: 100-7.
- Keil, B., and L. L. Wald. 2013. 'Massively parallel MRI detector arrays', *J Magn Reson*, 229: 75-89.
- Kemper, V. G., F. De Martino, A. T. Vu, B. A. Poser, D. A. Feinberg, R. Goebel, and E. Yacoub. 2015. 'Sub-millimeter T2 weighted fMRI at 7 T: comparison of 3D-GRASE and 2D SE-EPI', *Front Neurosci*, 9: 163.
- Kim, J., C. J. Matney, A. Blankenship, S. Hestrin, and S. P. Brown. 2014. 'Layer 6 corticothalamic neurons activate a cortical output layer, layer 5a', *J Neurosci*, 34: 9656-64.
- Kim, T. S., J. Lee, J. H. Lee, G. H. Glover, and J. M. Pauly. 2012. 'Analysis of the BOLD Characteristics in Pass-Band bSSFP fMRI', *Int J Imaging Syst Technol*, 22: 23-32.
- Kleinnijenhuis, M., T. van Mourik, D. G. Norris, D. J. Ruiter, A. M. van Cappellen van Walsum, and M. Barth. 2015. 'Diffusion tensor characteristics of gyrencephaly using high resolution diffusion MRI in vivo at 7T', *Neuroimage*, 109: 378-87.
- Kok, P., L. J. Bains, T. van Mourik, D. G. Norris, and F. P. de Lange. 2016. 'Selective Activation of the Deep Layers of the Human Primary Visual Cortex by Top-Down Feedback', *Curr Biol*, 26: 371-6.
- Konen, C. S., and S. Kastner. 2008. 'Representation of eye movements and stimulus motion in topographically organized areas of human posterior parietal cortex', *J Neurosci*, 28: 8361-75.
- Koopmans, P. J., M. Barth, and D. G. Norris. 2010. 'Layer-specific BOLD activation in human V1', *Hum Brain Mapp*, 31: 1297-304.
- Koopmans, P. J., M. Barth, S. Orzada, and D. G. Norris. 2011. 'Multi-echo fMRI of the cortical laminae in humans at 7 T', *Neuroimage*, 56: 1276-85.
- Larkum, M. 2013a. 'A cellular mechanism for cortical associations: an organizing principle for the cerebral cortex', *Trends Neurosci*, 36: 141-51.
- Larkum, M. E. 2013b. 'The yin and yang of cortical layer 1', *Nat Neurosci*, 16: 114-5.
- Lebranchu, P., J. Bastin, M. Pelegrini-Issac, S. Lehericy, A. Berthoz, and G. A. Orban. 2010. 'Retinotopic coding of extraretinal pursuit signals in early visual cortex', *Cereb Cortex*, 20: 2172-87.
- Lee, T. S., and D. Mumford. 2003. 'Hierarchical Bayesian inference in the visual cortex', *J Opt Soc Am A Opt Image Sci Vis*, 20: 1434-48.
- Leprince, Y., F. Poupon, T. Delzescaux, D. Hasboun, C. Poupon, and D. Rivière. 2015. "Combined Laplacian-equivolumic model for studying cortical lamination with ultra high field MRI (7 T)." In *2015 IEEE 12th International Symposium on Biomedical Imaging (ISBI)*, 580-83.
- Logothetis, N. K. 2002. 'The neural basis of the blood-oxygen-level-dependent functional magnetic resonance imaging signal', *Philos Trans R Soc Lond B Biol Sci*, 357: 1003-37.

- Logothetis, N. K. 2008. 'What we can do and what we cannot do with fMRI', *Nature*, 453: 869-78.
- Loureiro, J. R., G. E. Hagberg, T. Ethofer, M. Erb, J. Bause, P. Ehses, K. Scheffler, and M. Himmelbach. 2017. 'Depth-dependence of visual signals in the human superior colliculus at 9.4 T', *Hum Brain Mapp*, 38: 574-87.
- Lusebrink, F., A. Wollrab, and O. Speck. 2013. 'Cortical thickness determination of the human brain using high resolution 3T and 7T MRI data', *Neuroimage*, 70: 122-31.
- Lyon, D. C., J. J. Nassi, and E. M. Callaway. 2010. 'A disynaptic relay from superior colliculus to dorsal stream visual cortex in macaque monkey', *Neuron*, 65: 270-9.
- M. Smith, Stephen, Mark Jenkinson, Mark W. Woolrich, Christian F. Beckmann, Timothy E. J. Behrens, Heidi Johansen-Berg, Peter Bannister, Medana Luca, Ivana Drobnjak, David Flitney, Rami Niazy, and James Saunders. 2004. *Advances in Functional and Structural MR Image Analysis and Implementation as FSL Technical Report TR04SS2*.
- Markov, N. T., and H. Kennedy. 2013. 'The importance of being hierarchical', *Curr Opin Neurobiol*, 23: 187-94.
- Markov, N. T., J. Vezoli, P. Chameau, A. Falchier, R. Quilodran, C. Huisoud, C. Lamy, P. Misery, P. Giroud, S. Ullman, P. Barone, C. Dehay, K. Knoblauch, and H. Kennedy. 2014. 'Anatomy of hierarchy: feedforward and feedback pathways in macaque visual cortex', *J Comp Neurol*, 522: 225-59.
- Markuerkiaga, I., M. Barth, and D. G. Norris. 2016. 'A cortical vascular model for examining the specificity of the laminar BOLD signal', *Neuroimage*, 132: 491-98.
- Marques, J. P., T. Kober, G. Krueger, W. van der Zwaag, P. F. Van de Moortele, and R. Gruetter. 2010. 'MP2RAGE, a self bias-field corrected sequence for improved segmentation and T1-mapping at high field', *Neuroimage*, 49: 1271-81.
- Merboldt, K. D., J. Finsterbusch, and J. Frahm. 2000. 'Reducing inhomogeneity artifacts in functional MRI of human brain activation-thin sections vs gradient compensation', *J Magn Reson*, 145: 184-91.
- Miller, K. L., B. A. Hargreaves, J. Lee, D. Ress, R. C. deCharms, and J. M. Pauly. 2003. 'Functional brain imaging using a blood oxygenation sensitive steady state', *Magn Reson Med*, 50: 675-83.
- Miller, K. L., and P. Jezzard. 2008. 'Modeling SSFP functional MRI contrast in the brain', *Magn Reson Med*, 60: 661-73.
- Miller, K. L., S. M. Smith, P. Jezzard, G. C. Wiggins, and C. J. Wiggins. 2007. 'Signal and noise characteristics of SSFP FMRI: a comparison with GRE at multiple field strengths', *Neuroimage*, 37: 1227-36.
- Morrone, M. C., M. Tosetti, D. Montanaro, A. Fiorentini, G. Cioni, and D. C. Burr. 2000. 'A cortical area that responds specifically to optic flow, revealed by fMRI', *Nat Neurosci*, 3: 1322-8.
- Muckli, L., F. De Martino, L. Vizioli, L. S. Petro, F. W. Smith, K. Ugurbil, R. Goebel, and E. Yacoub. 2015. 'Contextual Feedback to Superficial Layers of V1', *Curr Biol*, 25: 2690-5.
- Muckli, Lars. 2010. 'What are we missing here? Brain imaging evidence for higher cognitive functions in primary visual cortex V1', *International Journal of Imaging Systems and Technology*, 20: 131-39.
- Mumford, D. 1992. 'On the computational architecture of the neocortex. II. The role of cortico-cortical loops', *Biol Cybern*, 66: 241-51.
- Nakamura, K., and C. L. Colby. 2002. 'Updating of the visual representation in monkey striate and extrastriate cortex during saccades', *Proc Natl Acad Sci U S A*, 99: 4026-31.

- Nasr, S., J. R. Polimeni, and R. B. Tootell. 2016. 'Interdigitated Color- and Disparity-Selective Columns within Human Visual Cortical Areas V2 and V3', *J Neurosci*, 36: 1841-57.
- Nau, M., A. Schindler, and A. Bartels. 2018. 'Real-motion signals in human early visual cortex', *Neuroimage*, 175: 379-87.
- Newton, A. T., B. P. Rogers, J. C. Gore, and V. L. Morgan. 2012. 'Improving measurement of functional connectivity through decreasing partial volume effects at 7 T', *Neuroimage*, 59: 2511-7.
- Norris, D. G. 2012. 'Spin-echo fMRI: The poor relation?', *Neuroimage*, 62: 1109-15.
- Olman, C. A., N. Harel, D. A. Feinberg, S. He, P. Zhang, K. Ugurbil, and E. Yacoub. 2012. 'Layer-specific fMRI reflects different neuronal computations at different depths in human V1', *PLoS One*, 7: e32536.
- Olman, C. A., S. Inati, and D. J. Heeger. 2007. 'The effect of large veins on spatial localization with GE BOLD at 3 T: Displacement, not blurring', *Neuroimage*, 34: 1126-35.
- Orban, G. A., D. Fize, H. Peuskens, K. Denys, K. Nelissen, S. Sunaert, J. Todd, and W. Vanduffel. 2003. 'Similarities and differences in motion processing between the human and macaque brain: evidence from fMRI', *Neuropsychologia*, 41: 1757-68.
- Ordidge, R. J., P. Gibbs, B. Chapman, M. K. Stehling, and P. Mansfield. 1990a. 'High-speed multislice T1 mapping using inversion-recovery echo-planar imaging', *Magnetic Resonance in Medicine*, 16: 238-45.
- Ordidge, R. J., P. Gibbs, B. Chapman, M. K. Stehling, and P. Mansfield. 1990b. 'High-speed multislice T1 mapping using inversion-recovery echo-planar imaging', *Magnetic Resonance in Medicine*, 16: 238-45.
- Park, H. J., and K. Friston. 2013. 'Structural and functional brain networks: from connections to cognition', *Science*, 342: 1238411.
- Petro, L. S., and L. Muckli. 2017. 'The laminar integration of sensory inputs with feedback signals in human cortex', *Brain Cogn*, 112: 54-57.
- Pfeuffer, J., P. F. van de Moortele, E. Yacoub, A. Shmuel, G. Adriany, P. Andersen, H. Merkle, M. Garwood, K. Ugurbil, and X. Hu. 2002. 'Zoomed functional imaging in the human brain at 7 Tesla with simultaneous high spatial and high temporal resolution', *Neuroimage*, 17: 272-86.
- Pitzalis, S., P. Fattori, and C. Galletti. 2012. 'The functional role of the medial motion area V6', *Front Behav Neurosci*, 6: 91.
- Pitzalis, S., P. Fattori, and C. Galletti. 2015. 'The human cortical areas V6 and V6A', *Vis Neurosci*, 32: E007.
- Pitzalis, S., C. Galletti, R. S. Huang, F. Patria, G. Committeri, G. Galati, P. Fattori, and M. I. Sereno. 2006. 'Wide-field retinotopy defines human cortical visual area v6', *J Neurosci*, 26: 7962-73.
- Pitzalis, S., M. I. Sereno, G. Committeri, P. Fattori, G. Galati, F. Patria, and C. Galletti. 2010. 'Human v6: the medial motion area', *Cereb Cortex*, 20: 411-24.
- Pitzalis, S., M. I. Sereno, G. Committeri, P. Fattori, G. Galati, A. Tosoni, and C. Galletti. 2013. 'The human homologue of macaque area V6A', *Neuroimage*, 82: 517-30.
- Pohmann, R., and K. Scheffler. 2013. 'A theoretical and experimental comparison of different techniques for B(1) mapping at very high fields', *NMR Biomed*, 26: 265-75.
- Polimeni, J. R., H. Bhat, T. Witzel, T. Benner, T. Feiweier, S. J. Inati, V. Renvall, K. Heberlein, and L. L. Wald. 2016. 'Reducing sensitivity losses due to respiration and motion in accelerated echo planar imaging by reordering the autocalibration data acquisition', *Magn Reson Med*, 75: 665-79.

- Polimeni, J. R., B. Fischl, D. N. Greve, and L. L. Wald. 2010a. 'Laminar analysis of 7T BOLD using an imposed spatial activation pattern in human V1', *Neuroimage*, 52: 1334-46.
- Polimeni, J. R., V. Renvall, N. Zaretskaya, and B. Fischl. 2018. 'Analysis strategies for high-resolution UHF-fMRI data', *Neuroimage*, 168: 296-320.
- Polimeni, Jonathan R., Bruce Fischl, Douglas N. Greve, and Lawrence L. Wald. 2010b. 'Laminar analysis of 7T BOLD using an imposed spatial activation pattern in human V1', *Neuroimage*, 52: 1334-46.
- Poser, Benedikt A, and Kawin Setsompop. 2018. 'Pulse sequences and parallel imaging for high spatiotemporal resolution MRI at ultra-high field', *Neuroimage*, 168: 101-18.
- Pruessmann, K. P., M. Weiger, M. B. Scheidegger, and P. Boesiger. 1999. 'SENSE: sensitivity encoding for fast MRI', *Magn Reson Med*, 42: 952-62.
- Rao, R. P., and D. H. Ballard. 1999. 'Predictive coding in the visual cortex: a functional interpretation of some extra-classical receptive-field effects', *Nat Neurosci*, 2: 79-87.
- Renvall, V., T. Witzel, L. L. Wald, and J. R. Polimeni. 2016. 'Automatic cortical surface reconstruction of high-resolution T1 echo planar imaging data', *Neuroimage*, 134: 338-54.
- Ress, D., G. H. Glover, J. Liu, and B. Wandell. 2007. 'Laminar profiles of functional activity in the human brain', *Neuroimage*, 34: 74-84.
- Roche, A. 2011. 'A four-dimensional registration algorithm with application to joint correction of motion and slice timing in fMRI', *IEEE Trans Med Imaging*, 30: 1546-54.
- Rockland, K. S., and D. N. Pandya. 1979. 'Laminar origins and terminations of cortical connections of the occipital lobe in the rhesus monkey', *Brain Res*, 179: 3-20.
- Rockland, K. S., and A. Virga. 1989. 'Terminal arbors of individual "feedback" axons projecting from area V2 to V1 in the macaque monkey: a study using immunohistochemistry of anterogradely transported Phaseolus vulgaris-leucoagglutinin', *J Comp Neurol*, 285: 54-72.
- Roelfsema, P. R., and F. P. de Lange. 2016. 'Early Visual Cortex as a Multiscale Cognitive Blackboard', *Annu Rev Vis Sci*, 2: 131-51.
- Royden, C. S., M. S. Banks, and J. A. Crowell. 1992. 'The perception of heading during eye movements', *Nature*, 360: 583-5.
- Satpute, A. B., T. D. Wager, J. Cohen-Adad, M. Bianciardi, J. K. Choi, J. T. Buhle, L. L. Wald, and L. F. Barrett. 2013. 'Identification of discrete functional subregions of the human periaqueductal gray', *Proc Natl Acad Sci U S A*, 110: 17101-6.
- Scheffler, K., and P. Ehses. 2016. 'High-resolution mapping of neuronal activation with balanced SSFP at 9.4 tesla', *Magn Reson Med*, 76: 163-71.
- Scheffler, K., and J. Hennig. 2003. 'Is TrueFISP a gradient-echo or a spin-echo sequence?', *Magn Reson Med*, 49: 395-7.
- Scheffler, K., E. Seifritz, D. Bilecen, R. Venkatesan, J. Hennig, M. Deimling, and E. M. Haacke. 2001. 'Detection of BOLD changes by means of a frequency-sensitive trueFISP technique: preliminary results', *NMR Biomed*, 14: 490-6.
- Schluppeck, D., P. Glimcher, and D. J. Heeger. 2005. 'Topographic organization for delayed saccades in human posterior parietal cortex', *J Neurophysiol*, 94: 1372-84.
- Schoppik, D., K. I. Nagel, and S. G. Lisberger. 2008. 'Cortical mechanisms of smooth eye movements revealed by dynamic covariations of neural and behavioral responses', *Neuron*, 58: 248-60.
- Segonne, F., A. M. Dale, E. Busa, M. Glessner, D. Salat, H. K. Hahn, and B. Fischl. 2004. 'A hybrid approach to the skull stripping problem in MRI', *Neuroimage*, 22: 1060-75.

- Self, M. W., R. N. Kooijmans, H. Super, V. A. Lamme, and P. R. Roelfsema. 2012. 'Different glutamate receptors convey feedforward and recurrent processing in macaque V1', *Proc Natl Acad Sci U S A*, 109: 11031-6.
- Self, M. W., T. van Kerkoerle, H. Super, and P. R. Roelfsema. 2013. 'Distinct roles of the cortical layers of area V1 in figure-ground segregation', *Curr Biol*, 23: 2121-9.
- Setsompop, K., D. A. Feinberg, and J. R. Polimeni. 2016. 'Rapid brain MRI acquisition techniques at ultra-high fields', *NMR Biomed*, 29: 1198-221.
- Shajan, G., M. Kozlov, J. Hoffmann, R. Turner, K. Scheffler, and R. Pohmann. 2014. 'A 16-channel dual-row transmit array in combination with a 31-element receive array for human brain imaging at 9.4 T', *Magn Reson Med*, 71: 870-9.
- Shmuel, A., M. Augath, A. Oeltermann, and N. K. Logothetis. 2006. 'Negative functional MRI response correlates with decreases in neuronal activity in monkey visual area V1', *Nat Neurosci*, 9: 569-77.
- Shmuel, A., D. Chaimow, G. Raddatz, K. Ugurbil, and E. Yacoub. 2010. 'Mechanisms underlying decoding at 7 T: ocular dominance columns, broad structures, and macroscopic blood vessels in V1 convey information on the stimulated eye', *Neuroimage*, 49: 1957-64.
- Sillito, A. M., J. Cudeiro, and H. E. Jones. 2006. 'Always returning: feedback and sensory processing in visual cortex and thalamus', *Trends Neurosci*, 29: 307-16.
- Silver, M. A., D. Ress, and D. J. Heeger. 2005. 'Topographic maps of visual spatial attention in human parietal cortex', *J Neurophysiol*, 94: 1358-71.
- Smith, M. A., and M. A. Sommer. 2013. 'Spatial and temporal scales of neuronal correlation in visual area V4', *J Neurosci*, 33: 5422-32.
- Stanton, G. B., H. R. Friedman, E. C. Dias, and C. J. Bruce. 2005a. 'Cortical afferents to the smooth-pursuit region of the macaque monkey's frontal eye field', *Exp Brain Res*, 165: 179-92.
- Stanton, Gregory B, Harriet R Friedman, Elisa C Dias, and Charles J Bruce. 2005b. 'Cortical afferents to the smooth-pursuit region of the macaque monkey's frontal eye field', *Experimental brain research*, 165: 179-92.
- Stehling, M. K., R. J. Ordidge, R. Coxon, and P. Mansfield. 1990. 'Inversion-recovery echo-planar imaging (ir-epi) at 0.5 T', *Magnetic Resonance in Medicine*, 13: 514-17.
- Thier, P., and U. J. Ilg. 2005. 'The neural basis of smooth-pursuit eye movements', *Curr Opin Neurobiol*, 15: 645-52.
- Thomson, A. M., and A. P. Bannister. 2003. 'Interlaminar connections in the neocortex', *Cereb Cortex*, 13: 5-14.
- Tootell, R. B., J. D. Mendola, N. K. Hadjikhani, P. J. Ledden, A. K. Liu, J. B. Reppas, M. I. Sereno, and A. M. Dale. 1997. 'Functional analysis of V3A and related areas in human visual cortex', *J Neurosci*, 17: 7060-78.
- Tootell, R. B., and J. B. Taylor. 1995. 'Anatomical evidence for MT and additional cortical visual areas in humans', *Cereb Cortex*, 5: 39-55.
- Trampel, R., P.-L. Bazin, Schaefer A., Heidemann R., Ivanov D., Lohmann G., Geyer S., and R. Turner. 2012. "Laminar-specific BOLD Fingerprints of Sensorimotor Areas during Imagined and Actual Finger Tapping." In *OHBM*, 628. Beijing.
- Trampel, R., P. L. Bazin, K. Pine, and N. Weiskopf. 2017. 'In-vivo magnetic resonance imaging (MRI) of laminae in the human cortex', *Neuroimage*.
- Triantafyllou, C., R. D. Hoge, G. Krueger, C. J. Wiggins, A. Potthast, G. C. Wiggins, and L. L. Wald. 2005. 'Comparison of physiological noise at 1.5 T, 3 T and 7 T and optimization of fMRI acquisition parameters', *Neuroimage*, 26: 243-50.

- Troncoso, X. G., M. B. McCamy, A. N. Jazi, J. Cui, J. Otero-Millan, S. L. Macknik, F. M. Costela, and S. Martinez-Conde. 2015. 'V1 neurons respond differently to object motion versus motion from eye movements', *Nat Commun*, 6: 8114.
- Turner, R., and T. Jones. 2003. 'Techniques for imaging neuroscience', *Br Med Bull*, 65: 3-20.
- Uğurbil, K., G. Adriany, P. Andersen, W. Chen, R. Gruetter, X. Hu, H. Merkle, D. S. Kim, S. G. Kim, J. Strupp, X. H. Zhu, and S. Ogawa. 2000. 'Magnetic resonance studies of brain function and neurochemistry', *Annu Rev Biomed Eng*, 2: 633-60.
- Uğurbil, Kâmil, Gregor Adriany, Peter Andersen, Wei Chen, Michael Garwood, Rolf Gruetter, Pierre-Gil Henry, Seong-Gi Kim, Haiying Lieu, Ivan Tkac, Tommy Vaughan, Pierre-Francoise Van De Moortele, Essa Yacoub, and Xiao-Hong Zhu. 2003. 'Ultrahigh field magnetic resonance imaging and spectroscopy', *Magnetic Resonance Imaging*, 21: 1263-81.
- Uludag, K., and P. Blinder. 2018. 'Linking brain vascular physiology to hemodynamic response in ultra-high field MRI', *Neuroimage*, 168: 279-95.
- Van de Moortele, P. F., E. J. Auerbach, C. Olman, E. Yacoub, K. Ugurbil, and S. Moeller. 2009. 'T1 weighted brain images at 7 Tesla unbiased for Proton Density, T2* contrast and RF coil receive B1 sensitivity with simultaneous vessel visualization', *Neuroimage*, 46: 432-46.
- van der Kouwe, A. J. W., T. Benner, D. H. Salat, and B. Fischl. 2008. 'Brain morphometry with multiecho MPRAGE', *Neuroimage*, 40: 559-69.
- Van Der Zwaag, W, P Buur, M Versluis, and JP Marques. 2016. "Distortion-matched T1-maps and bias-corrected T1w-images as anatomical reference for submillimeter-resolution fMRI." In *Proceedings of the International Society of Magnetic Resonance in Medicine*.
- Van Essen, D. C., and J. H. Maunsell. 1980. 'Two-dimensional maps of the cerebral cortex', *J Comp Neurol*, 191: 255-81.
- van Kerkoerle, T., M. W. Self, B. Dagnino, M. A. Gariel-Mathis, J. Poort, C. van der Togt, and P. R. Roelfsema. 2014. 'Alpha and gamma oscillations characterize feedback and feedforward processing in monkey visual cortex', *Proc Natl Acad Sci U S A*, 111: 14332-41.
- van Mourik, T., Jpjm van der Eerden, P. L. Bazin, and D. G. Norris. 2019. 'Laminar signal extraction over extended cortical areas by means of a spatial GLM', *PLoS One*, 14: e0212493.
- Vaughan, J. T., M. Garwood, C. M. Collins, W. Liu, L. DelaBarre, G. Adriany, P. Andersen, H. Merkle, R. Goebel, M. B. Smith, and K. Ugurbil. 2001. '7T vs. 4T: RF power, homogeneity, and signal-to-noise comparison in head images', *Magn Reson Med*, 46: 24-30.
- von Holst, E., and H. Mittelstaedt. 1950a. 'Das Reafferenzprinzip', *Naturwissenschaften*, 37: 464-76.
- von Holst, Erich, and Horst Mittelstaedt. 1950b. 'Das Reafferenzprinzip', *Naturwissenschaften*, 37: 464-76.
- Waehnert, M. D., J. Dinse, A. Schafer, S. Geyer, P. L. Bazin, R. Turner, and C. L. Tardif. 2016. 'A subject-specific framework for in vivo myeloarchitectonic analysis using high resolution quantitative MRI', *Neuroimage*, 125: 94-107.
- Waehnert, M. D., J. Dinse, M. Weiss, M. N. Streicher, P. Waehnert, S. Geyer, R. Turner, and P. L. Bazin. 2014. 'Anatomically motivated modeling of cortical laminae', *Neuroimage*, 93 Pt 2: 210-20.

- Waehnert, Miriam, Marcel Weiss, Markus Streicher, Pierre-Louis Bazin, S. Geyer, and Robert Turner. 2012. *Do cortical layers conform to the Laplace equation?*
- Wald, L. L., and J. R. Polimeni. 2017. 'Impacting the effect of fMRI noise through hardware and acquisition choices - Implications for controlling false positive rates', *Neuroimage*, 154: 15-22.
- Wall, M. B., A. Lingnau, H. Ashida, and A. T. Smith. 2008. 'Selective visual responses to expansion and rotation in the human MT complex revealed by functional magnetic resonance imaging adaptation', *Eur J Neurosci*, 27: 2747-57.
- Wang, L., R. E. Mruzek, M. J. Arcaro, and S. Kastner. 2015. 'Probabilistic Maps of Visual Topography in Human Cortex', *Cereb Cortex*, 25: 3911-31.
- Williams, M. A., C. I. Baker, H. P. Op de Beeck, W. M. Shim, S. Dang, C. Triantafyllou, and N. Kanwisher. 2008. 'Feedback of visual object information to foveal retinotopic cortex', *Nat Neurosci*, 11: 1439-45.
- Wong-Riley, M. 1978. 'Reciprocal connections between striate and prestriate cortex in squirrel monkey as demonstrated by combined peroxidase histochemistry and autoradiography', *Brain Res*, 147: 159-64.
- Xiang, Q. S., and F. Q. Ye. 2007. 'Correction for geometric distortion and N/2 ghosting in EPI by phase labeling for additional coordinate encoding (PLACE)', *Magn Reson Med*, 57: 731-41.
- Yacoub, E., T. Q. Duong, P. F. Van De Moortele, M. Lindquist, G. Adriany, S. G. Kim, K. Ugurbil, and X. Hu. 2003. 'Spin-echo fMRI in humans using high spatial resolutions and high magnetic fields', *Magn Reson Med*, 49: 655-64.
- Yacoub, E., N. Harel, and K. Ugurbil. 2008a. 'High-field fMRI unveils orientation columns in humans', *Proceedings of the National Academy of Sciences of the United States of America*, 105: 10607-12.
- Yacoub, E., N. Harel, and K. Ugurbil. 2008b. 'High-field fMRI unveils orientation columns in humans', *Proc Natl Acad Sci U S A*, 105: 10607-12.
- Yarnykh, V. L. 2010. 'Optimal radiofrequency and gradient spoiling for improved accuracy of T1 and B1 measurements using fast steady-state techniques', *Magn Reson Med*, 63: 1610-26.
- Yarnykh, Vasily L. 2007. 'Actual flip-angle imaging in the pulsed steady state: A method for rapid three-dimensional mapping of the transmitted radiofrequency field', *Magnetic Resonance in Medicine*, 57: 192-200.
- Zaitsev, M., J. Hennig, and O. Speck. 2004. 'Point spread function mapping with parallel imaging techniques and high acceleration factors: fast, robust, and flexible method for echo-planar imaging distortion correction', *Magn Reson Med*, 52: 1156-66.
- Zaretskaya, N., B. Fischl, M. Reuter, V. Renvall, and J. R. Polimeni. 2018. 'Advantages of cortical surface reconstruction using submillimeter 7 T MEMPRAGE', *Neuroimage*, 165: 11-26.
- Zeki, S., J. D. Watson, C. J. Lueck, K. J. Friston, C. Kennard, and R. S. Frackowiak. 1991. 'A direct demonstration of functional specialization in human visual cortex', *J Neurosci*, 11: 641-9.
- Zeng, H., and R. T. Constable. 2002. 'Image distortion correction in EPI: comparison of field mapping with point spread function mapping', *Magn Reson Med*, 48: 137-46.
- Zhang, T., H. W. Heuer, and K. H. Britten. 2004. 'Parietal area VIP neuronal responses to heading stimuli are encoded in head-centered coordinates', *Neuron*, 42: 993-1001.
- Zimmermann, J., R. Goebel, F. De Martino, P. F. van de Moortele, D. Feinberg, G. Adriany, D. Chaimow, A. Shmuel, K. Ugurbil, and E. Yacoub. 2011. 'Mapping the organization of

axis of motion selective features in human area MT using high-field fMRI', *PLoS One*, 6: e28716.

Statement of Contributions

CHAPTER 2. Acquisition and Analysis Strategies for Conducting Laminar fMRI Studies at UHF

Fatemeh Molaei-Vaneghi; Designed and conducted the experiments, collected and analyzed the data, wrote and revised the manuscript.

Natalia Zaretskaya; Contributed to data acquisition.

Tim van Mourik; Contributed to data analysis and revision of the manuscript.

Jonas Bause; Contributed to data acquisition.

Andreas Bartels; Contributed to data analysis and revision of the manuscript.

Klaus Scheffler; Contributed to designing the experiments and data acquisition.

CHAPTER 3. Laminar Responses to Visual Motion and Pursuit Integration in Human Areas V3A and V6 Measured Using 9.4T fMRI

(in internal review for submission to Neuroimage)

Fatemeh Molaei-Vaneghi; Designed and conducted the experiments, collected and analyzed the data, wrote and revised the manuscript.

Natalia Zaretskaya; Contributed to revision of the manuscript.

Tim van Mourik; Contributed to data analysis and revision of the manuscript.

Jonas Bause; Contributed to data acquisition and revision of the manuscript.

Andreas Bartels; Designed the study, contributed to data analysis, and revised the manuscript.

Klaus Scheffler; contributed to designing the study, data acquisition, and manuscript revision.

CHAPTER 4. Real World Motion Processing in MT, pMST, and V1. A Laminar fMRI Study at 9.4T

(in internal review for submission to Neuroimage)

Fatemeh Molaei-Vaneghi; Designed and conducted the experiments, collected and analyzed the data, wrote and revised the manuscript.

Natalia Zaretskaya; Contributed to data analysis and revision of the manuscript.

Andreas Bartels; Designed the study, contributed to data analysis, and revised the manuscript.

Klaus Scheffler; contributed to designing the study, data acquisition, and manuscript revision.

Acknowledgements

First and foremost, I would like to thank my supervisor Prof. Andreas Bartels for his daring curiosity to navigate unexplored territories of science, for his drive to ask difficult questions, and for his commitment to stand by me during my PhD journey. I would also like to thank Prof. Klaus Scheffler for his generous support, for believing in my research and trusting my intuition, and above all for providing me with means to navigate the challenging alleys of my research. Finally, I would like to thank other members of my thesis committee, Prof. Ilg and Prof. Braun for their encouragement, insightful guidance, and support.

A special thanks goes to my partner Maysam and my mother Farzaneh for showing me how to push through my limits and to become more of myself by giving more to others.